2009

Thermodynamic prediction of glass formation tendency, cluster-in-jellium model for metallic glasses, ab initio tight-binding calculations, and new density functional theory development for systems with strong electron correlation

Yongxin Yao
Iowa State University

Thermodynamic prediction of glass formation tendency, cluster-in-jellium model for metallic glasses, *ab initio* tight-binding calculations, and new density functional theory development for systems with strong electron correlation

by

Yongxin Yao

A dissertation submitted to the graduate faculty

in partial fulfillment of the requirements for the degree of

DOCTOR OF PHILOSOPHY

Major: Condensed Matter Physics

Program of Study Committee:
Kai-Ming Ho, Major Professor
Ralph E. Napolitano
David C. Johnston
Jianwei Qiu
Matthew Kramer
Jörg Schmalian

Iowa State University

Ames, Iowa

2009

DEDICATION

I would like to dedicate this thesis to my wife Qing and to my daughter Sarah, without whose support I would not have been able to complete this work. Thanks to my God who make known to me the path of life, where I may enjoy and practice a life of faith.

TABLE OF CONTENTS

LIST OF TABLES

LIST OF FIGURES

CHAPTER 1. OVERVIEW

Solidification of liquid is a very rich and complicated field, although there is always a famous homogeneous nucleation theory in a standard physics or materials science text book. Depending on the material and processing condition, liquid may solidify to single crystalline, polycrystalline with different texture, quasi-crystalline, amorphous solid or glass (Glass is a kind of amorphous solid in general, which has short-range and medium-range order). Traditional oxide glass may easily be formed since the covalent directional bonded network is apt to be disturbed. In other words, the energy landcape of the oxide glass is so complicated that system need extremely long time to explore the whole configuration space. On the other hand, metallic liquid usually crystalize upon cooling because of the metallic bonding nature. However, Klement et.al., (1960) reported that Au-Si liquid underwent an amorphous or "glassy" phase transformation with rapid quenching. In recent two decades, bulk metallic glasses have also been found in several multicomponent alloys[Inoue et al., (2002)]. Both thermodynamic factors (e.g., free energy of various competitive phase, interfacial free energy, free energy of local clusters, etc.) and kinetic factors (e.g., long range mass transport, local atomic position rearrangement, etc.) play important roles in the metallic glass formation process.

Metallic glass is fundamentally different from nanocrystalline alloys. Metallic glasses have to undergo a nucleation process upon heating in order to crystallize. Thus the short-range and medium-range order of metallic glasses have to be completely different from crystal. Hence a method to calculate the energetics of different local clusters in the undercooled liquid or glasses become important to set up a statistic model to describe metalllic glass formation.

Scattering techniques like x-ray and neutron have widely been used to study the structues of metallic glasses. Meanwhile, computer simulation also plays an important role, as it may

directly track the movement of every atom. Simulation time is a major limit for molecular dynamics, not only because of "slow" computer speed, but also because of the accumulation error in the numerical treatment of the motion equations. There is also a great concern about the reliability of the emperical potentials if using classical molecular dynamics. *Ab initio* methods based on density functional theory(DFT) do not have this problem, however, it suffers from small simulation cells and is more demanding computationally. When crystal phase is involved, size effect of the simulation cell is more pronounced since long-range elastic energy would be established. Simulation methods which are more efficient in computation but yet have similar reliability as the *ab initio* methods, like tight-binding method, are highly desirable.

While the complexity of metallic glasses comes from the atomistic level, there is also a large field which deals with the complexity from electronic level. The only "*ab initio*" method applicable to solid state systems is density functional theory with local density approximation(LDA) or generalized gradient approximation(GGA) for the exchange-correlation energy. It is very successful for simple sp element, where it reaches an high accuracy for determining the surface reconstruction. However, there is a large class of materials with strong electron correlation, where DFT based on LDA or GGA fails in a fundamental way. An "*ab initio*" method which can generally apply to correlated materials, as LDA for simple sp element, is still to be developed.

The thesis is prepared to address some of the above problems, which is arranged as follows:

Chapter 2: We have calculated the T_0 curves for several Al-Rare Earth (RE) binary alloys and compared the results with reported observations of glass formation (T_0 curve is defined as a trjectory in temperature-composition space where the liquid phase and solid phase have same Gibbs free energies), in order to assess the importance of the transport-based resistance to crystallization in the overall glass formation process. Our results show that the experimentally observed glass forming compositions for Al-(Ce,Gd,Ho,Nd,Y,Dy) alloys strongly correlate with the composition range bounded by the T_0 curves associated with the relevant crystalline phases. This agreement indicates that sluggish material transport is a key factor governing

glass formation in these systems, a behavior that differs substantially from the more common oxide glasses, where directional bonding constraints may stabilize the glassy network based on topological considerations.

Chapter 3: A jellium-passivated cluster model is developed to study the energetics of short-range ordering in supercooled liquid and glass systems. Calculations for single atoms embedded in jellium yield results in good agreement with bulk values for the cohesive energy, atomic volume as well as angular-momentum-projected electronic density of states. The energy difference between icosahedral clusters and FCC embryos in jellium is found to correlate with the glass-forming ability of liquid Al alloys. The model will be useful for studying the short-range order tendency with minor chemical additions in metallic glass formation, without the use of large unit cell calculations.

Chapter 4: We demonstrate an efficient and accurate first-principles method to calculate the electronic structure of a large system using a divide-and-conquer strategy based on localized quasi-atomic minimal basis set orbitals recently developed. Tight-binding Hamiltonian and overlap matrices of a big system can be constructed by extracting the matrix elements for a given pair of atoms from first-principles calculations of smaller systems that represent the local bonding environment of the particular atom pair. The approach is successfully applied to the studies of electronic structure in graphene nano-ribbons. This provides a promising way to do the electronic simulation for big systems directly from first-principles.

Chapter 5: We have developed a new density functional theory incorporating the correlated electronic effects into the kinetic energy via Gutzwiller approximation. All the Coulomb integrals are determined self-consistently without any adjustable parameters. In addition to the set of one-electron Schrödinger equations analogous to the standard LDA approach, we get another set of linear equations with respect to the probabilities of local configurations as the solution of the many body problem. A preliminary Fortran90 code has been developed with an interface to VASP. We applied our method to several systems with important electron correlation effects and got encouraging results.

CHAPTER 2. THERMODYNAMIC LIMITS OF CRYSTALLIZATION AND THE PREDICTION OF GLASS FORMATION TENDENCY

2.1 Introduction

Metallic alloys which resist crystallization in their undercooled states sufficiently well to become amorphous solids or "metallic glasses" have emerged as a very interesting and potentially useful class of materials. However, the criteria for glass-formation in metallic systems are still poorly understood. Unlike traditional topological or network glass systems where structural frustration promotes the formation of the glass state and thus may be formed even for pure element systems, metallic glasses are only found in multicomponent alloy systems. This indicates that restriction of material transport is a dominant factor in the glass formation process.

To date, a great deal of effort has been concentrated on (i) the quantification of the diverse and unusual physical and mechanical properties afforded by glass forming metallic alloys, (ii) the identification of compositional ranges that give rise to amorphous solids in various alloy systems, and (iii) the development of alloys and processing techniques capable of yielding glassy alloys in quantities or geometries that permit engineering application, i.e. "bulk" metallic glasses. A number of excellent reviews[Inoue et al., (2002); Inoue (1998); Greer (1995)] are available, and we forego a comprehensive discussion of these topics here.

More fundamentally, considerably less effort has been devoted to understanding the thermodynamic and kinetic implications of the glassy state exhibited by many metallic systems. Differing substantially from the more common oxide glasses, where directional bonding constraints may lead to static glassy network structures, glass formation in metallic systems cannot be reasonably justified in terms of simple topological considerations. Clearly, the transition to

the glassy state in a metallic system must be described as kinetic in nature, where relaxation to an energetically favorable crystalline state becomes sufficiently sluggish to effectively prevent its existence. Thus, the fundamental question to be answered with regard to this transition is: "What are the critical kinetic contributors which limit the crystallization process in a metallic system, and how are these influenced by temperature and chemical composition?" Indeed, a substantial amount of work has been reported pursuant to the second part of this question, and composition ranges where glass formation is practically achievable have been experimentally determined for a number of metallic systems. However, the more fundamental, first, part of the question has not been sufficiently addressed, and the suppression of structural and chemical relaxation processes contributing to the kinetic transition have not been distinguished or well described.

Following the earliest observations of amorphous or "glassy" phase formation, reported in 1960 for a rapidly quenched Au-Si alloy[Klement et.al., (1960)] and in 1965 for a Pd-Si alloy[Duwez et al., (1965)], researchers looked to quantify the inherent glass formation tendency, commonly termed glass forming ability (GFA), for metallic systems. Various relationships were proposed, suggesting that parameters such as the melting temperature, the cohesive energy, the Debye temperature, the reduced liquidus temperature, and linear combinations of pure component melting temperatures may correlate with the glass transition temperature, T_g [Marcus et al., (1976); Donald et al., (1978); Turnbull et al., (1961); Kauzmann (1948); Turnbull (1969); Davies et al., (1975)]. (T_g may be defined as the temperature at which the heat capacity changes abruptly.) Such correlations offered only limited utility, but reasonable success was achieved for several systems through the use of GFA maps constructed with two thermodynamic parameters. For example, Giessen et al., (1980) compared the GFA for several binary alloys by plotting the heat of formation for the liquid phase versus the atomic radius ratio of the two alloy components. Also, plots of reduced liquidus temperature ($T_{LR} = \left(\bar{T}_L^0 - T_L\right)/\bar{T}_L^0$, where T_L is the liquidus temperature and $\bar{T}_L^0$ is a linear combination of the pure component melting temperatures) versus reduced eutectic composition ($\left(C_e - C_s\right)/C_e$, where C_e is the eutectic composition and C_s is the solidus composition for the solvent-rich phase at the eutec-

tic temperature) were employed by Whang (1983) to compare the GFA for Ti, Zr, Si, and Al alloys.

Work by Lu et al., (2000) suggests that the reduced glass transition temperature ($T_{rg} = T_g/T_L$) may be a reasonable indicator of the GFA in Zr, La, Mg, Pd, and rare earth alloys (all containing at least three components), while other experimental reports suggest that the freezing range, ΔT_{xg}, is a more reliable indicator in several multicomponent Fe-base, Mg-base, and Pd-Ni-base alloys[Inoue et al., (1993); Shen et al., (1998, 1999); Murty et al., (2000); Inoue et al., (2001)]. Lu et al., (2002) examined this issue and proposed a parameter, defined as $\gamma = T_x/(T_g+T_L)$, that describes the ease of devitrification for a metallic glass and correlates with GFA better than both T_{rg} and ΔT_{xg}. They go on to relate this parameter to a critical cooling rate, R_c, and an associated critical section thickness[Lu et al., (2002, 2003)].

Beyond these rudimentary correlations, several approaches have been used for describing the behavior of undercooled metallic liquids and predicting glass formation in metallic alloys[Egami (2002)]. Beginning with Cohen et al., (1959), free volume theories have been used with reasonable success to describe some aspects of molecular motion and the associated glass transition[Turnbull et al., (1961); Cohen et al., (1959); Turnbull (1970); Taub et al., (1980)]. Continuum mode-coupling theories[Jacle (1986); Gotze et al., (1992)] have been useful in describing high temperature behavior of liquids, but these break down at lower temperatures where atomistic mechanisms become important for transport processes[Egami (2002)]. Egami used local topological considerations to explain how the glass transition may occur at the nanoscale, giving rise to glassy clusters[Egami (2002)]. By modifying a treatment for oxide glasses, Takeuchi et al., (2001) calculated critical cooling rates, R_c, for glass formation in Ni, Co, and Pd-Cu based alloys, showing a dramatic reduction in R_c with increasingly negative enthalpy of mixing in the liquid and with increasing atomic radius mismatch. Fecht et al., (2004) have summarized the requirements for the formation of bulk metallic glasses (i.e. $R_c \geq 1$ K/s) with the following five conditions: (i) steep liquidus boundaries meeting at a low temperature eutectic, (ii) atomic radius mismatch $> 15\%$, (iii) reduced driving force for crystallization, (iv) $T_{rg} > 0.65$, and (v) complete miscibility in the liquid at the relevant

temperatures. While structural "confusion" must play a role in suppressing the kinetics of crystallization[Greer (1995)], these general conditions suggest that observed glass formation tendency is fundamentally linked to the thermodynamic properties of the system.

In this chapter, we examine the hypothesis that the dominant mechanism for "confusion" in metallic glass formation comes from the limitation of material transport at the compositional scale and that the reduced diffusional burden associated with partitionless crystallization provides a temporally competitive avenue for relaxation and, thus, a fundamental thermodynamic and kinetic limit to the glass formation range. We employ a solution thermodynamics approach to compute the chemical limits of partitionless crystallization for several Al-RE binary alloys, chosen because their glass formation compositions have been well characterized by experiment and the reported glass formation ranges deviate substantially from the eutectic compositon. More specifically, we calculate the T_0 temperature as a function of composition and assert that glass formation is unlikely for compositions where $T_g < T_0$, suggested by Boettinger (1982), since the partitioning and chemical transport requirements for crystallization vanish below this temperature. In this case, the intersection between the T_g and T_0 curves for the two (or more) crystalline phases involved in a eutectic reaction would indicate a reasonable composition range for glass formation.

2.2 Calculation Method

T_0 is defined as the temperature for which the liquid phase and the crystalline phase have equal Gibbs free energies. Fig. 2.1 schematically shows the Gibbs free energy(G) versus composition(x) curves of one liquid phase and two solid solution phases at 500K for A-B binary system. From the intersections of the curves we may read that $T_0(x = 0.4) = 500K$ for solid-I and liquid, and $T_0(x = 0.7) = 500K$ for solid-II and liquid. One may get the T_0 versus x curve by scanning the whole temperature and composition domains. Fig. 2.2 shows the typical T_0 curves for A-B binary system with a single eutectic point.

In practice, the T_0 calculations are performed using the CALPHAD (CALculation of PHAse Diagrams) methodology, with missing parameters generated by *ab initio* calculations. Thus,

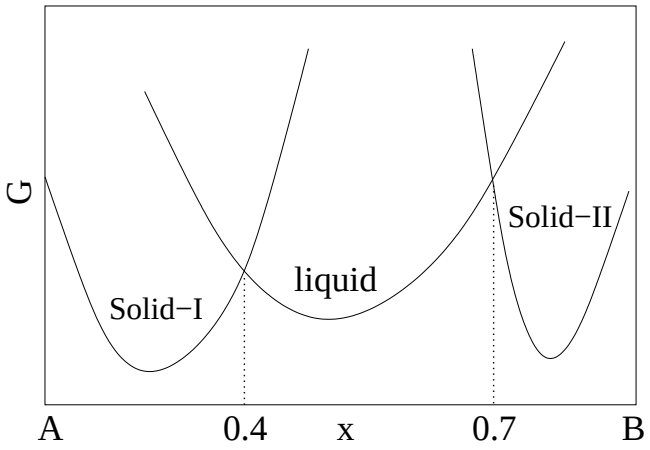

Figure 2.1 Schematic illustration of Gibbs free energy curves of solid and liquid phases for A-B binary system at a fixed temperature T. The intersection of the curves gives the T_0 temperature(=T) at compositions of x=0.4 and x=0.7.

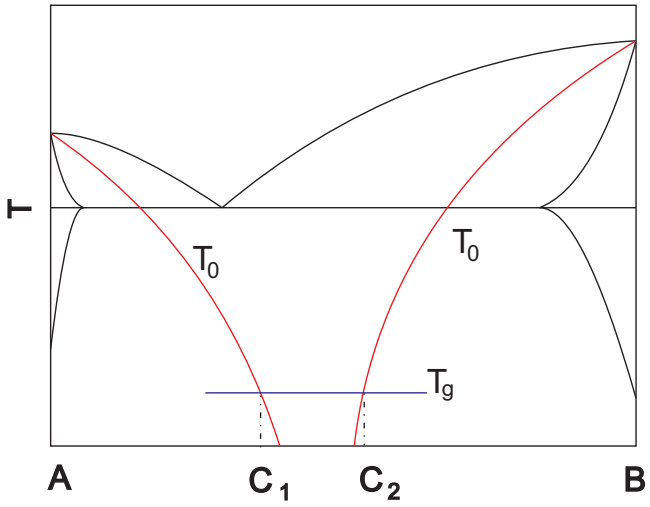

Figure 2.2 Schematic illustration of the simple eutectic phase diagram of A-B binary alloys with T_0 curves. The partition zone $(C_1 - C_2)$ bounded by the T_0 curves around T_g may serve as a reasonable lower limit for glass formation.

each phase is treated as a solution whose Gibbs free energy is expressed analytically over a certain composition and temperature range. In our treatment, binary solution phases are modeled with a single-sublattice, with a molar Gibbs free energy given as

$$G^{\Phi} = (1-x)\, G_{Al}^{\Phi,0} + xG_{RE}^{\Phi,0} + RT\left((1-x)\ln(1-x) - x\ln x\right) + G^{\Phi,xs} \tag{2.1}$$

Where $G_A^{\Phi,0}$ is the molar Gibbs free energy of the pure element A in structure Φ, taken from Dinsdale (1991). The excess Gibbs free energy $G^{\Phi,xs}$ is expressed as

$$G^{\Phi,xs} = (1-x)\, x \sum_{j=0}^{n} L_{Al,RE}^{\Phi,j} (1-2x)^j \tag{2.2}$$

Where the interaction parameters $L_{Al,RE}^{\Phi,j}$ take the form $A^{\Phi,j} + B^{\Phi,j}T$, including both enthalpic $\left(A^{\Phi,j}\right)$ and entropic $\left(-B^{\Phi,j}\right)$ contributions to each mixing term.

Typically, binary intermetallic phases are described using a two-sublattice model(which is independent of real crystal structure), with each component occupying one sublattice without mixing. The Gibbs free energy has the form

$$G^{Al_aRE_b} = aG_{Al}^{\Phi,0} + bG_{RE}^{\Phi,0} + A^{Al,RE} + B^{Al,RE}T \tag{2.3}$$

Where $A^{Al,RE}$ and $-B^{Al,RE}$ represent the enthalpy and entropy of formation for the stoichiometric compound. (For the Al-RE alloys studied in this paper, the coefficients A and B are taken from reference[Cacciamani et al., (2001, 2003); Gröbner et al., (1995)]. Some of the model coefficients have been tested in ternary systems[Cacciamani et al., (2003); Gröbner et al., (1995)].)

We here treat the intermetallic phases as solutions, rather than simple stoichiometric compounds assumed in usual CALPHAD calculations. We approximate the Gibbs free energy of the intermetallic solution as

$$G^{Al_{1-x}RE_x} = (1-x)\, G_{Al}^{\Phi,0} + xG_{RE}^{\Phi,0} + \Delta H^{Al_{1-x}RE_x} \tag{2.4}$$

Where the formation enthalpy is estimated by interpolating *ab initio* total energy calculation results for alloys at selected nearby compositions. As an example, the resulted Gibbs free energy curve for Al_3Y phase at 300 K was shown in Fig.2.3. We ignore the formation entropy,

assuming that its contribution is relatively small in the temperature range where the metallic glasses usually form. In fact, for all the intermetallic compounds under investigation, the contribution of the formation entropy is one order smaller than that of formation enthalpy near 500 K, based on fitted and experimental data, as shown in Table 2.1. Furthermore, the formation entropy is negative in all the intermetallic compounds investigated, which would only raise the corresponding intermetallic Gibbs free energy at the particular composition, forcing the T_0 curve to be steeper. This would not affect our conclusions.

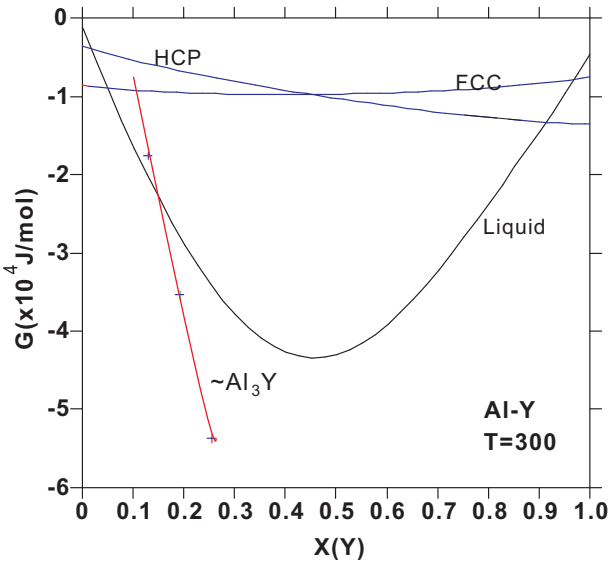

Figure 2.3 Gibbs free energy(G) versus composition(X) of Y curve for Al_3Y phase at 300 K. The Gibbs energy curves for liquid, fcc and hcp are also shown for reference. The intersection between Gibbs energy curve of Al_3Y and that of liquid give the specific composition with $T_0 = 300K$.

The first-principles calculations were done using VASP[Kresse et al., (1996)] with a plane-wave basis set. Projector augmented wave (PAW) method[Kresse et al., (1999)] were employed and the exchange-correlation potential was based on the generalized gradient corrections parametrized by Perdew et al., (1996).

Table 2.1 Comparison between the contributions from formation enthalpy ΔH_f and formation entropy $-T\Delta S_f$ based on the fitted and experimental data[Cacciamani et al., (2003); Gröbner et al., (1995)]. T=500K is used in the table. The contribution from formation entropy to the total Gibbs free energy is one order of magnitude smaller that that from formation enthalpy.

Intermetallic compound	ΔH_f (kJ/mol)	ΔS_f (J/K/mol)	$-T\Delta S_f$ (kJ/mol)	$-T\Delta S_f/H_f$
$\alpha Al_{11}Ce_3$	-41.5	-9.68	4.84	12%
Al_3Ce	-45.0	-10.3	5.16	11%
$\alpha Al_{11}Nd_3$	-39.1	-9.35	4.68	12%
Al_3Nd	-45.0	-11.7	5.84	13%
Al_3Gd	-41.2	-7.40	3.70	13%
Al_3Ho	-43.0	-7.53	3.77	9 %
Al_3Dy	-37.5	-6.46	3.23	9 %
Al_3Y	-47.5	-10.6	5.31	11%

2.3 Results and discussions

The calculated T_0 curve results, plotted with the truncated Al-rich part phase diagrams for Al-Ce, Al-Gd, Al-Ho, Al-Nd, Al-Y, and Al-Dy, are shown in Fig.2.4. The compositional dependence of structure for the corresponding rapidly solidified Al-RE binary alloys are also shown as insets. Two right-side T_0 curves are shown for Al-Ce and Al-Nd since there exist two competing phases with similar compositions. The shaded regions are the experimentally observed glass-forming composition ranges[Inoue (1998)]. Though the glass transition temperature, T_g, is not given, it is reasonable to assume that it is above 300K. Down to 300K, the partitioning zone defined as the composition range bounded by the relevant T_0 curves matches very well with the experimentally observed glass-forming range. For comparison, GFA predicted by T_{rg} and T_{LR} is peaked around the eutectic composition, while Takeuchi's R_c criterion [Takeuchi et al., (2001)] favors the composition near 40 at.% of RE. Thus only our T_0 criterion gives a reasonable prediction in the systems investigated here. It should be pointed out that the above-mentioned T_{rg}, ΔT_{xg} and γ criteria are generally not good for GFA *prediction* since T_g and T_x are unknown for new systems, although GFA could still be predicted by assuming that the compositional dependence is dominated by T_L.

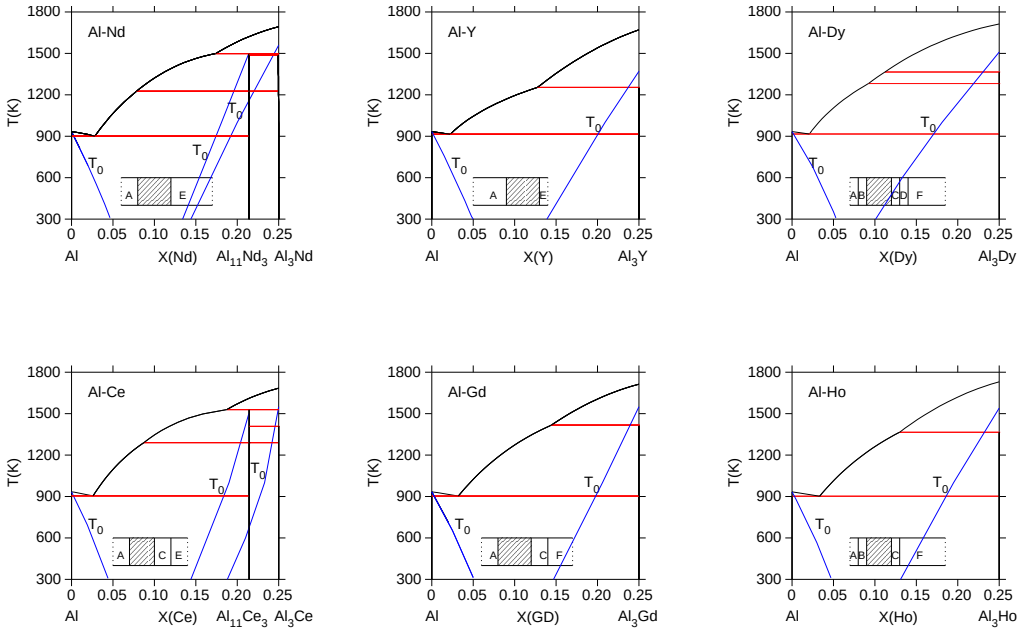

Figure 2.4 Calculated T_0 curves with the truncated Al-rich part phase diagrams for Al-Ce, Al-Gd, Al-Ho, Al-Nd, Al-Y, and Al-Dy. Inset: compositional dependence of structure in the corresponding rapidly solidified Al-RE binary alloys taken from Ref.[Dinsdale (1991)]. Shaded regions: amorphous, A: Al solid solution, B: Amorphous + Al, C: Amorphous +X (unidentified phase), D: Al +X (unidentified phase), E: $Al + Al_{11}RE_3$, F: $Al + Al_3RE$.

Considering that partitionless crystallization requires only short range atomic motion and that such a transition may occur at extremely high rates [Aziz et al., (2004)], we view the T_0 criterion as an upper bound (i.e. a zero driving force) temperature limit for partitionless crystalline solidification, and, therefore, view the two relevant T_0 curves in an eutectic system as operational inner bounds for the glass formation range. Accordingly, we offer the present analysis as a means for assessing the importance of chemical partitioning in the resistance to crystal phase formation. Instead of the traditional eutectic composition, around which it is often presumed that the glass-forming ability is particularly high, our results suggest that the partitioning range, bounded by the T_0 curves, may offer a more relevant thermodynamic criterion for metallic glass formation tendency. It is interesting to note that the partitioning ranges for the systems we investigated here are all clearly off the eutectic compositions. Our theoretical predictions agree well with experiment that glass forming ranges have been severely shifted to hypereutectic compositions.

Indeed the concept of purely thermodynamic criteria for glass formation is not a new one[Nash et al., (1988)]. However, the T_0 criterion for metallic glass formation has not been thoroughly investigated partly because previous solution-based models have not been adequate for accurate prediction of the T_0 temperature for metallic alloys. Our present study demonstrates that by combining a CALPHAD approach with first-principles methods for reliable computation of energies, more accurate and comprehensive description of alloy phases can be achieved.

While rudimentary thermodynamic treatments have shown promise in this regard, it should be noted that the above analysis does not account for the kinetics of partitionless solidification. Several investigators have combined thermodynamic models with models for crystallization kinetics to assess critical cooling rates[Uhlmann (1972)] and composition ranges for glass formation[Nash et al., (1988); Saunders et al., (1986)]. Zhu et al., (2004) incorporated existing thermodynamic treatments into analytical kinetic models to quantify nucleation and growth rates as a function of alloy composition for four Al-RE alloys. In each case, they assume equilibrium chemical partitioning and compute the time (τ) required for transformation of a

"minimal" (10^{-6}) volume fraction as a function of composition. For the Al-Ce and Al-Gd systems, their results for T=500K show a strong correlation between long transformation times and experimental observation of glass formation. Less agreement is observed for Al-Y, and rather poor agreement for Al-Nd. The good agreement between our results based on simple T_0 considerations with these more elaborate calculations and the observed experimental glass formation compositions indicates that the dominant factor affecting glass formation is the limitation of material diffusion in the liquid in these systems. If this premise, supported here by our results for several Al-RE alloys, turns out to be true for a large class of materials, favorable glass formation composition ranges could be estimated using purely thermodynamic models. Extension of our calculations into alloys with more components would be very interesting to test this hypothesis.

2.4 Conclusion

In conclusion, while accurate modeling of crystallization kinetics will ultimately be essential for reliable prediction of glass formation tendency over wide ranges of composition, it is scientifically prudent to examine, more completely, the implications of thermodynamic treatments before attempting to apply rigorous kinetic models. Indeed, any reliable kinetic treatment must include accurate thermodynamic descriptions of the relevant phases, including the undercooled liquid, and must account for the formation of the crystalline phase(s) over a continuous range of permissible compositions. Moreover, we must recognize that relaxation kinetics are integrally linked to the phenomenon of phase selection itself and that the composition of the crystalline phase is a degree of freedom that nature may explore in her quest for more efficient transitions. From a temporal viewpoint, the T_0 condition defines a completely partitionless limit to this behavior where the requirement for long range diffusion vanishes. Clearly, as a fundamental limit in terms of both system thermodynamics ($\Delta G = 0$) and system kinetics, we assert that accurate calculation of such limits should precede more convoluted treatments, where the natural selection of the dynamical transformation path, itself, becomes a critical variable.

CHAPTER 3. CLUSTER-IN-JELLIUM MODEL FOR METALLIC GLASSES

3.1 Introduction

Short range order in undercooled metallic liquids plays an essential role in glass formation in these systems. Many experiments using scattering and absorption techniques have been employed to study this problem. Meanwhile, computer simulations have also been widely used to track the atomic structure evolution in liquid metallic alloys. As a result of these efforts, local cluster structures for some model binary systems have been demonstrated[Sheng et al., (2006)]. Experimentally, it has been observed that the glass-forming ability of various systems are quite sensitive to their chemical compositions. This implies that the energetics and packing of local clusters may be a dominant factor in the glass-formation process. With the fast development of computational capabilities, calculations of isolated clusters is now a mature procedure. However, the energies and local structures of clusters in supercooled liquid or glass could be very different from isolated clusters due to the different environments. For instance, the structures of Si clusters with hydrogen passivation are tremendously different from those of free Si clusters[Tang et al., (2006)]. In fact, the passivation of metallic clusters is still an unresolved problem[Garzón et al., (2000)].

In this paper, we use a mean field approach to calculate the energetics of local clusters in supercooled metallic liquid or glass by studying clusters embedded in an effective jellium background. There are many studies on bonding properties of elemental metals using jellium approaches [Puska et al., (1981); Utreras-Diaz et al., (1984); Perdew et al., (1990); Shore et al., (1991); Rose et al., (1991); Puska et al., (1991)]. The difference of our present approach from previous jellium studies (e.g. Puska's atom-in-jellium model[Puska et al., (1981, 1991)])

is that, in our embedding scheme, we consider a volume around the atom or cluster where the jellium background is excluded. The size of the excluded volume is determined by minimizing the total system energy. Our jellium-passivation calculations yield good agreement with the cohesive energies and atomic volumes obtained from bulk calculation. The site- and angular-momentum- projected density of states (PDOS) from the jellium-passivation approach are also in good agreement with bulk results. Calculations for clusters with increasing size show that jellium-passivation gives good estimates for the bulk limit of large clusters. We believe the jellium-passivation approach to be a promising method to provide useful energetic information about the glass formation tendency of various liquid metal systems. It may be further improved for incorporation in local molecular dynamics simulations which can concentrate on the evolution of short-range or medium-range order in such systems while maintaining a reasonable simulation size.

3.2 Model and Formalism

A local cluster in supercooled liquid or glass is modeled as a cluster surrounded by jellium corresponding to the liquid metal environment in a mean-field approach, as illustrated in Fig.3.1(A). The central circle represents the cluster, surrounded by an empty space representing the optimized volume occupied by the cluster. The most outside region is the effective jellium background representing the electron sea coming from the liquid metal environment. Following the notations of the classic paper by Ihm et al., (1979), the total energy for the jellium-passivated cluster under DFT pseudopotential framework in Rydberg units can be expressed as ($\hbar = 2m_e = e^2/2 = 1$ from Gaussian units to Rydberg units)

$$E_{tot} = T + V + \int E_{xc}(\mathbf{r}) d^3\mathbf{r} - m_0 \epsilon_{jel}(n_0) \tag{3.1}$$

where T is the kinetic energy of the whole system,

$$T = \sum_n \int f_n \psi_n^*(\mathbf{r})(-\nabla^2)\psi_n(\mathbf{r}) d^3\mathbf{r} \tag{3.2}$$

V is the electrostatic potential energy,

$$\begin{aligned} V = & \sum_{n,i,l} \int f_n \psi_n^*(\mathbf{r}) U_{ps,l}(\mathbf{r}-\mathbf{R}_i) \widehat{P}_l \psi_n(\mathbf{r}) d^3\mathbf{r} \\ & + \frac{1}{2} \iint \frac{2\rho(\mathbf{r})\rho(\mathbf{r}')}{|\mathbf{r}-\mathbf{r}'|} d^3\mathbf{r} d^3\mathbf{r}' + \int v(\mathbf{r}) n_e(\mathbf{r}) d^3\mathbf{r} \\ & + \frac{1}{2} \sum_{\substack{i,j \\ i \neq j}} \frac{2Z^2}{|\mathbf{R}_i - \mathbf{R}_j|} + \sum_i \int \frac{2Z n_b(\mathbf{r})}{|\mathbf{r}-\mathbf{R}_i|} d^3\mathbf{r} \end{aligned} \tag{3.3}$$

and E_{xc} is the exchange-correlation energy. m_0 is the total number of electrons contributed by the jellium. $\epsilon_{jel}(n_0)$ gives the energy per electron in bulk jellium with density of n_0, which can be expressed analytically[Perdew (2003)]. n is the index for both wavevector $\mathbf{k}$ and band. Index i and j run over all the atomic lattice sites. $\sum_l U_{ps,l}(\mathbf{r}-\mathbf{R}_\mu)\widehat{P}_l$ is angular momentum-dependent pseudopotentials, where $\widehat{P}_l$ is the projection operator on angular momentum l. f_n specifies the occupancy of quantum state n. $v(\mathbf{r}) = v_0\gamma(\mathbf{r})$. v_0 is the constant electron chemical potential shift for the jellium background. $\gamma(\mathbf{r})$ is a step function which is one in jellium and zero outside. $n_b(\mathbf{r}) = n_b^0\gamma(\mathbf{r})$. n_b^0 is the positive background charge density, $n_b(\mathbf{r})$ is position-dependent because of the excluded volume in our model. $n_e(\mathbf{r}) = \sum_n f_n\psi_n^*(\mathbf{r})\psi_n(\mathbf{r})$ is the total electron density including the contributions from the cluster and jellium, and $\rho(\mathbf{r}) = n_e(\mathbf{r}) - n_b(\mathbf{r})$. The first term in Eq.3.3 describes the interaction between total electron n_e and ion cores. For simplicity, the formalism is given for a single-element cluster. It can be easily generalized to multi-element clusters. Assuming that the positive background charge does not overlap with the pseudopotential's core region where the Coulomb potential is smoothed, the expression for V can be written as

$$\begin{aligned} V = & \int V_{ion+jel}(\mathbf{r}) n_e(\mathbf{r}) d^3\mathbf{r} \\ & + \sum_{n,i,l} \int f_n \psi_n^*(\mathbf{r}) U'_{ps,l}(\mathbf{r}-\mathbf{R}_i) \widehat{P}_l \psi_n(\mathbf{r}) d^3\mathbf{r} \\ & + \frac{1}{2} \iint \frac{2\rho(\mathbf{r})\rho(\mathbf{r}')}{|\mathbf{r}-\mathbf{r}'|} d^3\mathbf{r} d^3\mathbf{r}' \\ & - \int V_{ion}^{loc}(\mathbf{r}) n_b(\mathbf{r}) d^3\mathbf{r} + \frac{1}{2} \sum_{\substack{i,j \\ i \neq j}} \frac{2Z^2}{|\mathbf{R}_i - \mathbf{R}_j|} \end{aligned} \tag{3.4}$$

Where $V_{ion+jel} = V_{ion}^{loc} + v(\mathbf{r})$. V_{ion}^{loc} is the pure local pseudopotential. $U'_{ps,l}$ denotes the angular momentum-dependent nonlocal part of the pseudopotential. The corresponding one-particle Schrödinger equation is

$$\begin{aligned}&\Big(-\nabla^2 + \sum_{i,l} U'_{ps,l}(\mathbf{r}-\mathbf{R}_i)\widehat{P}_l + V_{ion+jel}(\mathbf{r}) \\ &+ \int \frac{2\rho^{in}(\mathbf{r}')}{|\mathbf{r}-\mathbf{r}'|}d^3\mathbf{r}' + \mu_{xc}^{in}(\mathbf{r})\Big)\psi_n(\mathbf{r}) = \epsilon_n\psi_n(\mathbf{r}) \end{aligned} \tag{3.5}$$

Where μ_{xc} is the exchange-correlation potential. Based on the solution of the Schrödinger equation, the total energy can be expressed as a variational functional of the output electron density only[Pickett (1989)]:

$$\begin{aligned}E_{tot} = &\sum_n f_n\epsilon_n - \int \frac{2\rho^{in}(\mathbf{r})n_e^{out}(\mathbf{r})}{|\mathbf{r}-\mathbf{r}'|}d^3\mathbf{r}d^3\mathbf{r}' \\ &- \int \mu_{xc}^{in}n_e^{out}(\mathbf{r})d^3\mathbf{r} + \frac{1}{2}\int \frac{2\rho^{out}(\mathbf{r})\rho^{out}(\mathbf{r})}{|\mathbf{r}-\mathbf{r}'|}d^3\mathbf{r}d^3\mathbf{r}' \\ &+ \int \epsilon_{xc}^{out}(\mathbf{r})n_e^{out}(\mathbf{r})d^3\mathbf{r} - \int V_{ion,loc}(\mathbf{r})n_b(\mathbf{r})d^3(\mathbf{r}) \\ &+ \frac{1}{2}\sum_{\substack{i,j \\ i\neq j}} \frac{2Z^2}{|\mathbf{R}_i-\mathbf{R}_j|} - m_0\epsilon_{jel}(n_0)\end{aligned} \tag{3.6}$$

In the momentum space representation, the total energy is

$$\begin{aligned}E_{tot} = &\sum_n \epsilon_n f_n + \Omega\Big(-\sum_{\mathbf{G}} V_{Coul}^{in}(\mathbf{G})n_e^{out}(\mathbf{G}) \\ &- \sum_{\mathbf{G}} \mu_{xc}^{in}(\mathbf{G})n_e^{out}(\mathbf{G}) + \frac{1}{2}\sum_{\mathbf{G}} V_{Coul}^{out}(\mathbf{G})\rho^{out}(\mathbf{G}) \\ &+ \sum_{\mathbf{G}} \epsilon_{xc}^{out}(\mathbf{G})n_e^{out}(\mathbf{G}) - \sum_{\mathbf{G}} V_{ion,loc}(\mathbf{G})n_b(\mathbf{G})\Big) \\ &+ \frac{1}{2}\sum_{\substack{i,j \\ i\neq j}} \frac{2Z^2}{|\mathbf{R}_i-\mathbf{R}_j|} - m_0\epsilon_{jel}(n_0)\end{aligned} \tag{3.7}$$

where $V_{Coul} = 8\pi\rho(\mathbf{G})/\mathbf{G}^2$. By the same argument as Ihm et al., (1979), finally the total energy per unit cell can be expressed as

$$E_{tot,cell} = \frac{1}{N}\sum_n \epsilon_n f_n + \Omega_{cell}\Big(-\sum_{\mathbf{G}} V'^{in}_{Coul}(\mathbf{G}) n_e^{out}(\mathbf{G}) - \sum_{\mathbf{G}} \mu^{in}_{xc}(\mathbf{G}) n_e^{out}(\mathbf{G}) + \frac{1}{2}\sum_{\mathbf{G}} V'^{out}_{Coul}(\mathbf{G})\rho^{out}(\mathbf{G}) + \sum_{\mathbf{G}} \epsilon^{out}_{xc}(\mathbf{G}) n_e^{out}(\mathbf{G}) - \sum_{\mathbf{G}} V'_{ion,loc}(\mathbf{G}) n_b(\mathbf{G})\Big) + \alpha_1 Z + \gamma_{Ewald} - \frac{m_0}{N}\epsilon_{jel}(n_0) \tag{3.8}$$

V' indicates the term with $G = 0$ set to be zero, which is equivalent to a constant shift of the potential.

The above formalism is incorporated into our pseudopotential mixed-basis code[Louie et al., (1979); Ho et al., (1992)]. Norm-conserving pseudopotentials are generated with the method by Troullier et al., (1991). For transition metals, the localized character of d electrons can be efficiently expressed by including truncated atomic pseudo-wavefunctions in the basis set in addition to plane waves. The exchange-correlation potential is based on the generalized gradient corrections parametrized by Perdew et al., (1996). The calculations are done in the supercell approach with a cubic unit cell of length 20 Bohr. The plane wave cut-off energy is 20 Ry. A Gaussian smearing width of 0.06 eV is used for the Brillouin zone integration on a $6 \times 6 \times 6$ Monkhorst-Pack grid. The jellium boundary is smoothed by Fermi smearing with width of 0.05 Bohr to remove high Fourier components.

3.3 Results and discussion

3.3.1 Single atom embedded in jellium

The excluded volume occupied by an atom in our model can be understood by considering the pair distribution function g(r) in liquid or glass. Fig.3.1(B) shows a typical pair distribution function of liquid Al(dark grey area), which describes the average environment of an Al atom in the liquid. In a mean field approach, the environment can be approximated as an effective

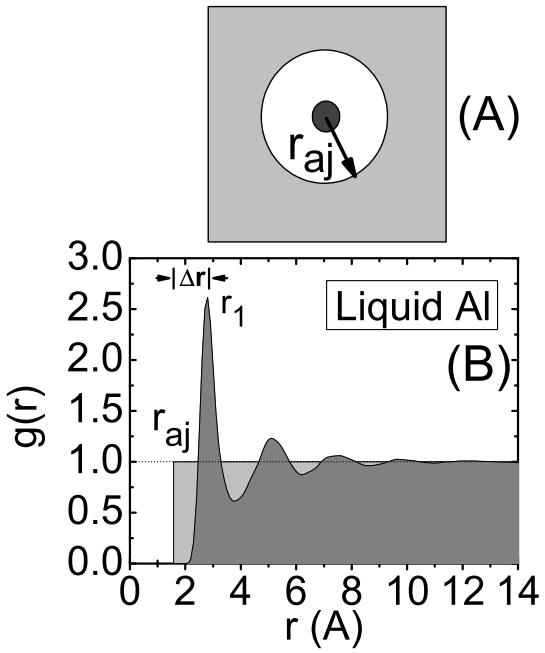

Figure 3.1 (A) Schematic representation of the our cluster-in-jellium model. (B) Dark grey area: pair distribution function of liquid aluminum; light grey area: uniform jellium as an approximation for the liquid metallic environment.

jellium(light grey area). The optimised atom-jellium spacing, r_{aj}^{o}, must be smaller than the first peak position of the pair distribution function, r_1, from mass conservation.

The jellium density parameter could be obtained from the average interstitial electron density from LDA calculations [Moruzzi et al., (1978)]. It was known that bare jellium model failed qualitatively to describe the energetics of metals, e.g., the predicted surface energy could be negative for large electron density[Lang et al., (1970)]. Utreras-Diaz and Shore showed that this shortcoming of the jellium model can be corrected by adding a constant shift, v_0, to the electron potential of the jellium background[Utreras-Diaz et al., (1984)]. We follow the simple procedure outlined in ref.[Shore et al., (1991); Rose et al., (1991)] to estimate v_0 from jellium density, $v_0 = -n_0 \left[\frac{\partial \epsilon_{jel}}{\partial n}\right]_{n_0}$. In the case of Aluminum, using the chemical potential shift of -0.17 Ry from ref.[Rose et al., (1991)], we obtained 2.92 Bohr for the optimized atom-jellium distance. This is fairly close to the Wigner-Seitz radius of bulk Al (2.99 Bohr). Fig.3.2 shows

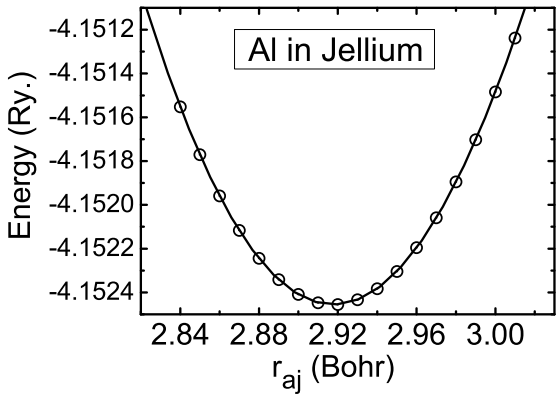

Figure 3.2 The total energy of Al atom passivated by jellium as a function of the distance between the atom and the jellium boundary, r_{aj}.

a typical result of the total energy of an Al atom embedded in jellium with respect to the atom-jellium spacing, r_{aj}, which is well fitted by a third order polynomial function. A good correlation between r^o_{aj} and Wigner-Seitz radius, $R_{W.S.}$, for nine simple metals is shown in Fig.3.3. The cohesive energies of the simple metals from the jellium passivation approach, E_j, are also compared with the bulk results, E_B, as shown in Fig.3.4. Similar trend was observed from other jellium approach[Rose et al., (1991); Puska et al., (1991)]. Such good agreement suggests that the jellium background is a good approximation of the bulk environment for simple metals.

In order to gain deeper insight into jellium passivation, we also compared the angular-momentum projected DOS of Al in jellium passivation approach with the bulk result, as shown in Fig.3.5. 2.99 Bohr is selected to be the radius of the atomic sphere for the integration of the wave functions and yields 3.0 electrons in both cases. The fairly good match reveals the essential physical justification of jellium passivation for Al.

3.3.2 Clusters embedded in jellium

To generalize the treatment of single atom in jellium to clusters in jellium we need to determine the shape and position of the jellium boundary. In the case of a single atom, the

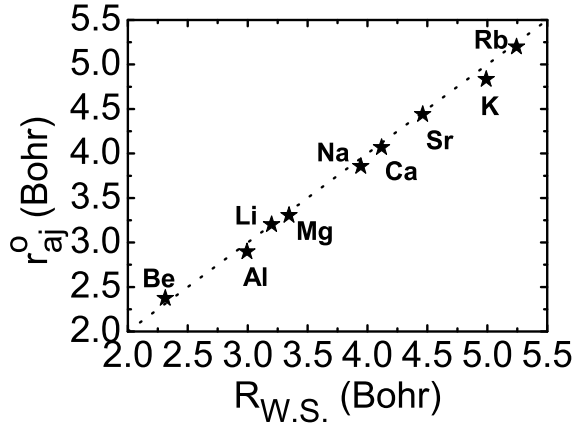

Figure 3.3 Correlation between the optimised atom-jellium distance, r^o_{aj}, and the Wigner-Seitz radiu, $R_{W.S.}$, for nine simple metals.

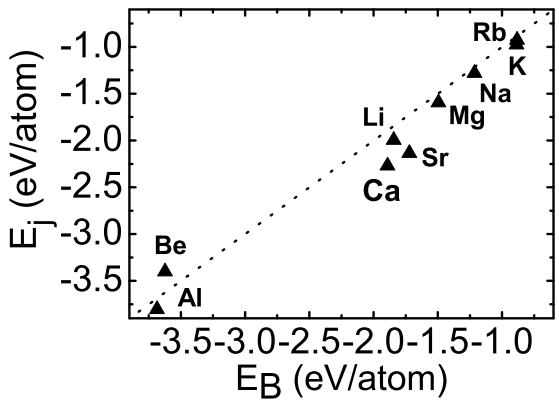

Figure 3.4 Correlation between the cohesive energies of the simple metals from the jellium passivation approach, E_j, and those from bulk calculation, E_B.

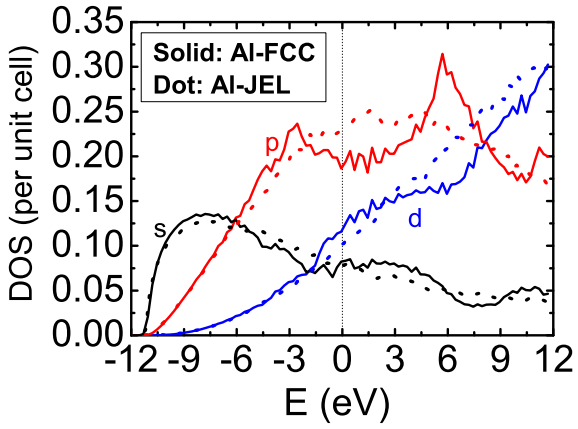

Figure 3.5 Angular momentum-projected density of states (PDOS) for Al in FCC crystal structure (solid line) and embedded in jellium (dots).

shape of the jellium boundary is taken to be spherical. In our calculations, we want the jellium to represent the embedding environment and want the jellium background to be kept away from the "inside" region of the cluster. The simplest generalization of the treatment for single atom in jellium is to empty a spherical region with optimized atom-jellium radius centered at each atom in the cluster. However, because the volume per spherical region is similar to the volume per atom and there are significant overlaps in the spheres centered on different atoms in the cluster, this approach does not remove enough space from inside the cluster and allows some pockets of jellium to persist inside the cluster, as shown in Fig.3.6(a). Also the resulting boundary exhibits sharp cusps at the spherical intersections leading to high Fourier components not easy to remove. We found an approach which works better is to follow a "push-pull" strategy, which is physically motivated by the pair distribution function in Fig.3.1(B): jellium is first pushed outward to a nearest-neighbor distance (corresponding to r_1 the nearest-neighbor peak position in g(r)) from each atom in the cluster and then pulled inward $\Delta r = r_1 - r_{aj}$ from the initial boundary, as shown in Fig.3.6(b). The advantages of the "push-pull" strategy are: (a) smooth jellium boundaries good for Fourier transform; (b) no jellium inside the cluster; (c) jellium boundary reflects the morphology of cluster's surface

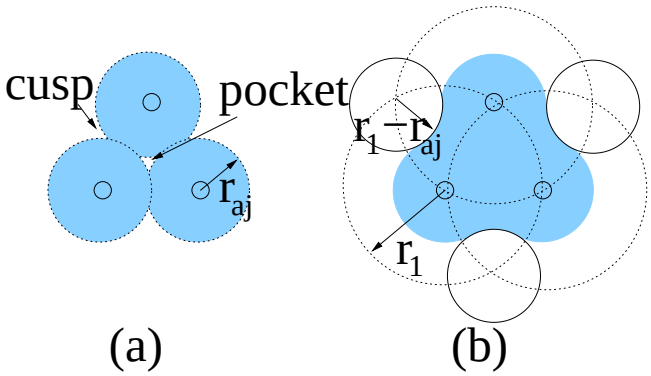

Figure 3.6 Schematic illustration of the jellium boundaries for an Al-trimer. (a) Simplest generalization of single atom in jellium treatment results in pockets and cusps. (b) "Push-pull" strategy for jellium boundary construction. Shaded (light-blue online) area corresponds to the region where jellium is excluded.

which is desired physically.

Five-fold icosahedral local order has been linked with the short range and medium range order in metallic glass system[Sheng et al., (2006)]. Local icosahedral clusters may serve as competitors against possible nuclei for crystallization. Thus, an interesting question is the relative stability of the icosahedral cluster and a crystal nucleus inside an undercooled liquid metal system and how well it correlates with the glass forming ability (GFA) of the metallic liquid. Here we choose a series of Al-X (X=Na, K, Mg, Ca, Sr, Al, Si, Ge, Sn, Ni, Mo, Zn, Zr, Pt, Pd, Cu, Ag, and Au) binary alloys and examine the energy difference of local icosahedral clusters and FCC embryos in a jellium environment approximating liquid Al. The local icosahedral cluster for Al-X liquid is an Al_{13} icosahedral cluster with central atom replaced by a solute atom X. Similarly, the FCC embryo is a pure solvent Al_{13} FCC fragment with central atom replaced by a solute atom X. Fig.3.7 shows the energy difference between the icosahedral clusters and FCC fragments of Al-X liquid with jellium passivation. The energy differences for free clusters with one shell of Al ($Al_{12} + X$) and two shells of Al ($Al_{54} + X$), are also shown. Spin polarization effects are found to be negligible for the systems studied in this paper. Good correlation exists between the jellium-passivation results, $E_{I-F,jel}$, and those by adding one more shell of Al atoms, $E_{I-F,2-shell}$ shown in Fig.3.8. The free clusters

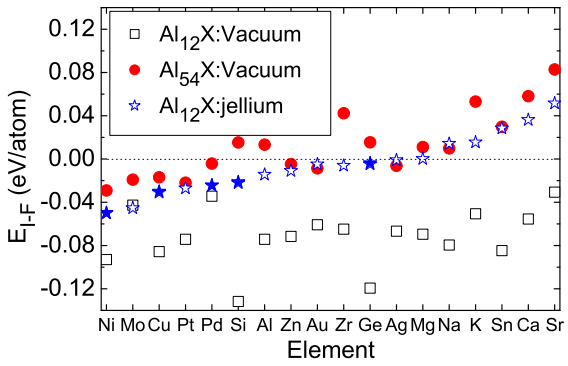

Figure 3.7 Energy difference between icosahedral clusters and FCC fragments of Al with central atom replaced by X (Ni, Mo, ...) with jellium passivation, which is a good estimate of the bulk limit of non-isolated clusters as shown by the trend in the energy differences for free clusters with one shell of Al (Al_{12}+X) and two shells of Al (Al_{54}+X). Solid star represents the system where coexistent amorphous and crystalline phases have been observed experimentally.

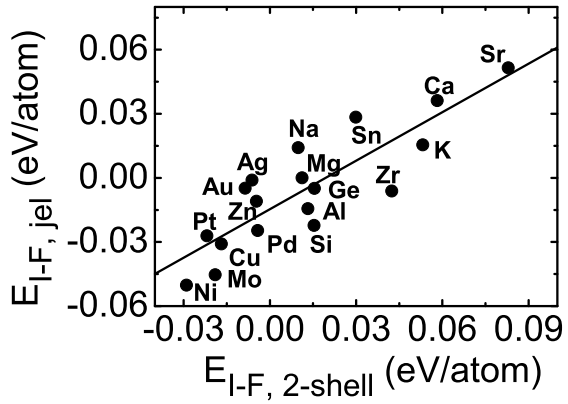

Figure 3.8 Correlation between the energy differences of icosahedral cluster and FCC fragment in jellium passivation approach ($E_{I-F,jel}$) and those by adding one more shell of Al atoms ($E_{I-F,2-shell}$). The solid line is a linear least squares fitting of the data.

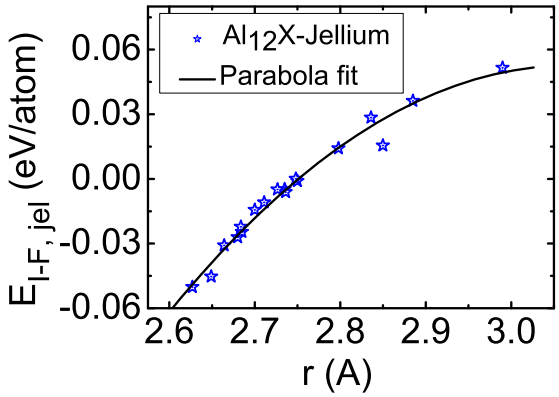

Figure 3.9 The energy difference as a function of the distance between the central atom, X, and outer shell Al atom.

calculation results show that the behavior of the energy difference approaches the clusters-in-jellium results as the free clusters increase in size. This suggests the jellium-passivated result is a good estimate of the energy behavior of the cluster inside a liquid metal system.

Looking at the trend of the energy differences for the various choices of X, we found a good correlation with the size of the center atom (Fig.3.9). This suggests that smaller atoms allow for a more efficient packing for the icosahedral cluster[Ashman et al., (1997)] relative to the fcc embryo structure. Experimentally, coexistent amorphous and crystalline phases have been observed in Al-Si[Predecki et al., (1965)], Al-Ge[Ramachandrarao et al., (1972)], Al-Cu[Davies et al., (1972)], Al-Ni[Chattopadyay et al., (1976)] and Al-Pd[Sastry et al., (1978)], corresponding to a region of negative $E_{I-F,jel}$ in Fig.3.7. Thus, the energy difference between icosahedral cluster and FCC embryos with jellium passivation may serve as an indication for GFA of Al-rich liquid metallic alloys.

In many cases, the glass transformations of liquid metal alloy systems are very sensitive to the addition of small amounts of impurity atoms [Wang Wei Hua (2007)]. A fundamental understanding of the role of the small amount of added material is critical for a successful theory of glass transformation. Our cluster-in-jellium model could be further developed to study the effects of low-concentration impurity atoms on the energetics, structures and dynamical

behavior of important local clusters without the use of large unit cell calculations.

3.4 Conclusion

We have used a model of clusters embedded in jellium to study short-range ordering in supercooled liquid and glass systems in a mean field approach. The model was first verified by the good agreement between the single atom in jellium results and those from bulk calculations. The PDOS of Al atom embedded in jellium matches very well with bulk result. Application of the model to Al-X metallic liquid shows that cluster passivated by jellium is a reasonable estimate for the bulk limit. Furthermore, the energy differences between icosahedral clusters and FCC embryoes are related with the GFA of the metallic liquids. The model may be further developed to study a critical issue of glass formation–the effect of minor addition of other chemical elements on the glass behavior of liquid metal alloys system.

CHAPTER 4. *AB INITIO* TIGHT-BINDING CALCULATIONS

4.1 Introduction

First-principles methods based on density functional theory(DFT)[Kohn et al., (1964)] and plane wave basis[Ihm et al., (1979); Payne et al., (1992)] have been well developed over the past four decades and very successful in calculating the electronic structure and total energy of many systems. Nevertheless, due to the complexity of the algorithms and the fact that a large number of basis functions is required in the calculation, many complex structures and materials that require a computational unit cell containing thousands of atoms are still beyond the reach of the first-principles plane-wave based DFT methods.

On the other hand, considerable work have been tried to use localized orbitals as basis[Galli et al., (1992); Mauri et al., (1993); Ordejon et al., (1993); Kim et al., (1995); Hernandez et al., (1995); Koepernik et al., (1999); Soler et al., (2002)] in order to reduce the dimension of the Hamiltonian matrix, so that a large number of atoms can be handled in the calculation. It has also been shown that O(N) scaling in the first-principles calculations (i.e., the computational work load scales linearly with the number of atoms in the calculation) can be achieved by using a set of well-localized orbitals as basis[Galli et al., (1992); Mauri et al., (1993); Ordejon et al., (1993); Kim et al., (1995); Hernandez et al., (1995); Soler et al., (2002)]. However, the efficiency and accuracy of the calculations in this approach strongly depend on the choice of basis orbitals. In many cases, accurate calculations would require a basis set consisting of a large number of localized orbitals which slow down the calculations considerably[Soler et al., (2002)]. Thus it is highly desirable to have a set of localized minimal basis orbitals that can faithfully produce the converged electronic structure.

Recently two independent approaches, i.e., the maximally localized Wannier functions ap-

proach by Marzari et al., (1997) and the quasi-atomic minimal basis set orbitals(QUAMBOs) approach by Lu et al., (2004); Wang et al., (2004); Qian et al., (2008) demonstrated that highly localized minimal basis set orbitals can be constructed through unitary transformations of the wavefunctions obtained from fully self-consistent first-principles calculations with large basis set. These minimal basis set orbitals are atomic-like but deform according to the bonding environment, and can span exactly the same preserved electronic subspace as the full-basis first-principles calculations. These minimal basis sets would serve as a promising platform for developing an efficient yet accurate method for large scale electronic calculations.

In this chapter, we show that accurate tight-binding Hamiltonian and overlap matrix elements can be calculated by first-principles methods through the QUAMBO representation of electronic structure at different local bonding environments. By sampling various local bonding environments of a large complex system from a series of first-principles calculations of smaller systems, the "exact" environment-dependent tight-binding matrix of the large system can be assembled directly from a first-principles approach without resorting to the usual fitting procedure to generate tight-binding parameters.

4.2 Method and formalism

A set of free atomic orbitals $\{|A_\alpha\rangle\}$ (may be modified) are first chosen, which has a one-to-one correspondence to the quasiatomic orbitals $\left\{\left|\tilde{A}_\alpha\right\rangle\right\}$. α is a composite label for the orbital type ($s, p_x, p_y, p_z, etc.,$) for each atom in the unit cell. $\{|\psi_{\mathbf{k}\mu}\rangle\}$ is a complete set of Bloch eigenstates obtained from first-principles calculations using a large basis set of dimension N_{BS}, with the eigenstates being labeled by the wave vector $\mathbf{k}$ in the Brillouin zone and the band number μ, we want to construct a set of quasiatomic orbitals $\left\{\left|\tilde{A}_\alpha\right\rangle\right\}$ by linear combinations of the Bloch eigenstates. For each wave vector $\mathbf{k}$, we have a total of N_{BS} bands, with $n_{occ}(\mathbf{k})$ of them intended to be preserved and the rest $n_{vir}(\mathbf{k})$ are of no interest. However, only a subspace of the rest bands is needed and this subspace should be optimized in order to enhance the localization of the QUAMBOs when combined coherently with the preserved bands. This

optimal subset of virtual bands $|\psi_{\mathbf{k}p}\rangle$ may be obtained by a linear transformation:

$$|\psi_{\mathbf{k}p}\rangle = \sum_{\mu=n_{occ}+1}^{N_{BS}} T_p^{\mu\mathbf{k}} |\psi_{\mathbf{k}\mu}\rangle, p = 1, 2, ..., n_p(\mathbf{k}) < n_{vir}(\mathbf{k}), \tag{4.1}$$

where T-matrix is rectangular to be determined later (see Appendix B) which satisfies $T \cdot T^{\dagger} = I$ since $|\psi_{\mathbf{k}p}\rangle$ is an orthonormal set.

Let the total number of QUAMBOs be N_q. We have $N_q = n_{occ}(\mathbf{k}) + n_p(\mathbf{k})$. To simplify the notations, we define a new set of Bloch wavefunctions $\{|\phi_{\mathbf{k}\mu}\rangle\}$ as the collection of the preserved bands and the optimized virtual bands.

$$|\phi_{\mathbf{k}\mu}\rangle = \begin{cases} |\psi_{\mathbf{k}\mu}\rangle & \cdots if \quad 1 \leq \mu \leq n_{occ}(\mathbf{k}) \\ |\psi_{\mathbf{k}p}\rangle & \cdots p = \mu - n_{occ}(\mathbf{k}), \ if \ n_{occ}(\mathbf{k}) < \mu \leq \mathbf{n}_q \end{cases} \tag{4.2}$$

Thus $\{|\phi_{\mathbf{k}\mu}\rangle\}$ spans the chosen subspace and the quasiatomic orbitals may be expressed as their linear combinations.

$$\left|\tilde{A}_\alpha\right\rangle = \sum_{\mathbf{k}\mu} C_\alpha^{\mathbf{k}\mu} |\phi_{\mathbf{k}\mu}\rangle \tag{4.3}$$

We require each QUAMBO $\left|\tilde{A}_\alpha\right\rangle$ to be as close as possible to its corresponding free-atom orbital $|A_\alpha\rangle$. The minimization of the mean square deviation $\langle \tilde{A}_\alpha - A_\alpha | \tilde{A}_\alpha - A_\alpha \rangle$ under the norm-conserving constraint $\langle \tilde{A}_\alpha | \tilde{A}_\alpha \rangle = 1$ yields(see Appendix A)

$$\left|\tilde{A}_\alpha\right\rangle = D_\alpha^{-1/2} \sum_{\mathbf{k}\mu} |\phi_{\mathbf{k}\mu}\rangle \langle \phi_{\mathbf{k}\mu} | A_\alpha \rangle = \sum_{\mathbf{k}} \left|\tilde{A}_\alpha^{\mathbf{k}}\right\rangle \tag{4.4}$$

where

$$D_\alpha = \sum_{\mathbf{k}\mu} |\langle \phi_{\mathbf{k}\mu} | A_\alpha \rangle|^2 \tag{4.5}$$

$$\left|\tilde{A}_\alpha^{\mathbf{k}}\right\rangle = D_\alpha^{-1/2} \sum_{\mu} |\phi_{\mathbf{k}\mu}\rangle \langle \phi_{\mathbf{k}\mu} | A_\alpha \rangle$$

and is related to the root-mean-square deviation of the optimized $\left|\tilde{A}_\alpha\right\rangle$ from the corresponding free-atom $|A_\alpha\rangle$ by

$$\Delta_\alpha = \langle \tilde{A}_\alpha - A_\alpha | \tilde{A}_\alpha - A_\alpha \rangle^{1/2} = [2(1 - D_\alpha^{1/2})]^{1/2} \tag{4.6}$$

Equation (4.6) suggests that the key step to obtaining quasiatomic localized orbitals is to select a virtual band subset $\phi_{\mathbf{k}p}(\mathbf{r})$ that maximizes the sum $\sum_\alpha D_\alpha$, i.e. maximizing the overall

overlap between the virtual bands and the free-atom orbitals. With the subset of virtual bands chosen according to this criteria, QUAMBOs can be constructed through equation (4.4). The details for constructing optimised virtual bands may be seen in Appendix B.

Once QUAMBOs are obtained, the real space hopping($H^{\mathbf{R}}_{\alpha\alpha'}$) and overlapping elements($S^{\mathbf{R}}_{\alpha\alpha'}$) may be calculated as follows

$$H^{\mathbf{R}}_{\alpha\alpha'} = \left\langle \tilde{A}_{\alpha} \left| H \right| \tilde{A}^{\mathbf{R}}_{\alpha} \right\rangle = \sum_{\mathbf{k}} \left\langle \tilde{A}^{\mathbf{k}}_{\alpha} \left| H \right| \tilde{A}^{\mathbf{k}}_{\alpha'} \right\rangle e^{i\mathbf{k}\cdot\mathbf{R}} \tag{4.7}$$

$$S^{\mathbf{R}}_{\alpha\alpha'} = \left\langle \tilde{A}_{\alpha} | \tilde{A}^{\mathbf{R}}_{\alpha} \right\rangle = \sum_{\mathbf{k}} \left\langle \tilde{A}^{\mathbf{k}}_{\alpha} | \tilde{A}^{\mathbf{k}}_{\alpha'} \right\rangle e^{i\mathbf{k}\cdot\mathbf{R}}$$

where

$$\left\langle \mathbf{r} | \tilde{A}^{\mathbf{R}}_{\alpha} \right\rangle = \tilde{A}^{\mathbf{R}}_{\alpha} \left(\mathbf{r} - \mathbf{R} \right) \tag{4.8}$$

In our scheme for large scale electronic calculation, an overlap or tight-binding Hamiltonian matrix of a big system is built by filling in a set of $n \times m$ "exact" sub-matrices of all pairs of atoms in the system, where n and m are the numbers of minimal basis orbitals for the two atoms in the pair respectively. These $n \times m$ "exact" sub-matrices are calculated from first-principles following the QUAMBO procedure described above. Note that the QUAMBOs and hence the $n \times m$ sub-matrices of tight-binding are dependent of the environment around the pair of atoms, and in principle the $n \times m$ "exact" sub-matrices has to be calculated for every pair of atoms in the system. This can be done by first performing first-principles calculations for a relatively small system which keeps the dominant local environment of the pair of atoms in the big system, then the $n \times m$ tight-binding matrix for this pair of atoms can be constructed following the QUAMBO scheme. This approach will break the first-principles calculations of a big system into many much smaller sub-system calculations. In many cases of interest (e.g., defects in crystals), the bonding environments of many different atom pairs in the big system are essentially the same, therefore, in practice first-principles calculations are needed only for a limited number of smaller systems and an accurate tight-binding overlap and Hamiltonian matrices for the big system can be constructed. The scheme was illustrated with a study of the electronic structure of graphene nano-ribbons.

4.3 Results

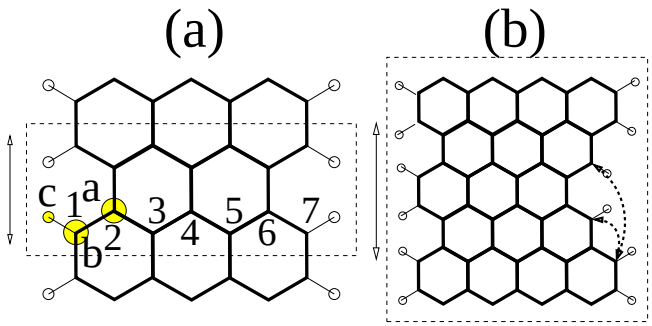

Figure 4.1 (a) N_a=7 A-GNR was chosen to be the training sample for perfect A-GNR. Dotted rectangle indicates the primitive unit cell. The left arrow gives the periodical direction. Atom a, b and c are treated to be three different atoms according to their local environment. (b) Additional training sample for studies on A-GNRs with edge defects.

We first applied our scheme to calculate the electronic structure of perfect armchair-graphene nano-ribbons (A-GNRs) of different widths, where three different types of atoms in the nano-ribbons have been identified as shown in fig.4.1(a): atom a represents a carbon atom inside the ribbon, atom b represents a carbon atom at the edge, and atom c is a hydrogen atom for passivation. The number of minimal basis orbitals for a carbon atom is 4 (one s and three p) and that for a hydrogen atom is one. Only one training cell of N_a =7 A-GNR as shown in fig.4.1(a) and a single first-principles calculation is needed to extract all the necessary "exact" 4×4 or 4×1 tight-binding matrices for each pair of a-a, a-b, b-b, and b-c atoms from these three types of non-equivalent atoms, respectively. We notice that the same type of atom-pair by our definition (i.e., a-a, a-b, b-b, and b-c) can appear more than once at different locations in the same training cell (or in different training cells) and, strictly speaking, their bonding environments are not exactly the same. But we found the tight-binding hopping elements of the same type of pair are different only on the order of several meV, while the overlapping elements are almost the same. Therefore, we assign the matrix elements to each type of atom-pair in the system by taking an algebraic average over the same type of pairs in

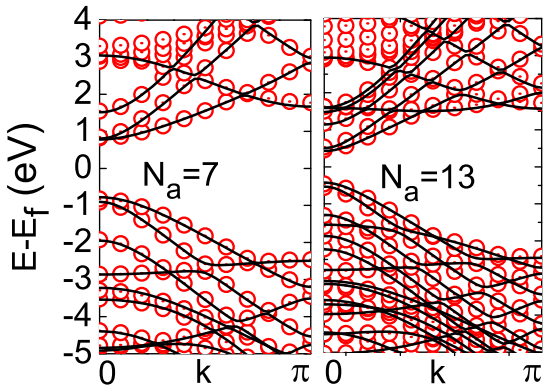

Figure 4.2 Band structures based on the QUAMBO-TB scheme (solid line) compared with DFT results (circle) for A-GNR with N_a=7 and 13.

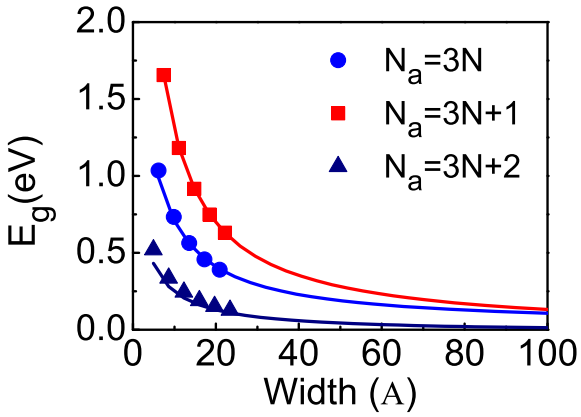

Figure 4.3 TB band gap (solid lines) of A-GNR with different size compared with DFT results (symbols).

the training cells. All the occupied states and some $\pi*$-antibonding states upto 4 eV above the fermi level are preserved in the QUAMBO construction. Fig.4.2 shows the band structures for A-GNRs with width $N_a = 7$ and 13 (solid lines) from the QUAMBO-tight-binding scheme using small 4×4 and 4×1 tight-binding matrices generated from the N_a =7 training cell as described above. The results from full first-principles calculations (circle) were also shown for comparison. One can see that the QUAMBO-TB band structures agree very well with the full first-principles results in the targeted energy window. One may observe some additional DFT bands between 3 eV and 4 eV above fermi level. These bands are dominated by higher angular momentum characters, so they are not covered by the tight-binding results with minimal basis(s,p). (However, one can always include more orbitals in QUAMBO construction to capture these relatively higher-energy bands if desired.) The electronic band gap variation of a perfect A-GNR as a function of the width of the nanoribbon has also been studied. Fig.4.3 shows the oscillation of the band gap with a period of N_a =3 obtained from our QUAMBO-TB scheme, which agrees very well with the results from first-principles calculations[Son et al., (2006)]. The efficiency of the QUAMBO-TB scheme enables us to calculate the electronic structure of much wider graphene nano-ribbons, as one can also see from fig.4.3, where the band gap of nanoribbons up to 100 Å in width has been calculated with our QUAMBO-TB method.

The QUAMBO-TB scheme also enables us to study the electronic structure of graphene nano-ribbons with random defects. For the purpose of illustration, we have studied the electronic structures of N_a=6 A-GNR with random edge defects on one edge of the ribbon at different concentrations. We first constructed a supercell of N_a=6 A-GNR by repeating the primitive unit cell 100 times(containing 1200 carbon atoms). The edge defects were generated by randomly removing pairs of carbon atoms on one side as shown in fig.4.4(a). The new structures were passivated with hydrogen atoms. For this defect system, some additional QUAMBO-TB matrix elements around the edge defects are needed. We used another training cell as shown in fig.4.1(b) to obtain these additional matrix elements, where the curved arrows indicate the new matrix elements between these sites to be added to the existing QUAMBO-TB matrix elements database from the $N_a = 7$ training cell as discussed above. Based upon

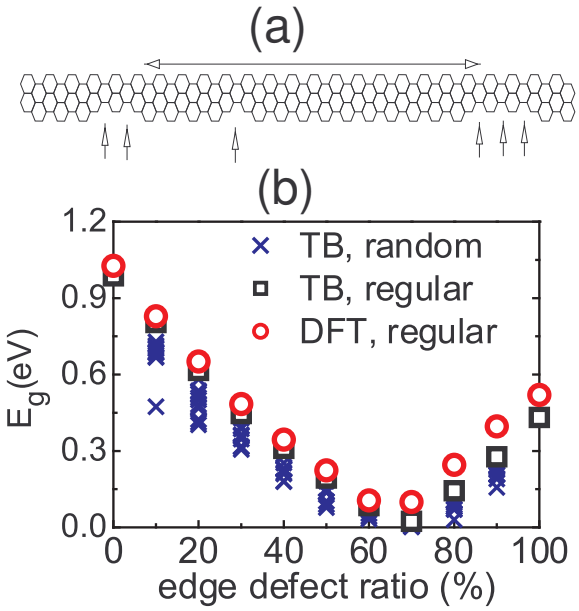

Figure 4.4 (a) Schematic view of a part of a supercell of N_a=6 A-GNR containing more than one thousand atoms with edge defects randomly distributed on one side. Small arrows indicate the edge defetcts. (b) Band gap behavior of the defected N_a=6 A-GNR with increasing edge defects ratio. The perfect N_a=6(5) A-GNR corresponds to a defect ratio of 0%(100%). Crosses are the results from supercells (containing 100 primitive unitcells of perfect A-GNR) with random edge defects. Squares(circles) are TB(DFT) results from smaller supercells (containing 10 primitive unitcells of perfect A-GNR) with regular edge defects by removing pairs of carbon atoms successively on one side.

this set of QUAMBO-TB matrix elements from first-principles calculations performed on two small unit cells as shown in fig.4.1, actual tight-binding overlap and Hamiltonian matrices for the defected graphene nano-ribbons at various defect concentrations can be constructed, and the electronic structure of A-GNRs with random edge defects can be studied. The results of the band gap as a function of defect ratio in the N_a=6 A-GNR are shown in fig.4.4(b). The random distribution of the edge defects gives some variation of the band gap at each defect concentration, however, there exists a general trend of the band gap with increasing defect concentration. The band gap reaches its minimum (which is quite small) at a defect ratio of 70%. This implies that edge defects have a significant effect on the electronic structures of A-GNRs, which is consistent with observations from experiments[Han et al., (2007)]. In order to verify the accuracy of our QUAMBO-TB approach for studying the A-GNR with edge defects, we compared the QUAMBO-TB and DFT results of band gap as a function of the edge defect ratio for a N_a=6 A-GNR with the edge defects regularly arranged in a much smaller supercell (so that DFT calculations can be easily performed). The lattice vector along the ribbon direction is only 10 times that of the primitive unit cell of a N_a=6 A-GNR. The edge defects were constructed by removing pairs of carbon atoms successively on one side of the ribbon so that all the edge defects stay together in the supercell. The results are also shown in fig.4.4(b) where the open squares represent the results from our QUAMBO-TB and the open circles represent the results from full-basis DFT calculations. The results from the TB and the DFT agree with each other very well, indicating that the QUAMBO-TB approach we used in this study should be accurate for studying graphene nanoribbons with defects. It is also interesting to note from fig.4.4(b) that randomly distributed edge defects tend to have smaller band gaps as compare to the case of regularly distributed defects at the same defect ratio.

Furthermore, the QUAMBO-TB scheme may also be applied to studies with spin-polarization, where two sets of TB parameters (for spin-up and spin-down) are needed[Qian et al., (2008)]. For demonstration, we applied it to zigzag-graphene nano-ribbons (Z-GNRs) which have a ground state with a spin configuration of FM-A, i.e., the coupling of spins is of ferromagnetic

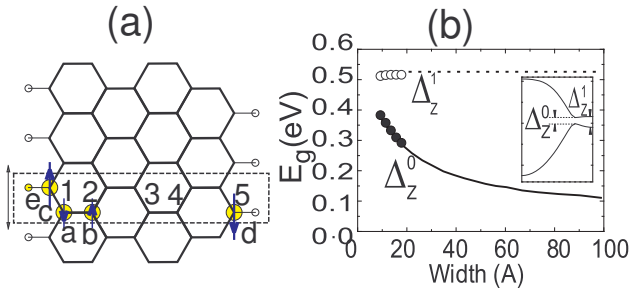

Figure 4.5 (a) The training sample for Z-GNRs. (b) TB band gap (solid lines) of Z-GNR with different size compared with DFT results (symbols).

type at each edge and of antiferromagnetic type between the two edges[Nakada et al., (1996); Son et al., (2006); Martins et al., (2007)]. Five different types of atoms in the nano-ribbons have been identified as illustrated in fig.4.5(a), where atom a(b) represents a carbon atom inside the ribbon with spin-down(up) majority, atom c(d) represents a carbon atom at the edges with spin-up(down) majority, and atom e is a hydrogen atom for passivation. Only one training sample of N_z =5 Z-GNR as shown in fig.4.5(a) and a single first-principles calculation with local spin density approximation are needed to extract all the spin-up and spin-down tight-binding matrices for these five types of non-equivalent atom. Fig.4.5(b) shows the band gap hehaviour of Z-GNRs with width up to 100 Å. Lines are QUAMBO-TB results, which are consistent with DFT calculations indicated by circles[Son et al., (2006)]. It is very straightwforward and advantageous to use our method to study the electronic structures of doped graphene nanrobbons[Martins et al., (2007)] or grephene with adatom adsorption[Duplock et al., (2004); Mao et al., (2008)].

4.4 Discussion

The success of our QUAMBO-based tight-binding divide-and-conquer approach relies on several fundamental physical concepts: local environment-dominance of physical properties,

good localization and enviroment-adaptedness of the minimal basis set orbitals(QUAMBOs). The first locality property in materials is the physical foundation, upon which the order-N methods may be developed[Goedecker (1999)]. For example, in Yang's density-based divide-and-conquer approach, the physical system may be divided into a few subsystems[Yang (1991)]. And the charge density of each subsystem can be calculated separately. In our approach, the locality property ensures that a small training cell which keeps local environment of certain atom pairs in big systems may be constructed. However, the exact size of the training cell depends on the specific systems. The training cell is expected to be relatively big for metallic systems.

The good localization and environment-adaptedness of QUAMBOs makes the derived tight-binding parameters short-ranged as well as exact. Namely, the converged electronic structure with respect to basis set may be exactly downfolded into a short-ranged tight-binding representation, which is pioneered by O. K. Andersen in his Muffin-tin orbitals approach[Andersen et al., (1984)]. Therefore only smaller number of atom pairs and training cells need to be considered. In the case of perfect A-GNRs, one training cell actually contains all the necessary tight-binding parameters.

Our scheme does not explicitly include the atomic relaxation. However, the lattice distortion effect is readily taken care of by proper choice of training cells. The current scheme is mainly focused on the electronic structure calculation of big systems. The total energy and its derivatives can not be obtained. Hence the total energy calculations and molecular dynamics may not be handled. However, the scheme may be further developed following the way of traditional tight-binding potential development.

4.5 Conclusion

We have demonstrated an efficient and accurate method for calculating the electronic structure of a large system using a divide-and-conquer strategy. First-principles calculations are needed only for small number of atoms around the pairs, yet an accurate QUAMBO-TB matrix can be constructed for the whole system. Such an approach has proved quite successful for

the studies of electronic structures in graphene nano-ribbons. This "QUAMBO-on-demand" approach opens a promising avenue to do electronic-structure simulations and total energy calculations for big systems directly from first principles.

CHAPTER 5. NEW DENSITY FUNCTIONAL THEORY DEVELOPMENT FOR SYSTEMS WITH STRONG ELECTRON CORRELATION

5.1 Introduction

Density functional theory (DFT) with local density approximation (LDA) or generalized gradient approximation (GGA) has been successfully applied to many solid state systems in several decades[Kohn et al., (1964); Perdew et al., (1996); Chelikowsky et al., (1996); Kresse et al., (1996, 1999)]. However, the predictive capability of DFT with LDA/GGA becomes limited or completely fails for systems with significant electronic correlation effects, such as materials containing transition metal or rear-earth element with f-electron. Quite a few methods which try to go beyond LDA/GGA have been proposed and studied intensively in the last two decades. Based on the idea of merger of two seemingly different approaches, traditional DFT-LDA and model Hamiltonian approach, Anisimov et al., (1991) proposed the LDA+U method. It takes into account the onsite Coulomb repulsion in a static mean-field way. LDA+U method turns out to be very useful for materials with strong electron correlation, but fails for materials with intermediate correlation effect. LDA plus Dynamical Mean Field Theory(LDA+DMFT)[Kotliar et al., (2004); Kotloiar et al., (2006); McMahan (2005); Savrasov et al., (2001)] behaves correctly from weakly correlated materials to strongly correlated materials, but the evaluation of frequency-dependent electron self-energy makes the method very demanding in computation time. It should be pointed out that both LDA+U and LDA+DMFT have a parameter U, which is manually added in an ad hoc manner. There are also methods which deal with the parametrized exchange-correlation potential directly, like self-interaction-correction LDA[Petit (2002)] and hybrid-functionals[Martin (2003); Martin

et al., (2005)]. Although these methods may address the problem stemming from electron correlation to some extent, a generally accepted predictive theory for materials with important electron correlation effect is still lacking. Here we propose a new density functional theory which maps a correlated electron system to a solvable electron system with exact onsite Hamiltonian. Additional set of self-consistent equations are obtained for the solution of this many body problem. All the interactions are treated in a self-consistent manner and there are no adjustable parameters in our method.

5.2 Method and formalism

5.2.1 Many electron problem

In a solid state system, the many body Hamiltonian for electrons may be written as

$$H = \sum_i \left(-\frac{\hbar^2}{2m} \nabla_i^2 \right) + \sum_{il} \left(-\frac{e^2}{4\pi\varepsilon_0} \frac{Z_l}{|\mathbf{r}_i - \mathbf{R}_l|} \right) + \frac{1}{2} \sum_{i \neq j} \frac{e^2}{4\pi\varepsilon_0} \frac{1}{|\mathbf{r}_i - \mathbf{r}_j|} \tag{5.1}$$

where Born-Oppenheimer approximation has been adopted to separate the degerees of freedom of fast electrons from slow ions. The first term $\sum_i \left(-\frac{\hbar^2}{2m} \nabla_i^2 \right)$ describes the kinetic energy of electrons. The second term describes electron-ion Coulomb attraction. The third term decsribes electron-electron Coulomb repulsion, which correlates the motions of the electrons. It is because of the existence of the third term that the exact analytic solution of electron-ion system only exists for hydrogen atom. Furthermore, this Hamiltonian may be exactly solved numerically only for very few electrons. The quantum states increase exponentially with the number of electrons, thus any method which tries to exactly solve many electron Hamiltonian is doomed to fail. There are two main streams to solve the many-electron problem approximately. One is quantum chemistry group based on the Hartree-Fock approximation; another is condensed matter physics group based on density functional theory. However, the only method which can be successfully applied to solid is density functional theory.

5.2.2 Density functional theory

It is very difficult to solve the full electronic spectrum of many-electron systems. However, the ground state energy of the many electron system (and its derivatives) can already determine many important physical properties. Thus it is physically desirable to have a method to solve for the ground state of the many-electron system. The Hohenberg-Kohn theorem[Kohn et al., (1964)] states that the ground state energy of a many-electron system is a functional of the electron density.

$$E_0[\rho] = T_0[\rho] + V_H[\rho] + E_{xc}^0[\rho] + \int V_{ion}(\mathbf{r})\,\rho(\mathbf{r})\,d^3r \tag{5.2}$$

where

$$V_H[\rho] = \frac{1}{2}\frac{e^2}{4\pi\varepsilon_0}\iint \frac{\rho(\mathbf{r})\,\rho(\mathbf{r}')}{|\mathbf{r}-\mathbf{r}'|}d^3r d^3r' \tag{5.3}$$

The dimension of the many electron problem is therefore greatly reduced to 3 from $3N_e$ in the quantum chemistry wavefunction approach. Unfortunately, the form of the total energy functional may not be given by the theory, i.e., the functional of kinetic energy and exchange-correlation energy is not known. Based on Virial theorem, the kinetic energy of a stable system is of the same order of the total energy, while the exchange-correlation energy is much smaller. Hence the kinetic energy functional must be carefully devised to high accuracy. Starting from Thomas-Fermi's approximation of the kinetic energy functional based on free electron gas, many efforts have been devoted to improve it, yet without great success. Kohn and Sham[Kohn et al., (1964)] took a different way and made a significant progress in approximating the kinetic energy functional by expressing it as the sum of kinetic energy of fictitious non-interacting electrons which keeps the same density as real system. In terms of formula

$$T_0[\rho] = \sum_i -\frac{\hbar^2}{2m}\left\langle \psi_i \left| \nabla_i^2 \right| \psi_i \right\rangle \tag{5.4}$$

with

$$\rho(\mathbf{r}) = \sum_i |\psi_i(\mathbf{r})|^2 \tag{5.5}$$

The difference between the true total energy, $E_0[\rho]$, and the sum of non-interacting kinetic energy $T_0[\rho]$, the Hartree energy $V_H[\rho]$, the external potential energy $\int V_{ion}(\mathbf{r})\,\rho(\mathbf{r})\,d^3r$ is called

exchange-correlation energy, $E_{xc}^{0}[\rho]$. As a result, Kohn and Sham abandoned the attracting advantage of dimension reduction by introducing the single particle wavefunctions. However, the Kohn-Sham approach with LDA for the exchange-correlation energy is unexpectedly successful. The main reason is that the only approximate term, the exchange-correlation energy $E_{xc}[\rho]$, in Kohn-Sham approach is very small compared with the total energy; while in the orbital-free DFT, the kinetic energy functional is also an approximation as we discussed. LDA is based on the homogeneous electron gas, which is a fairly good approximation for metals. Thus it is reasonable that LDA-DFT also behaves well for electron density with small spatial variation. For systems with strongly localized charges, e.g., transition metal oxides, rear-earth materials, the results from LDA-DFT may be suspecious, sometimes completely wrong. This casts a great challenge to the computational physics community.

5.2.3 Model Hamiltonian and Gutzwiller approximation

Another different approach to address the physical properties of solid state systems is based on parametrized model Hamiltonian. While quantum chemistry or DFT tries to solve the many-electron problem by including all the relevant degrees of freedom, model Hamiltonian is focused on the most essential interactions governing the low temperature physics, i.e., the quantum states near the Fermi-level. Model Hamiltonian is very successful to explain the complicated problems, like Mott metal-insulator transition, Kondo effect, and superconductivity. Although model Hamiltonian has been greatly simplified, the exact solutions only exist for very few cases in 1-dimention or infinite-dimension limit. Generally, certain approximations need to be employed. Gutzwiller (1963,1965) proposed a Jastrow-type correlated wavefunction of the electrons and an approximation to simplify the counting procedures in the problem of ferromagnetism. Jastrow-type wave function has a general form of

$$|\Psi_J\rangle = \hat{F}\,|\Psi_0\rangle \tag{5.6}$$

where $\hat{F}$ is a correlation operator. $|\Psi_0\rangle$ is a non-interacting wavefunction which corresponds to a single Slater determinant.

We will first apply the Gutzwiller approximation to the widely used Anderson lattice model, and then show that it may be naturally incorporated in the DFT framework.

5.2.3.1 Non-degenerate Anderson lattice

We consider the Anderson lattice with no orbital degeneracy[Dorin et al., (1992)]. We focus on the paramagnetic solution. The Hamiltonian is

$$\begin{aligned} H &= \sum_{\mathbf{k}\sigma} \varepsilon_{\mathbf{k}} c^{\dagger}_{\mathbf{k}\sigma} c_{\mathbf{k}\sigma} + \sum_{\mathbf{k}\sigma} \varepsilon_f f^{\dagger}_{\mathbf{k}\sigma} f_{\mathbf{k}\sigma} \\ &\quad + V \sum_{i\sigma} \left(f^{\dagger}_{i\sigma} c_{i\sigma} + h.c. \right) + U \sum_i n^{(f)}_{i\uparrow} n^{(f)}_{i\downarrow} \end{aligned} \tag{5.7}$$

where the first term accounts for the normal non-interacting conduction electrons. The second term accounts for the localized orbital. The third term accounts for the onsite hybridization between the localized orbital and and the extended orbital with strengh V. The fourth term accounts for the onsite Coulomb repulsion between the localized orbitals. Also for convenience, $\varepsilon_{\mathbf{k}} = \varepsilon^0_{\mathbf{k}} - \mu$ and $\varepsilon_f = \varepsilon^0_f - \mu$. Here $\varepsilon^0_{\mathbf{k}}$ is the conduction band energy, ε^0_f is the localized orbital level energy, and μ is the chemical potential for the whole electron system.

With Gutzwiller approximation, the effective Hamiltonian may be written as

$$\begin{aligned} H_{\text{eff}} &= \sum_{\mathbf{k}\sigma} \varepsilon_{\mathbf{k}} c^{\dagger}_{\mathbf{k}\sigma} c_{\mathbf{k}\sigma} + \sum_{\mathbf{k}\sigma} \left(\varepsilon_f + \mu_{1\sigma} \right) f^{\dagger}_{\mathbf{k}\sigma} f_{\mathbf{k}\sigma} \\ &\quad + V \sum_{i\sigma} \left(z_{i\sigma} f^{\dagger}_{i\sigma} c_{i\sigma} + h.c. \right) \end{aligned} \tag{5.8}$$

where the renormalization factor

$$z_\sigma = \frac{b_{1\sigma} b_0 + b_2 b_{1-\sigma}}{\sqrt{n^f_\sigma \left(1 - n^f_\sigma \right)}} \tag{5.9}$$

with the local orbital occupation

$$n^f_\sigma = \left\langle f^{\dagger}_{\mathbf{i}\sigma} f_{\mathbf{i}\sigma} \right\rangle \tag{5.10}$$

The total energy to be minimized is:

$$\begin{aligned} E/N &= \langle H_{\text{eff}} \rangle / N + \mu_0 \left(1 - \left(b_0^2 + b_{1\uparrow}^2 + b_{1\downarrow}^2 + b_2^2 \right) \right) + U b_2^2 \\ &\quad - \sum_\sigma \mu_{1\sigma} \left(b_{1\sigma}^2 + b_2^2 \right) \end{aligned} \tag{5.11}$$

This gives a set of equations:

$$1 = b_0^2 + b_{1\uparrow}^2 + b_{1\downarrow}^2 + b_2^2 \tag{5.12}$$

$$n_\sigma^f = b_{1\sigma}^2 + b_2^2 \tag{5.13}$$

$$0 = \sum_\sigma \frac{2Vb_{1\sigma}}{\sqrt{n_\sigma^f\left(1-n_\sigma^f\right)}}\left\langle f_{i\sigma}^\dagger c_{i\sigma}\right\rangle - 2\mu_0 b_0 \tag{5.14}$$

$$\begin{aligned} 0 &= \frac{2Vb_0}{\sqrt{n_\sigma^f\left(1-n_\sigma^f\right)}}\left\langle f_{i\sigma}^\dagger c_{i\sigma}\right\rangle + \frac{2Vb_2}{\sqrt{n_{-\sigma}^f\left(1-n_{-\sigma}^f\right)}}\left\langle f_{i-\sigma}^\dagger c_{i-\sigma}\right\rangle & (5.15)\\ &\quad -2\left(\mu_0+\mu_{1\sigma}\right)b_{1\sigma} & (5.16)\end{aligned}$$

$$0 = \sum_\sigma \frac{2b_{1-\sigma}V}{\sqrt{n_\sigma^f\left(1-n_\sigma^f\right)}}\left\langle f_{i\sigma}^\dagger c_{i\sigma}\right\rangle + 2\left(-\mu_0+U-\mu_{1\uparrow}-\mu_{1\downarrow}\right)b_2 \tag{5.17}$$

The solutions of the above set of equations may be formulated as an eigen-value problem as

$$\begin{pmatrix} 0 & V(\uparrow) & V(\downarrow) & 0 \\ V(\uparrow) & -\mu_{1\uparrow} & 0 & V(\downarrow) \\ V(\downarrow) & 0 & -\mu_{1\downarrow} & V(\uparrow) \\ 0 & V(\downarrow) & V(\uparrow) & U-\mu_{1\uparrow}-\mu_{1\downarrow} \end{pmatrix}\begin{pmatrix} b_0 \\ b_{1\uparrow} \\ b_{1\downarrow} \\ b_2 \end{pmatrix} = \mu_0 \begin{pmatrix} b_0 \\ b_{1\uparrow} \\ b_{1\downarrow} \\ b_2 \end{pmatrix} \tag{5.18}$$

with conditions of

$$b_{1\sigma}^2 + b_2^2 = n_\sigma^f \tag{5.19}$$

where $V(\sigma) = \frac{V}{\sqrt{n_\sigma^f\left(1-n_\sigma^f\right)}}\left\langle f_{i\sigma}^\dagger c_{i\sigma}\right\rangle$. This is in fact a standard problem which may be solved iteratively by, for instance, Broyden mixing method and its variants.

In order to find the expectation values of the operators in the Hamiltonian, we need to analyze the propagators w.r.t. the mean field Hamiltonian H_{eff}, which is expressed as

$$\begin{aligned} H_{\text{eff}} &= \sum_{\mathbf{k}\sigma}\varepsilon_{\mathbf{k}}c_{\mathbf{k}\sigma}^\dagger c_{\mathbf{k}\sigma} + \sum_{\mathbf{k}\sigma}\tilde{\varepsilon}_f f_{\mathbf{k}\sigma}^\dagger f_{\mathbf{k}\sigma} \\ &\quad + zV\sum_{i\sigma}\left(f_{\mathbf{k}\sigma}^\dagger c_{\mathbf{k}\sigma} + h.c.\right) \end{aligned} \tag{5.20}$$

where $\tilde{\varepsilon}_f = \varepsilon_f + \mu_{1\sigma}$. In momentum space, the equation of motion for the local-electron propagator is

$$(\omega - \tilde{\varepsilon}_f) \left\langle\left\langle f_{\mathbf{k}\sigma}; f^\dagger_{\mathbf{k}\sigma} \right\rangle\right\rangle_\omega = 1 + zV \left\langle\left\langle c_{\mathbf{k}\sigma}; f^\dagger_{\sigma} \right\rangle\right\rangle_\omega \tag{5.21}$$

$$(\omega - \varepsilon_{\mathbf{k}}) \left\langle\left\langle c_{\mathbf{k}\sigma}; f^\dagger_{\mathbf{k}\sigma} \right\rangle\right\rangle_\omega = zV \left\langle\left\langle f_{\mathbf{k}\sigma}; f^\dagger_{\mathbf{k}\sigma} \right\rangle\right\rangle_\omega \tag{5.22}$$

$$(\omega - \varepsilon_{\mathbf{k}}) \left\langle\left\langle c_{\mathbf{k}\sigma}; c^\dagger_{\mathbf{k}\sigma} \right\rangle\right\rangle_\omega = 1 + zV \left\langle\left\langle f_{\mathbf{k}\sigma}; c^\dagger_{\mathbf{k}\sigma} \right\rangle\right\rangle_\omega \tag{5.23}$$

$$(\omega - \tilde{\varepsilon}_f) \left\langle\left\langle f_{\mathbf{k}\sigma}; c^\dagger_{\mathbf{k}\sigma} \right\rangle\right\rangle_\omega = zV \left\langle\left\langle c_{\mathbf{k}\sigma}; c^\dagger_{\mathbf{k}\sigma} \right\rangle\right\rangle_\omega \tag{5.24}$$

The above set of equations give

$$\left\langle\left\langle f_{\mathbf{k}\sigma}; f^\dagger_{\mathbf{k}\sigma} \right\rangle\right\rangle_\omega = \frac{1}{\omega - \tilde{\varepsilon}_f - \frac{(zV)^2}{\omega - \varepsilon_{\mathbf{k}}}} \tag{5.25}$$

$$\left\langle\left\langle c_{\mathbf{k}\sigma}; c^\dagger_{\mathbf{k}\sigma} \right\rangle\right\rangle_\omega = \frac{1}{\omega - \varepsilon_{\mathbf{k}} - \frac{(zV)^2}{\omega - \tilde{\varepsilon}_f}} \tag{5.26}$$

and

$$\begin{aligned} \left\langle\left\langle c_{\mathbf{k}\sigma}; f^\dagger_{\mathbf{k}\sigma} \right\rangle\right\rangle_\omega &= \frac{zV}{\omega - \varepsilon_{\mathbf{k}}} \left\langle\left\langle f_{\mathbf{k}\sigma}; f^\dagger_{\mathbf{k}\sigma} \right\rangle\right\rangle_\omega \\ &= \frac{zV}{(\omega - \varepsilon_{\mathbf{k}})(\omega - \tilde{\varepsilon}_f) - (zV)^2} \\ &= \frac{1}{\omega - \tilde{\varepsilon}_f} \frac{zV}{\omega - \varepsilon_{\mathbf{k}} - \frac{(zV)^2}{\omega - \tilde{\varepsilon}_f}} \end{aligned} \tag{5.27}$$

The single particle Green functions may be also written as

$$G^{ff}_\sigma(\mathbf{k},\omega) = \left\langle\left\langle f_{\mathbf{k}\sigma}; f^\dagger_{\mathbf{k}\sigma} \right\rangle\right\rangle_\omega = \frac{u^2_{\mathbf{k}}}{\omega - E_+(\mathbf{k})} + \frac{v^2_{\mathbf{k}}}{\omega - E_-(\mathbf{k})} \tag{5.28}$$

$$G^{cc}_\sigma(\mathbf{k},\omega) = \left\langle\left\langle c_{\mathbf{k}\sigma}; c^\dagger_{\mathbf{k}\sigma} \right\rangle\right\rangle_\omega = \frac{v^2_{\mathbf{k}}}{\omega - E_+(\mathbf{k})} + \frac{u^2_{\mathbf{k}}}{\omega - E_-(\mathbf{k})} \tag{5.29}$$

where

$$E_\pm(\mathbf{k}) = \frac{1}{2}\left(\varepsilon_{\mathbf{k}} + \tilde{\varepsilon}_f \pm \sqrt{(\varepsilon_{\mathbf{k}} - \tilde{\varepsilon}_f)^2 + 4(zV)^2}\right) \tag{5.30}$$

and

$$\begin{aligned} 2u^2_{\mathbf{k}} &= 1 - \frac{\varepsilon_{\mathbf{k}} - \varepsilon_f}{\sqrt{(\varepsilon_{\mathbf{k}} - \varepsilon_f)^2 + 4(zV)^2}} \\ 2v^2_{\mathbf{k}} &= 1 + \frac{\varepsilon_{\mathbf{k}} - \varepsilon_f}{\sqrt{(\varepsilon_{\mathbf{k}} - \varepsilon_f)^2 + 4(zV)^2}}. \end{aligned} \tag{5.31}$$

We also have

$$\begin{aligned} G_{\sigma}^{cf}\left(\mathbf{k},\omega\right) &= \left\langle\left\langle c_{\mathbf{k}\sigma};f_{\mathbf{k}\sigma}^{\dagger}\right\rangle\right\rangle_{\omega}=\frac{zV}{\omega-\varepsilon_{\mathbf{k}}}\left\langle\left\langle f_{\mathbf{k}\sigma};f_{\mathbf{k}\sigma}^{\dagger}\right\rangle\right\rangle_{\omega} \\ &= \frac{zV}{\omega-\tilde{\varepsilon}_{f}}\left\langle\left\langle c_{\mathbf{k}\sigma};c_{\mathbf{k}\sigma}^{\dagger}\right\rangle\right\rangle_{\omega} \end{aligned} \tag{5.32}$$

From the last equation follows

$$\begin{aligned} -\frac{1}{\pi}ImG^{fc}\left(\mathbf{k},\omega+i0^{+}\right) &= b\delta\left(\omega-\varepsilon_{f}\right)ReG^{cc}\left(\mathbf{k},\varepsilon_{f}+i0^{+}\right) \\ &\quad +\mathcal{P}\left(\frac{b}{\omega-\varepsilon_{f}}\right)\rho^{cc}\left(\mathbf{k},\omega\right) \end{aligned} \tag{5.33}$$

where $\rho^{cc}\left(\mathbf{k},\omega\right)=-\frac{1}{\pi}ImG^{cc}\left(\mathbf{k},\omega+i0^{+}\right)$. And we use

$$\lim_{\eta\to0}\int_{a}^{b}dx\frac{f\left(x\right)}{x-x_{0}\pm i\eta}=\mathcal{P}\int_{a}^{b}dx\frac{f\left(x\right)}{x-x_{0}}\mp i\pi f\left(x_{0}\right)$$

where

$$\mathcal{P}\int_{a}^{b}dx\frac{f\left(x\right)}{x-x_{0}}=\lim_{\delta\to0}\left(\int_{a}^{x_{0}-\delta}dx\frac{f\left(x\right)}{x-x_{0}}+\int_{x_{0}+\delta}^{b}dx\frac{f\left(x\right)}{x-x_{0}}\right)$$

thus

$$\begin{aligned} \frac{1}{x-x_{0}\pm i\eta} &= \mathcal{P}\frac{1}{x-x_{0}}\mp i\pi\delta\left(x-x_{0}\right) \\ G_{m}^{cc}\left(\mathbf{k},\omega\right) &= \frac{1}{\omega-\varepsilon_{\mathbf{k}}-\frac{b^{2}}{\omega-\varepsilon_{f}}} \end{aligned} \tag{5.34}$$

The first term in Eqn.5.33 vanishes for $zV\neq0$ because

$$\begin{aligned} \lim_{\gamma\to0^{+}}G^{cc}\left(\mathbf{k},\lambda+i\gamma\right) &= \lim_{\gamma\to0^{+}}\frac{1}{\lambda-\varepsilon_{\mathbf{k}}+i\gamma-\frac{b^{2}}{i\gamma}} \\ &= \lim_{\gamma\to0^{+}}\frac{1}{\lambda-\varepsilon_{\mathbf{k}}\ +i\frac{b^{2}}{\gamma}} \\ &= \lim_{\gamma\to0^{+}}\frac{\gamma^{2}\left(\lambda-\varepsilon_{\mathbf{k}}\right)\ +i\gamma b^{2}}{b^{4}}=0 \end{aligned} \tag{5.35}$$

Thus

$$-\frac{1}{\pi}ImG^{fc}\left(\mathbf{k},\omega+i0^{+}\right)=\mathcal{P}\left(\frac{b}{\omega-\varepsilon_{f}}\right)\rho^{cc}\left(\mathbf{k},\omega\right) \tag{5.36}$$

The conduction electron density of states can be expressed in terms of the bare density of states $\rho_{0}\left(\omega\right)=\sum_{\mathbf{k}}\delta\left(\omega-\varepsilon_{\mathbf{k}}^{0}\right)$ via:

$$\rho^{cc}\left(\omega\right)=\sum_{\mathbf{k}}\rho_{m}^{cc}\left(\mathbf{k},\omega\right)=\rho_{0}\left(\Omega\left(\omega\right)\right) \tag{5.37}$$

with:

$$\Omega(\omega) = \omega + \mu - \frac{(zV)^2}{\omega + \mu - \left(\varepsilon_f^0 + \mu_1\right)} \tag{5.38}$$

Similarly, it follows:

$$\begin{aligned} \rho^{fc}(\omega) &= -\frac{1}{\pi}\sum_{\mathbf{k}} ImG^{fc}\left(\mathbf{k},\omega + i0^+\right) \\ &= \mathcal{P}\left(\frac{zV}{\omega - \tilde{\varepsilon}_f}\right)\rho_0(\Omega(\omega)) \\ &= \mathcal{P}\left(\frac{zV}{\omega + \mu - \left(\varepsilon_f^0 + \mu_1\right)}\right)\rho_0(\Omega(\omega)) \end{aligned} \tag{5.39}$$

To determine the density of states for the localized orbital, we use that $\rho^{ff}(\omega) = \rho^{tot}(\omega) - \rho^{cc}(\omega)$ where

$$\begin{aligned} \rho^{tot}(\omega) &= \sum_{\mathbf{k}} \left(\delta(\omega - E_+(\mathbf{k})) + \delta(\omega - E_+(\mathbf{k}))\right) \\ &= \left(1 + \frac{(zV)^2}{\left(\omega + \mu - \left(\varepsilon_f^0 + \mu_1\right)\right)^2}\right)\rho_0(\Omega(\omega)) \end{aligned} \tag{5.40}$$

Here we used the general formula for Dirac Delta function

$$\delta(g(x)) = \sum_i \frac{\delta(x - x_i)}{|g'(x_i)|} \tag{5.41}$$

x_i is the i^{th} solution of $g(x) = 0$.

Thus it holds

$$\rho^{ff}(\omega) = \frac{b^2}{(\omega - \tilde{\varepsilon}_f)^2}\rho_0(\Omega(\omega)). \tag{5.42}$$

At $T = 0$, we have

$$\begin{aligned} \left\langle f_{i\sigma}^\dagger c_{i\sigma}\right\rangle &= \int_{-\infty}^0 \rho^{fc}(\omega)\, d\omega \\ n^f &= \int_{-\infty}^0 \rho^{ff}(\omega)\, d\omega \\ n^{tot} &= \int_{-\infty}^0 \rho^{tot}(\omega)\, d\omega \end{aligned} \tag{5.43}$$

In practice, the total number of electrons, n^{tot}, the local orbital level energy, ε_f^0, and the bare density of states of the conduction electrons should be given, then Eqn.5.18, 5.19, 5.43 are solved iteratively.

5.2.4 Gutzwiller density functional theory

In this part we give the detailed formalisms to show that the above Gutzwiller approximation may be naturally incooperated in the DFT framework.

5.2.4.1 Choice of reference system

Instead of choosing the non-interacting electron reference system in the Kohn-Sham approach, we choose our simplified interacting electron reference system to be represented by the following Hamiltonian

$$\hat{H}_s = \hat{T} + \hat{V}_s + \hat{U}_s \tag{5.44}$$

where

$$\hat{T} = \sum_{i,j,\alpha,\beta,\sigma} \left\langle \phi_{i\alpha\sigma} \left| \hat{T} \right| \phi_{j\beta\sigma} \right\rangle c^{\dagger}_{i\alpha\sigma} c_{j\beta\sigma} \tag{5.45}$$

$$\hat{V}_s = \sum_{i,j,\alpha,\beta,\sigma} \left\langle \phi_{i\alpha\sigma} \left| \hat{V}_s \right| \phi_{j\beta\sigma} \right\rangle c^{\dagger}_{i\alpha\sigma} c_{j\beta\sigma} \tag{5.46}$$

$$\hat{U}_s = \frac{1}{2} \sum_{(\alpha,\beta,\gamma,\delta)\in\mathcal{L},\sigma,\sigma'} U_{\alpha\sigma\beta\sigma';\gamma\sigma\delta\sigma'} c^{\dagger}_{i\alpha\sigma} c^{\dagger}_{i\beta\sigma'} c_{i\delta\sigma'} c_{i\gamma\sigma} \tag{5.47}$$

with

$$U_{\alpha\sigma\beta\sigma';\gamma\sigma\delta\sigma'} = \frac{e^2}{4\pi\varepsilon_0} \int d\mathbf{r} \int d\mathbf{r}' \phi_{i\alpha}(\mathbf{r}) \phi_{i\beta}(\mathbf{r}') \frac{1}{|\mathbf{r}-\mathbf{r}'|} \phi_{i\gamma}(\mathbf{r}) \phi_{i\delta}(\mathbf{r}') \tag{5.48}$$

$\{\phi_{i\alpha}\}$ is a complete set of orbitals for the system, a subset $\mathcal{L}$ of which represents non-overlapping localized orbitals at the various sites in the system. Thus $\hat{U}_s$ is the projection of the two-particle Coulomb repulsion operator onto the localized orbital subspace, including only on-site terms. The remaining part of the two-body Coulomb repulsion term is assumed to be represented in a mean-field fashion in $\hat{V}_s$.

5.2.4.2 Exact treatment for on-site Hamiltonian

We will treat exactly the on-site correlations between our localized orbitals by projecting $\hat{H}_s$ onto the localized orbitals at the i^{th} site to give

$$\hat{H}_i = \sum_{(\alpha,\beta)\in\mathcal{L},\sigma} \langle\phi_{i\alpha\sigma}| \left(\hat{T}+\hat{V}_s\right) |\phi_{i\beta\sigma}\rangle\, c^{\dagger}_{i\alpha\sigma}c_{i\beta\sigma} \tag{5.49}$$

$$+\frac{1}{2}\sum_{(\alpha,\beta,\gamma,\delta)\in\mathcal{L},\sigma,\sigma'} U_{\alpha\sigma\beta\sigma';\gamma\sigma\delta\sigma'}c^{\dagger}_{i\alpha\sigma}c^{\dagger}_{i\beta\sigma'}c_{i\delta\sigma'}c_{i\gamma\sigma} \tag{5.50}$$

We can exactly diagonalize the on-site Hamiltonian (including all relevant on-site interactions, like spin-orbit interaction, crystal field effect, magnetic exchange, Hund's rule coupling etc.) to obtain all possible electronic configurations at the site i.

We can introduce the boson operator $b_{i\Gamma}$ to create the configuration $|\Gamma_i\rangle$ at site i. $\hat{H}_s$ may be reformulated as

$$\hat{H}_s = \hat{T}+\hat{V}_s - \sum_{i,(\alpha,\beta)\in\mathcal{L},\sigma} \left\langle \phi_{i\alpha\sigma}\left|\hat{T}+\hat{V}_s\right|\phi_{i\beta\sigma}\right\rangle c^{\dagger}_{i\alpha\sigma}c_{i\beta\sigma} + \sum_{i,\Gamma} E_{i\Gamma}b^{\dagger}_{i\Gamma}b_{i\Gamma} \tag{5.51}$$

Having treated the on-site localized-localized electron correlations in an exact manner, we turn our attention to the effects these correlations have on the electron hopping between different sites in the system.

5.2.4.3 Gutzwiller treatment of intersite hopping

Following Bünemann et al., (1998,2007), we introduce a unitary transformation among the localized orbital basis at each site such that the local density matrix is diagonal. The rotated set of local orbitals, $\{h_{i\gamma\sigma}\}$, are called local natural orbitals.

$$h^{\dagger}_{i\gamma\sigma} = \sum_{\alpha\in\mathcal{L}} u^{*}_{i,\gamma\alpha}\phi^{\dagger}_{i\alpha\sigma} \tag{5.52}$$

$$\left\langle \Psi_0\left|h^{\dagger}_{i\gamma\sigma}h_{i\gamma'\sigma}\right|\Psi_0\right\rangle = n^{0}_{i\gamma\sigma}\delta_{\gamma\gamma'} \tag{5.53}$$

In the local natural basis, we have

$$\hat{H}_s = \hat{T}+\hat{V}_s - \sum_{i,\alpha,\beta,\sigma} \left\langle h_{i\alpha\sigma}\left|\hat{T}+\hat{V}_s\right|h_{i\beta\sigma}\right\rangle h^{\dagger}_{i\alpha\sigma}h_{i\beta\sigma} + \sum_{i,\Gamma} E_{i\Gamma}b^{\dagger}_{i,\Gamma}b_{i,\Gamma} \tag{5.54}$$

Let $\{H\}$ of be a complete Fock states generated by $\left\{h^{\dagger}_{i\alpha\sigma}\right\}$

$$|H\rangle = h^{\dagger}_{i\alpha_1\sigma_1} h^{\dagger}_{i\alpha_2\sigma_2} \cdots |\text{Vacuum}\rangle$$

Local configuration $|\Gamma\rangle$ may be expressed in terms of these Fock states

$$|\Gamma\rangle = \sum_H \langle H|\Gamma\rangle \, |H\rangle$$

We realise that the choice of the Gutzwiller operator is by no means unique. Here we introduce a simplest form, and we may need to examine the some other forms in the future. Gutzwiller operators for site i is chosen to be the projection over Fock states

$$\hat{G}_i = \sum_H g_{iH} \, |H_i\rangle \, \langle H_i| \tag{5.55}$$

and

$$\hat{G} = \prod_i \hat{G}_i \tag{5.56}$$

For any uncorrelated wavefunction $|\Psi_0\rangle = \prod_{n\mathbf{k}\sigma} \psi^{\dagger}_{n\mathbf{k}\sigma} |\text{Vacuum}\rangle$, we can construct a Gutzwiller trial wavefunction

$$|\Psi_G\rangle = \frac{\hat{G}\,|\Psi_0\rangle}{\sqrt{\left\langle \Psi_0 \left| \hat{G}^2 \right| \Psi_0 \right\rangle}} \tag{5.57}$$

To evaluate expectation values in this trial subspace, we follow the results of Bünemann et al., (1998,2007) which are exact in the limit of infinite dimensions. And we have

$$\left\langle \Psi_G \left| \sum_{i,\Gamma} E_i\left(\Gamma\right) b^{\dagger}_{i\Gamma} b_{i\Gamma} \right| \Psi_G \right\rangle = \sum_{i,\Gamma} p_{i,\Gamma} E_{i\Gamma} \tag{5.58}$$

$$p_{i,\Gamma} = \sum_H g^2_{iH} \, |\langle\Gamma|H\rangle|^2 \, m^0_{iH} = \sum_H p_{iH} \, |\langle\Gamma|H\rangle|^2 \tag{5.59}$$

with

$$m^0_{iH} = \prod_{\gamma\sigma(occ)} n^0_{i\gamma\sigma} \prod_{\gamma'\sigma'(unocc)} \left(1 - n^0_{i\gamma'\sigma'}\right) \tag{5.60}$$

For intersite hopping

$$\left\langle \Psi_G \left| h^{\dagger}_{i\alpha\sigma} h_{j\beta\sigma} \right| \Psi_G \right\rangle = z_{i\alpha\sigma} z_{j\beta\sigma} \left\langle \Psi_0 \left| h^{\dagger}_{i\alpha\sigma} h_{j\beta\sigma} \right| \Psi_0 \right\rangle \tag{5.61}$$

$$z_{i\alpha\sigma} = \frac{1}{\sqrt{n^0_{i\alpha\sigma}\left(1-n^0_{i\alpha\sigma}\right)}} \sum_{H,H'} \sqrt{p_{iH}p_{iH'}} \left| \left\langle H \left| h^\dagger_{i\alpha\sigma} \right| H' \right\rangle \right|^2 \tag{5.62}$$

We need to comment on the effect of the choice of Gutzwiller operator here. We observe that Eqn. 5.58 may be rewritten as

$$\left\langle \Psi_G \left| \sum_{i,\Gamma} E_i\left(\Gamma\right) b^\dagger_{i\Gamma} b_{i\Gamma} \right| \Psi_G \right\rangle = \sum_{i,H} p_{iH} E_{iH} \tag{5.63}$$

As a result, this particular choice of Gutzwiller operator removes all the inter-Fock state correlation effect. We believe it would have big effect if we have many local electrons. However, in some systems of interest, e.g., Ce, where local electrons are supposed to be around one, we assume such inter-Fock state correlation effect to be small.

5.2.4.4 Definition of density functional for ground state energy

We can now define our density functional for the ground state energy of our many-electron system

$$E_0\left[\rho\right] = T\left[\rho\right] + \int \rho V_{ion} + \frac{1}{2}\iint \rho v \rho + E_{xc}\left[\rho\right] + E_{ion-ion} \tag{5.64}$$

In this functional, the kinetic energy functional and the exchange-correlation energy functional are defined with respect to the reference interacting electron system system defined above. We define our exchange-correlation functional as

$$E_{xc}\left[\rho\right] = \left\langle \Psi_G \left| \hat{U}_s \right| \Psi_G \right\rangle - \frac{1}{2}\iint \rho_l v \rho_l + \int \rho \varepsilon_{xc}\left(\rho\right) - \int \rho_l \varepsilon_{xc}\left(\rho_l\right) \tag{5.65}$$

The kinetic energy functional is

$$T\left[\rho\right] = \left\langle \Psi_G \left| \hat{H}_s - \hat{V}_s - \hat{U}_s \right| \Psi_G \right\rangle \tag{5.66}$$

Then

$$\begin{aligned} T\left[\rho\right] + E_{xc}\left[\rho\right] &= \left\langle \Psi_G \left| \hat{H}_s \right| \Psi_G \right\rangle - \int \rho V_s - \frac{1}{2}\iint \rho_l v \rho_l & (5.67)\\ &\quad + \int \rho \varepsilon_{xc}\left(\rho\right) - \int \rho_l \varepsilon_{xc}\left(\rho_l\right) & (5.68) \end{aligned}$$

$$\begin{aligned} E_0\left[\rho\right] &= \left\langle \Psi_G \left| \hat{H}_s \right| \Psi_G \right\rangle - \int \rho V_{scr} + \frac{1}{2}\iint \rho v \rho - \frac{1}{2}\iint \rho_l v \rho_l & (5.69)\\ &\quad + \int \rho \varepsilon_{xc}\left(\rho\right) - \int \rho_l \varepsilon_{xc}\left(\rho_l\right) + E_{ion-ion} & (5.70) \end{aligned}$$

where

$$V_{scr} = V_s - V_{ion} \tag{5.71}$$

$\hat{H}_s$ is chosen to have the same electron density as the exact many body ground state. Thus

$$\rho(\mathbf{r}) = \sum_{i\alpha j\beta\sigma} \phi^*_{i\alpha}(\mathbf{r})\,\phi_{j\beta}(\mathbf{r}) \left\langle \Psi_G \left| c^\dagger_{i\alpha\sigma} c_{j\beta\sigma} \right| \Psi_G \right\rangle \tag{5.72}$$

and the local charge density is defined as

$$\rho_l(\mathbf{r}) = \sum_{i\alpha\beta\sigma} h^*_{i\alpha}(\mathbf{r})\,h_{i\beta}(\mathbf{r}) \left\langle \Psi_G \left| h^\dagger_{i\alpha\sigma} h_{i\beta\sigma} \right| \Psi_G \right\rangle \tag{5.73}$$

It is computationally convenient to introduce the local projectors

$$\hat{P}_h = \sum_{i,\alpha,\sigma} |h_{i\alpha\sigma}\rangle \langle h_{i\alpha\sigma}| \tag{5.74}$$

$$\hat{Q}_h = \sum_{i,\alpha,\sigma} z_{i\alpha\sigma} |h_{i\alpha\sigma}\rangle \langle h_{i\alpha\sigma}| \tag{5.75}$$

Then

$$\begin{aligned}\rho(\mathbf{r}) = &\sum_{n\mathbf{k}\sigma} f_{n\mathbf{k}\sigma} \langle\psi_{n\mathbf{k}\sigma}| \left(\left(1-\hat{P}_h\right)+\hat{Q}_h\right)|\mathbf{r}\rangle\langle\mathbf{r}| \left(\left(1-\hat{P}_h\right)+\hat{Q}_h\right)|\psi_{n\mathbf{k}\sigma}\rangle \\ &+ \sum_{i\alpha\sigma} \left(1-z^2_{i\alpha\sigma}\right)\rho_{i\alpha\sigma}(\mathbf{r}) \left(\sum_{n\mathbf{k}} f_{n\mathbf{k}\sigma} \langle\psi_{n\mathbf{k}\sigma}|h_{i\alpha\sigma}\rangle\langle h_{i\alpha\sigma}|\psi_{n\mathbf{k}\sigma}\rangle\right)\end{aligned} \tag{5.76}$$

$$\begin{aligned}\rho_l(\mathbf{r}) = &\sum_{n\mathbf{k}\sigma} f_{n\mathbf{k}\sigma} \langle\psi_{n\mathbf{k}\sigma}| \hat{Q}_h |\mathbf{r}\rangle\langle\mathbf{r}| \hat{Q}_h |\psi_{n\mathbf{k}\sigma}\rangle \\ &+ \sum_{i\alpha\sigma} \left(1-z^2_{i\alpha\sigma}\right)\rho_{i\alpha\sigma}(\mathbf{r}) \left(\sum_{n\mathbf{k}} f_{n\mathbf{k}\sigma} \langle\psi_{n\mathbf{k}\sigma}|h_{i\alpha\sigma}\rangle\langle h_{i\alpha\sigma}|\psi_{n\mathbf{k}\sigma}\rangle\right)\end{aligned} \tag{5.77}$$

where

$$\rho_{i\alpha\sigma}(\mathbf{r}) = \langle h_{i\alpha\sigma}|\mathbf{r}\rangle\langle\mathbf{r}|h_{i\alpha\sigma}\rangle \tag{5.78}$$

5.2.4.5 Variational parameters and self-consistent equations

In addition to the non-interacting Hartree wavefunction $|\Psi_0\rangle$(equivalently $\{\psi_{n\mathbf{k}\sigma}\}$), we have a set of local Fock state occupation probability $\{p_{iH}\}$ as the variational parameters. Furthermore, we have the following constraints

$$n^0_{i\alpha\sigma} - \sum_{\alpha\sigma\in H} p_{iH} = 0 \tag{5.79}$$

$$1-\sum_{H} p_{iH}=0 \tag{5.80}$$

Consider the Lagrange function to be minimized

$$L=E_0\left[\rho\right]+\mu_0\left(1-\sum_{H} p_{iH}\right)+\sum_{i\alpha\sigma}\mu_{\alpha\sigma}\left(n^0_{i\alpha\sigma}-\sum_{H:\alpha\sigma(occ)} p_{iH}\right) \tag{5.81}$$

$$\begin{aligned}
\delta L &= \delta\left\langle\Psi_G\left|\hat{H}_s\right|\Psi_G\right\rangle \\
&\quad +\delta\left\{-\int\rho V_{scr}+\frac{1}{2}\iint\rho v\rho-\frac{1}{2}\iint\rho_l v\rho_l\right. \\
&\quad \left.+\int\rho\varepsilon_{xc}\left(\rho\right)-\int\rho_l\varepsilon_{xc}\left(\rho_l\right)+E_{ion-ion}\right\} \\
&\quad +\delta\left\{\mu_{i0}\left(1-\sum_{H} p_{iH}\right)\right\} \\
&\quad +\delta\left\{\sum_{i\alpha\sigma}\mu_{i\alpha\sigma}\left(n^0_{i\alpha\sigma}-\sum_{H:\alpha\sigma(occ)} p_{iH}\right)\right\}
\end{aligned} \tag{5.82}$$

Note that

$$\left\langle\Psi_G\left|\hat{H}_s\right|\Psi_G\right\rangle=\sum_{i,H} p_{i,H}E_{iH}$$

$$+\sum_{n,\mathbf{k},\sigma} f_{n\mathbf{k}\sigma}\left\langle\psi_{n\mathbf{k}\sigma}\right|\left(1-P_h\right)\left(T+V_s\right)\left(1-P_h\right)\left|\psi_{n\mathbf{k}\sigma}\right\rangle \tag{5.83}$$

$$+\sum_{n,\mathbf{k},\sigma} f_{n\mathbf{k}\sigma}\left(\left\langle\psi_{n\mathbf{k}\sigma}\right|\left(1-P_h\right)\left(T+V_s\right)Q_h\left|\psi_{n\mathbf{k}\sigma}\right\rangle+c.c.\right) \tag{5.84}$$

then we have for the 1^{st} term

$$\delta\left\langle\Psi_G\left|\hat{H}_s\right|\Psi_G\right\rangle$$

$$=\sum_{i,H}\delta p_{i,H}E_{iH} \tag{5.85}$$

$$+\sum_{n,\mathbf{k},\sigma} f_{n\mathbf{k}\sigma}\delta\left\langle\psi_{n\mathbf{k}\sigma}\right|\left(1-\hat{P}_h\right)\left(T+V_s\right)\left(1-\hat{P}_h\right)\left|\psi_{n\mathbf{k}\sigma}\right\rangle \tag{5.86}$$

$$+\sum_{n,\mathbf{k},\sigma} f_{n\mathbf{k}\sigma}\left(\delta\left\langle\psi_{n\mathbf{k}\sigma}\right|\left(1-\hat{P}_h\right)\left(T+V_s\right)\hat{Q}_h\left|\psi_{n\mathbf{k}\sigma}\right\rangle+c.c.\right)$$

$$+\sum_{n,\mathbf{k},\sigma} f_{n\mathbf{k}\sigma}\left(\left\langle\psi_{n\mathbf{k}\sigma}\right|\left(1-\hat{P}_h\right)\left(T+V_s\right)\left(\sum_{i\alpha}\delta z_{i\alpha\sigma}\left|h_{i\alpha\sigma}\right\rangle\left\langle h_{i\alpha\sigma}\right|\right)\left|\psi_{n\mathbf{k}\sigma}\right\rangle+c.c.\right) \tag{5.87}$$

2^{nd} term

$$\delta\left\{-\int\rho V_{scr}+\frac{1}{2}\iint\rho v\rho-\frac{1}{2}\iint\rho_l v\rho_l+\int\rho\varepsilon_{xc}\left(\rho\right)-\int\rho_l\varepsilon_{xc}\left(\rho_l\right)+E_{ion-ion}\right\}$$
$$=\int\left\{\delta\rho\left[-V_{scr}+V_H+\mu_{xc}\right]-\delta\rho_l\left[V_H^l+\mu_{xc}^l\right]\right\} \tag{5.88}$$

$$V_H=\int\rho\left(\mathbf{r}'\right)v\left(\mathbf{r},\mathbf{r}'\right)d^3\mathbf{r}' \tag{5.89}$$

$$V_H^l=\int\rho_l\left(\mathbf{r}'\right)v\left(\mathbf{r},\mathbf{r}'\right)d^3\mathbf{r}' \tag{5.90}$$

$$\mu_{xc}=\frac{\partial}{\partial\rho}\left[\rho\varepsilon_{xc}\left(\rho\right)\right] \tag{5.91}$$

Let's choose

$$V_{scr}=V_H+\mu_{xc}-\hat{P}_h\left(V_H^l+\mu_{xc}^l\right)\hat{P}_h \tag{5.92}$$

then 2^{nd} term vanishes.

3^{rd} term

$$\delta\left\{\mu_{i0}\left(1-\sum_H p_{iH}\right)\right\}=-\mu_{i0}\sum_H\delta p_{iH} \tag{5.93}$$

4^{th} term

$$\delta\left\{\sum_{i\alpha\sigma}\mu_{i\alpha\sigma}\left(n_{i\alpha\sigma}^0-\sum_{H:\alpha\sigma(occ)}p_{iH}\right)\right\}$$
$$=\sum_{i\alpha\sigma}\mu_{i\alpha\sigma}\left(\delta n_{i\alpha\sigma}^0-\sum_{H:\alpha\sigma(occ)}\delta p_{iH}\right) \tag{5.94}$$
$$=\sum_{i\alpha\sigma}\mu_{i\alpha\sigma}\left(\sum_{n,\mathbf{k},\sigma}f_{n\mathbf{k}\sigma}\delta\left\langle\psi_{n\mathbf{k}\sigma}|h_{i\alpha\sigma}^\dagger h_{i\alpha\sigma}|\psi_{n\mathbf{k}\sigma}\right\rangle-\sum_{H:\alpha\sigma(occ)}\delta p_{iH}\right) \tag{5.95}$$

Derivative w.r.t. $\psi_{n\mathbf{k}\sigma}$ gives

$$\hat{H}_{eff}\psi_{n\mathbf{k}\sigma}=\lambda_{n\mathbf{k}\sigma}\psi_{n\mathbf{k}\sigma} \tag{5.96}$$

$$\hat{H}_{eff}=\left(1-\hat{P}_h\right)\left(T+V_s\right)\left(1-\hat{P}_h\right)+\left(\left(1-\hat{P}_h\right)\left(T+V_s\right)\hat{Q}_h+h.c.\right) \tag{5.97}$$
$$+\sum_{i\alpha}\varepsilon_{i\alpha\sigma}h_{i\alpha\sigma}^\dagger h_{i\alpha\sigma} \tag{5.98}$$

$$\varepsilon_{i\alpha\sigma}=\mu_{i\alpha\sigma}+\frac{\partial z_{i\alpha\sigma}}{\partial n_{i\alpha\sigma}^0}e_{i\alpha\sigma} \tag{5.99}$$

with

$$e_{i\alpha\sigma} = \sum_{n,\mathbf{k}} f_{n\mathbf{k}\sigma} \left(\langle \psi_{n\mathbf{k}\sigma} | \left(1 - \hat{P}_h \right) (T + V_s) \, | h_{i\alpha\sigma} \rangle \, \langle h_{i\alpha\sigma} | \psi_{n\mathbf{k}\sigma} \rangle + c.c. \right) \tag{5.100}$$

Derivative w.r.t. p_{iH} gives

$$\mu_{i0} + \sum_{\alpha\sigma \in H} \mu_{i\alpha\sigma} = E_{iH} + \sum_{\alpha,\sigma} \frac{\partial z_{i\alpha\sigma}}{\partial p_{iH}} e_{i\alpha\sigma} \tag{5.101}$$

Derivative w.r.t. μ gives

$$n^0_{i\alpha\sigma} - \sum_{\alpha\sigma \in H} p_{iH} = 0 \tag{5.102}$$

$$1 - \sum_{H} p_{iH} = 0 \tag{5.103}$$

Using

$$\frac{\partial z_{i\alpha\sigma}}{\partial n^0_{i\alpha\sigma}} = \frac{z_{i\alpha\sigma}}{2} \left(\frac{1}{1 - n^0_{i\alpha\sigma}} - \frac{1}{n^0_{i\alpha\sigma}} \right) \tag{5.104}$$

$$\sqrt{p_{iH}} \frac{\partial z_{i\alpha\sigma}}{\partial p_{iH}} = \frac{1}{2\sqrt{n^0_{i\alpha\sigma} \left(1 - n^0_{i\alpha\sigma} \right)}} \sum_{H'} \sqrt{p_{iH'}} \left(\left| \left\langle H \left| h^\dagger_{i\alpha\sigma} \right| H' \right\rangle \right|^2 + \left| \left\langle H' \left| h^\dagger_{i\alpha\sigma} \right| H \right\rangle \right|^2 \right) \tag{5.105}$$

Eqn. 5.101 may be written as

$$\begin{aligned} 0 \;\; = \;\; & \left(E_{iH} - \mu_{i0} - \sum_{\alpha\sigma \text{ in } H} \mu_{i\alpha\sigma} \right) \sqrt{p_{iH}} \\ & + \sum_{H'} \sqrt{p_{iH'}} \sum_{\alpha,\sigma} \frac{e_{i\alpha\sigma}}{2\sqrt{n^0_{i\alpha\sigma} \left(1 - n^0_{i\alpha\sigma} \right)}} \left(\left| \left\langle H \left| h^\dagger_{i\alpha\sigma} \right| H' \right\rangle \right|^2 + \left| \left\langle H' \left| h^\dagger_{i\alpha\sigma} \right| H \right\rangle \right|^2 \right) \end{aligned} \tag{5.106}$$

Equivalently we have a set of homogeneous linear equations

$$\sum_{H'} M^{(i)}_{H,H'} \sqrt{p_{iH'}} = \mu_{i0} \sqrt{p_{iH}} \tag{5.107}$$

where

$$\begin{aligned} M^{(i)}_{H,H'} \;\; = \;\; & \sum_{\alpha,\sigma} \frac{e_{i\alpha\sigma}}{2\sqrt{n^0_{i\alpha\sigma} \left(1 - n^0_{i\alpha\sigma} \right)}} \left(\left| \left\langle H \left| h^\dagger_{i\alpha\sigma} \right| H' \right\rangle \right|^2 + \left| \left\langle H' \left| h^\dagger_{i\alpha\sigma} \right| H \right\rangle \right|^2 \right) \\ & + \delta_{HH'} \left(E_{iH} - \sum_{\alpha\sigma \in H} \mu_{i\alpha\sigma} \right) \end{aligned} \tag{5.108}$$

Thus it turns our to be an eigen-value problem with constraints of Eqn.5.102.

5.2.4.6 Implementation in VASP

The code for Gutzwiller-DFT consists of two parts. One is analogous to the traditional LDA-DFT, where the Hartree wavefunction is solved iteratively. The other is to solve the onsite Hamiltonian and find the local configuration probabilities, $\{p_{iH}\}$. The two parts are independent in principle. For the first part, we choose the most widely used Vienna Ab-initio Simulation Package (VASP)[Kresse et al., (1996)]. It uses ultrasoft pseudopotential or projected-augmented wave(PAW) method and planewave basis[Vanderbilt (1990); Blöchl (1994); Kresse et al., (1999)]. For the simplicity of coding, we choose our local orbital confined in the augmentation sphere in the PAW method.

In PAW method, the true wavefunction $|\psi_{n\mathbf{k}\sigma}\rangle$ and the pseudowavefunction $\left|\tilde{\psi}_{n\mathbf{k}\sigma}\right\rangle$ are related in the following way

$$|\psi_{n\mathbf{k}\sigma}\rangle = \left(1 + \sum_{\Lambda} |\phi_{\Lambda}\rangle \langle\tilde{p}_{\Lambda}| - \sum_{\Lambda} \left|\tilde{\phi}_{\Lambda}\right\rangle \langle\tilde{p}_{\Lambda}|\right) \left|\tilde{\psi}_{n\mathbf{k}\sigma}\right\rangle \tag{5.109}$$

where Λ is a composite index for atomic site i, angular momentum numbers $L = (l, m)$, and reference energy ϵ_l. The charge density $\rho(\mathbf{r})$ (Eqn. 5.76) may be readily decomposed into three parts(see Kresse et al., (1999) for details).

$$\rho(\mathbf{r}) = \tilde{\rho}(\mathbf{r}) - \tilde{\rho}^1(\mathbf{r}) + \rho^1(\mathbf{r}) \tag{5.110}$$

with

$$\tilde{\rho}(\mathbf{r}) = \sum_{n\mathbf{k}\sigma} f_{n\mathbf{k}\sigma} \left\langle\tilde{\psi}_{n\mathbf{k}\sigma}|\mathbf{r}\right\rangle \left\langle\mathbf{r}|\tilde{\psi}_{n\mathbf{k}\sigma}\right\rangle \tag{5.111}$$

$$\tilde{\rho}^1(\mathbf{r}) = \sum_{\Lambda,\Lambda'} \rho_{\Lambda,\Lambda'} \tilde{\Phi}_{\Lambda,\Lambda'}(\mathbf{r}) \tag{5.112}$$

$$\rho^1(\mathbf{r}) = \sum_{\Lambda,\Lambda'} \rho_{\Lambda,\Lambda'} \Phi_{\Lambda,\Lambda'}(\mathbf{r}) \tag{5.113}$$

$$\tilde{\Phi}_{\Lambda,\Lambda'}(\mathbf{r}) = \left\langle\tilde{\phi}_{\Lambda}|\mathbf{r}\right\rangle \left\langle\mathbf{r}|\tilde{\phi}_{\Lambda'}\right\rangle \tag{5.114}$$

$$\begin{aligned} \Phi_{\Lambda,\Lambda'}(\mathbf{r}) &= \langle\phi_{\Lambda}| \left(\left(1 - \hat{P}_h\right) + \hat{Q}_h\right) |\mathbf{r}\rangle \langle\mathbf{r}| \left(\left(1 - \hat{P}_h\right) + \hat{Q}_h\right) |\phi_{\Lambda'}\rangle \\ &\quad + \sum_{i\alpha\sigma} \left(1 - z^2_{i\alpha\sigma}\right) \rho_{i\alpha\sigma}(\mathbf{r}) \langle\phi_{\Lambda}|h_{i\alpha\sigma}\rangle \langle h_{i\alpha\sigma}|\phi_{\Lambda'}\rangle \end{aligned} \tag{5.115}$$

$$\rho_{\Lambda,\Lambda'} = \sum_{n\mathbf{k}\sigma} f_{n\mathbf{k}\sigma} \left\langle \tilde{\psi}_{n\mathbf{k}\sigma} | \tilde{p}_{\Lambda} \right\rangle \left\langle \tilde{p}_{\Lambda'} | \tilde{\psi}_{n\mathbf{k}\sigma} \right\rangle$$

Local charge density $\rho_l(\mathbf{r})$ may be written as

$$\begin{aligned}
\rho_l(\mathbf{r}) &= \sum_{n\mathbf{k}\sigma} f_{n\mathbf{k}\sigma} \langle \psi_{n\mathbf{k}\sigma} | \hat{Q}_h | \mathbf{r} \rangle \langle \mathbf{r} | \hat{Q}_h | \psi_{n\mathbf{k}\sigma} \rangle \\
&+ \sum_{i\alpha\sigma} \left(1 - z_{i\alpha\sigma}^2\right) \rho_{i\alpha\sigma}(\mathbf{r}) \left(\sum_{n\mathbf{k}} f_{n\mathbf{k}\sigma} \langle \psi_{n\mathbf{k}\sigma} | h_{i\alpha\sigma} \rangle \langle h_{i\alpha\sigma} | \psi_{n\mathbf{k}\sigma} \rangle \right) \\
&= \sum_{\Lambda,\Lambda'} \rho_{\Lambda,\Lambda'} \left(\langle \phi_{\Lambda} | \hat{Q}_h | \mathbf{r} \rangle \langle \mathbf{r} | \hat{Q}_h | \phi_{\Lambda'} \rangle + \sum_{i\alpha\sigma} \left(1 - z_{i\alpha\sigma}^2\right) \rho_{i\alpha\sigma}(\mathbf{r}) \langle \phi_{\Lambda} | h_{i\alpha\sigma} \rangle \langle h_{i\alpha\sigma} | \phi_{\Lambda'} \rangle \right)
\end{aligned} \tag{5.116}$$

Now the expectation values of $\hat{H}_s$ may be written as

$$\left\langle \Psi_G \left| \hat{H}_s \right| \Psi_G \right\rangle = E_p + \tilde{E} + E^1 - \tilde{E}^1 \tag{5.117}$$

where

$$E_p = \sum_{i,\Gamma,H} p_{i,H} \left| \langle \Gamma | H \rangle \right|^2 E_{i\Gamma} \tag{5.118}$$

$$\tilde{E} = \sum_{n,\mathbf{k},\sigma} f_{n\mathbf{k}\sigma} \left\langle \tilde{\psi}_{n\mathbf{k}\sigma} \left| \hat{T} \right| \tilde{\psi}_{n\mathbf{k}\sigma} \right\rangle + \int \tilde{v}_{eff} \left(\tilde{\rho} + \hat{\rho}_s \right) \tag{5.119}$$

$$\tilde{v}_{eff} = V_H \left[\tilde{\rho} + \hat{\rho} + \tilde{\rho}_{Zc} \right] + \mu_{xc} \left[\tilde{\rho} + \hat{\rho} + \tilde{\rho}_c \right] \tag{5.120}$$

$$\begin{aligned}
E^1 \;=\; & \sum_{\Lambda,\Lambda'} \rho_{\Lambda,\Lambda'} \langle \phi_{\Lambda} | \left(\hat{T} + v_{eff}^1 \right) + P_h \left(\hat{T} + v_{eff}^1 \right) P_h \\
& + \left(\left(\hat{T} + v_{eff}^1 \right) (Q_h - P_h) - P_h \left(\hat{T} + v_{eff}^1 \right) Q_h + c.c. \right) | \phi_{\Lambda'} \rangle
\end{aligned} \tag{5.121}$$

$$v_{eff}^1 = V_H \left[\rho^1 + \rho_{Zc} \right] + \mu_{xc} \left[\rho^1 + \rho_c \right] \tag{5.122}$$

$$\tilde{E}^1 = \sum_{\Lambda,\Lambda'} \rho_{\Lambda,\Lambda'} \left\langle \tilde{\phi}_{\Lambda} | \hat{T} | \tilde{\phi}_{\Lambda'} \right\rangle + \overline{\int \tilde{v}_{eff}^1 \left(\tilde{\rho}^1 + \hat{\rho}_s \right)} \tag{5.123}$$

$$\tilde{v}_{eff}^1 = V_H \left[\tilde{\rho}^1 + \hat{\rho} + \tilde{\rho}_{Zc} \right] + \mu_{xc} \left[\tilde{\rho}^1 + \hat{\rho} + \tilde{\rho}_c \right] \tag{5.124}$$

Derivative with respective to $\bar{\rho}$=$\sum_{n\mathbf{k}\sigma} f_{n\mathbf{k}\sigma} \left| \tilde{\psi}_{n\mathbf{k}\sigma} \right\rangle \left\langle \tilde{\psi}_{n\mathbf{k}\sigma} \right|$ gives the effective Hamiltonian for the Hartree wavefunction.

$$\frac{d\tilde{E}}{d\bar{\rho}} = \hat{T} + \tilde{v}_{eff} + \sum_{\Lambda,\Lambda'} |\tilde{p}_{\Lambda}\rangle \hat{D}_{\Lambda\Lambda'} \langle \tilde{p}_{\Lambda}| \tag{5.125}$$

with

$$\hat{D}_{\Lambda\Lambda'} = \hat{D}^{v}_{\Lambda\Lambda'} + \hat{D}^{z}_{\Lambda\Lambda'} \tag{5.126}$$

$$\hat{D}^{v}_{\Lambda\Lambda'} = \sum_{L} \int \tilde{v}_{eff}\left(\mathbf{r}\right) \hat{Q}^{s,L}_{\Lambda\Lambda'}\left(\mathbf{r}\right) \tag{5.127}$$

$$\hat{Q}^{s,L}_{\Lambda\Lambda'}\left(\mathbf{r}\right) = q^{s,L}_{\Lambda\Lambda'} g_l\left(\left|\mathbf{r}-\mathbf{R}\right|\right) Y_L\left(\widehat{\mathbf{r}-\mathbf{R}}\right) \tag{5.128}$$

$$q^{s,L}_{\Lambda\Lambda'} = \int_{\Omega_r} Q^{s}_{\Lambda\Lambda'}\left(\mathbf{r}\right) \left|\mathbf{r}-\mathbf{R}\right|^{l} Y^{*}_{L}\left(\widehat{\mathbf{r}-\mathbf{R}}\right) d\mathbf{r} \tag{5.129}$$

$$Q^{s}_{\Lambda\Lambda'}\left(\mathbf{r}\right) = \Phi^{s}_{\Lambda,\Lambda'}\left(\mathbf{r}\right) - \tilde{\Phi}_{\Lambda,\Lambda'}\left(\mathbf{r}\right) \tag{5.130}$$

$$\begin{aligned} \Phi^{s}_{\Lambda,\Lambda'}\left(\mathbf{r}\right) &= \left\langle \phi_{\Lambda}\right| \left(1-P_h\left|\mathbf{r}\right\rangle \left\langle \mathbf{r}\right| 1-P_h\right) \\ &\quad + \left(1-P_h\left|\mathbf{r}\right\rangle \left\langle \mathbf{r}\right| Q_h + c.c.\right) \left|\phi_{\Lambda'}\right\rangle \end{aligned} \tag{5.131}$$

$$\hat{D}^{z}_{\Lambda\Lambda'} = \sum_{i\alpha\sigma} \frac{\partial z_{i\alpha\sigma}}{\partial n^{0}_{i\alpha\sigma}} \left\langle \phi_{\Lambda}\right| h^{\dagger}_{i\alpha\sigma} h_{i\alpha\sigma} \left|\phi_{\Lambda'}\right\rangle \hat{e}_{i\alpha\sigma} \tag{5.132}$$

$$\begin{aligned} \hat{e}_{i\alpha\sigma} &= \sum_{(\lambda,\lambda'),L} \rho_{\lambda\lambda'} \left(\int \tilde{v}_{eff}\left(\mathbf{r}\right) g_l\left(\left|\mathbf{r}-\mathbf{R}\right|\right) Y_L\left(\widehat{\mathbf{r}-\mathbf{R}}\right) dr \right) \\ &\quad \times \int \left(\left\langle \phi_{\lambda}\right| h_{i\alpha\sigma}\right\rangle \left\langle h_{i\alpha\sigma}\right| \mathbf{r}\right\rangle \left\langle \mathbf{r}\right| \left(1-P_h\right) \left|\phi_{\lambda'}\right\rangle + c.c.\right) \left|\mathbf{r}-\mathbf{R}\right|^{l} Y^{*}_{L}\left(\widehat{\mathbf{r}-\mathbf{R}}\right) d\mathbf{r} \end{aligned} \tag{5.133}$$

and

$$\frac{dE^{1}}{d\bar{\rho}} = \sum_{\Lambda,\Lambda'} \left|\tilde{p}_{\Lambda}\right\rangle D^{1}_{\Lambda\Lambda'} \left\langle \tilde{p}_{\Lambda}\right| \tag{5.134}$$

with

$$D^{1}_{\Lambda\Lambda'} = D^{1,v}_{\Lambda\Lambda'} + D^{1,z}_{\Lambda\Lambda'} \tag{5.135}$$

$$\begin{aligned} D^{1,v}_{\Lambda\Lambda'} &= \left\langle \phi_{\Lambda}\right| \left(\hat{T} + v^{1}_{eff}\right) + P_h \left(\hat{T} + v^{1}_{eff}\right) P_h \\ &\quad + \left(\left(\hat{T} + v^{1}_{eff}\right) \left(Q_h - P_h\right) - P_h \left(\hat{T} + v^{1}_{eff}\right) P_h + c.c. \right) \left|\phi_{\Lambda'}\right\rangle \end{aligned} \tag{5.136}$$

$$D^{1,z}_{\Lambda\Lambda'} = \sum_{i\alpha\sigma} \frac{\partial z_{i\alpha\sigma}}{\partial n^{0}_{i\alpha\sigma}} \left\langle \phi_{\Lambda}\right| h^{\dagger}_{i\alpha\sigma} h_{i\alpha\sigma} \left|\phi_{\Lambda'}\right\rangle e^{1}_{i\alpha\sigma} \tag{5.137}$$

$$e^{1}_{i\alpha\sigma} = \sum_{(\lambda,\lambda'),L} \rho_{\lambda\lambda'} \left\langle \phi_{\lambda}\right| \left(\left(1-P_h\right) \left(\hat{T} + v^{1}_{eff}\right) \left|h_{i\alpha\sigma}\right\rangle \left\langle h_{i\alpha\sigma}\right| + c.c. \right) \left|\phi_{\lambda'}\right\rangle \tag{5.138}$$

and

$$\frac{dE^{1}}{d\bar{\rho}} = \sum_{\Lambda,\Lambda'} \left|\tilde{p}_{\Lambda}\right\rangle \tilde{D}^{1}_{\Lambda\Lambda'} \left\langle \tilde{p}_{\Lambda}\right| \tag{5.139}$$

$$\tilde{D}^1_{\Lambda\Lambda'} = \tilde{D}^{1,v}_{\Lambda\Lambda'} + \tilde{D}^{1,z}_{\Lambda\Lambda'} \tag{5.140}$$

with

$$\tilde{D}^{1,v}_{\Lambda\Lambda'} = \left\langle \tilde{\phi}_\Lambda | \hat{T} + \tilde{v}^1_{eff} | \tilde{\phi}_{\Lambda'} \right\rangle + \sum_L \overline{\int \tilde{v}^1_{eff}(\mathbf{r}) \hat{Q}^{s,L}_{\Lambda\Lambda'}(\mathbf{r})} \tag{5.141}$$

$$\tilde{D}^{1,z}_{\Lambda\Lambda'} = \sum_{i\alpha\sigma} \frac{\partial z_{i\alpha\sigma}}{\partial n^0_{i\alpha\sigma}} \langle \phi_\Lambda | h^\dagger_{i\alpha\sigma} h_{i\alpha\sigma} | \phi_{\Lambda'} \rangle \tilde{e}^1_{i\alpha\sigma} \tag{5.142}$$

$$\begin{aligned} \tilde{e}^1_{i\alpha\sigma} &= \sum_{(\lambda,\lambda'),L} \rho_{\lambda\lambda'} \left(\int \tilde{v}^1_{eff}(\mathbf{r}) g_l(|\mathbf{r}-\mathbf{R}|) Y_L\left(\widehat{\mathbf{r}-\mathbf{R}}\right) dr \right) \\ &\quad \times \int \left(\langle \phi_\lambda | h_{i\alpha\sigma} \rangle \langle h_{i\alpha\sigma} | \mathbf{r} \rangle \langle \mathbf{r} | (1-P_h) | \phi_{\lambda'} \rangle + c.c. \right) |\mathbf{r}-\mathbf{R}|^l Y^*_L\left(\widehat{\mathbf{r}-\mathbf{R}}\right) d\mathbf{r} \end{aligned} \tag{5.143}$$

From the Lagrange multiplier $\{\mu_{i0}, \mu_{i\alpha\sigma}\}$,

$$D^\mu_{\Lambda\Lambda'} = \sum_{i\alpha\sigma} \langle \phi_\Lambda | h^\dagger_{i\alpha\sigma} h_{i\alpha\sigma} | \phi_{\Lambda'} \rangle \mu_{i\alpha\sigma} \tag{5.144}$$

Thus the effecitve Hamiltonian is

$$H_{eff} = \hat{T} + \tilde{v}_{eff} + \sum_{\Lambda,\Lambda'} |\tilde{p}_\Lambda\rangle \left(\hat{D}_{\Lambda\Lambda'} + D^1_{\Lambda\Lambda'} - \tilde{D}^1_{\Lambda\Lambda'} + D^\mu_{\Lambda\Lambda'} \right) \langle \tilde{p}_\Lambda | \tag{5.145}$$

We also have

$$e_{i\alpha\sigma} = \hat{e}_{i\alpha\sigma} + e^1_{i\alpha\sigma} - \tilde{e}^1_{i\alpha\sigma} \tag{5.146}$$

The double counting ΔE to total energy is treated in the following way.

$$\begin{aligned} \Delta E &= E_p + \tilde{E} + E^1 - \tilde{E}^1 - \left\langle \Psi_0 \left| \hat{H}_{eff} \right| \Psi_0 \right\rangle \\ &\quad - \int \rho V_{scr} + \frac{1}{2} \iint \rho v \rho - \frac{1}{2} \iint \rho_l v \rho_l \\ &\quad + \int (\rho + \rho_c) \varepsilon_{xc}[\rho + \rho_c] - \int \rho_l \varepsilon_{xc}[\rho_l] + E_{ion-ion} \end{aligned} \tag{5.147}$$

It may be expressed in a variational form

$$\begin{aligned}
\Delta E &= E_p + \int \tilde{v}_{eff}^{out}\tilde{\rho}^{out} + \sum_{\Lambda,\Lambda'}\rho_{\Lambda,\Lambda'}^{out}\left(\hat{D}_{\Lambda\Lambda'}^{v,out} + D_{\Lambda\Lambda'}^{1,v,out} - \tilde{D}_{\Lambda\Lambda'}^{1,v,out}\right) \\
&\quad - \int \tilde{v}_{eff}^{in}\tilde{\rho}^{out} - \sum_{\Lambda,\Lambda'}\rho_{\Lambda,\Lambda'}^{out}\left(\hat{D}_{\Lambda\Lambda'}^{in} + D_{\Lambda\Lambda'}^{1,in} - \tilde{D}_{\Lambda\Lambda'}^{1,in} + D_{\Lambda\Lambda'}^{\mu,in}\right) \\
&\quad - E_H\left[\tilde{\rho}+\hat{\rho}\right] - \overline{E_H\left[\rho^1\right]} + \overline{E_H\left[\tilde{\rho}^1+\hat{\rho}\right]} + \overline{E_H\left[\rho_l\right]} \\
&\quad - \int \mu_{xc}\left[\tilde{\rho}+\hat{\rho}+\tilde{\rho}_c\right](\tilde{\rho}+\hat{\rho})\,d\mathbf{r} + \overline{\int \mu_{xc}\left[\tilde{\rho}^1+\hat{\rho}+\tilde{\rho}_c\right](\tilde{\rho}^1+\hat{\rho})\,d\mathbf{r}} \\
&\quad - \overline{\int \mu_{xc}\left[\rho^1+\rho_c\right]\rho^1 d\mathbf{r}} + \overline{\int \mu_{xc}^l\left[\rho_l\right]\rho_l d\mathbf{r}} \\
&\quad + E_{xc}\left[\tilde{\rho}+\hat{\rho}+\tilde{\rho}_c\right] - \overline{E_{xc}\left[\tilde{\rho}^1+\hat{\rho}+\tilde{\rho}_c\right]} + \overline{\int (\rho+\rho_c)\,\varepsilon_{xc}\,(\rho+\rho_c)} - \overline{E_{xc}\left[\rho_l\right]} \\
&\quad + E_{ion-ion}
\end{aligned} \tag{5.148}$$

The charge density here should be output part if not indicated.

5.3 Application and preliminary results

5.3.1 Non-degenerate Anderson lattice

To get some sense of the Gutzwiller approximation, we first applied it to the paramagnetic Anderson lattice without orbital degeneracy. We assume a flat density of states for the conduction electrons

$$\rho_0(\omega) = \begin{cases} \frac{1}{D} & \text{if } -D < \omega < D \\ 0 & \text{otherwise} \end{cases} \tag{5.149}$$

5.3.1.1 Symmetric case

We look at the symmetric case with

$$\varepsilon_f^0 = -\frac{U}{2} \tag{5.150}$$

$$n^{tot} = 2 \tag{5.151}$$

$$D = 10V \tag{5.152}$$

Fig. 5.1 shows the density of states with different onsite Coulomb repulsion U. We can see that the hybridization gap between the local orbital and the delocalized orbital decreases

with increasing the onsite repulsion U. It is reasonable since the hybridization strength V is renormalized to zV with Gutzwiller approximation. Fig. 5.2 shows the variation of the hybridization energy gap, E_g, and renormalization factor, z, as functions of onsite U. As onsite U becomes stronger, the renormalized hybridization strength(zV) becomes weaker. Therefore the energy gap becomes smaller. In the limit of no hybridization, the energy gap closes. Note that in the symmetric case with total 2 electrons, the local orbital (f) occupation is always 1, one may wonder how onsite U affect the renormalization factor z. To investigate this issue, we need to look at the occupation probability of the local doubly occupied state, where the onsite U matters. Fig. 5.3 shows that the local doubly occupied state probability decreases as the onsite U increases. We may see a competition picture between the hybridization effect and onsite Coulomb repulsion effect. While the hybridization tends to lower the total energy, it needs to pay an energy penalty ($\propto U$) for the local doubly occupied state. The ground state of the system is a trade-off between these two effects.

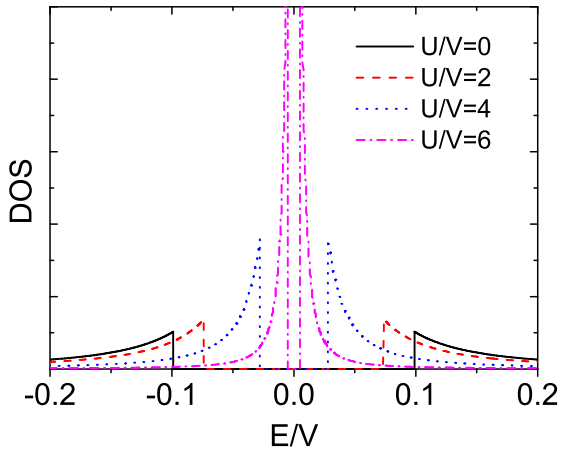

Figure 5.1 Density of states of the nondegenerate Anderson lattice in symmetric case with different onsite Coulomb repulsion U.

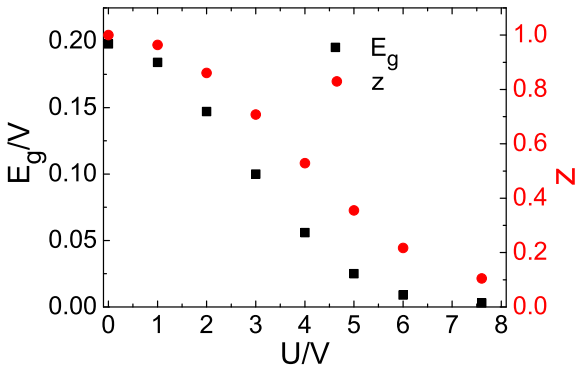

Figure 5.2 Variation of the hybridization energy gap, E_g, and renormalization, z, with increasing onsite U for symmetric nondegenerate Anderson lattice.

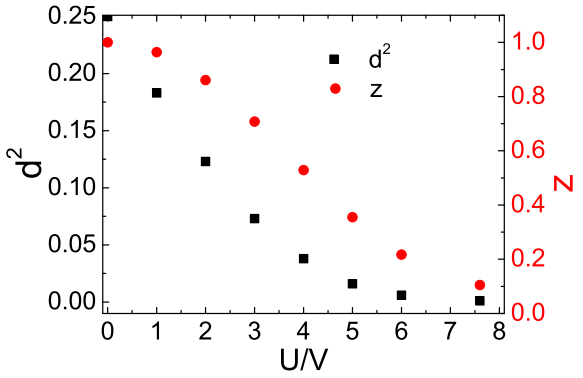

Figure 5.3 The local doubly occupied state occupation probability as a function of onsite U for symmetric nondegenerate Anderson lattice.

5.3.1.2 Non-symmetric case

It is also interesting to examine how the non-symmetric Anderson lattice will deviate from the symmetric case. As we can see in the symmetric case, there are three parameters (local orbital level ε_f^0, total number of electrons n^{tot}, and conduction electron band width D) which determine the symmetry properties of the model. We first want to see how the total number of electrons (n^{tot}) will affect the results. We choose $U = 6V$ for the analysis below. Fig. 5.4 shows the density of states with different filling electrons. The model exhibits a particle-hole symmetry with respect to total number of electrons about $n^{tot} = 2$. Fig. 5.5 shows that the energy gap E_g behavior is again consistent with the renormalization factor z. Fig. 5.6 shows the local configuration probabilities with a particle-hole symmetry.

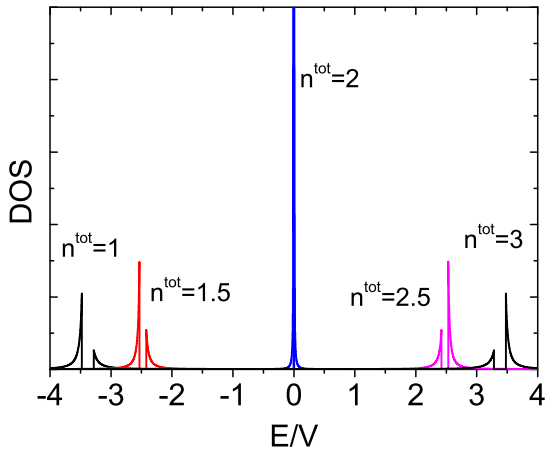

Figure 5.4 Density of states of the nondegenerate Anderson lattice at $\varepsilon_f^0 = -\frac{U}{2}$ with increasing total filling electrons.

We next investigated how the particle-hole symmetry would be affected by the local orbital level. We choose $\varepsilon_f^0 = -\frac{U}{2} - 7V$ for the analysis followed. Thus the center of the local orbital levels, $\varepsilon_f^c = \frac{2\varepsilon_f^0+U}{2}$, would be at $-7V$. Fig. 5.7 shows the consistency between the energy gap E_g and the renormalization factor z at different filling electrons, however, both curves lost the mirror symmetry. We also nitice that the local orbital is always half-filled

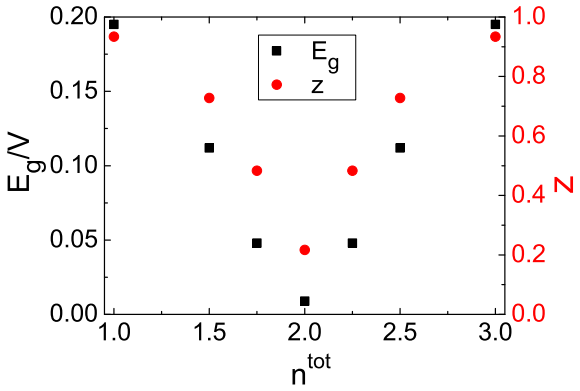

Figure 5.5 Variation of the hybridization energy gap, E_g, and renormalization factor, z, with increasing total filling electrons for nondegenerate Anderson lattice at $\varepsilon_f^0 = -\frac{U}{2}$.

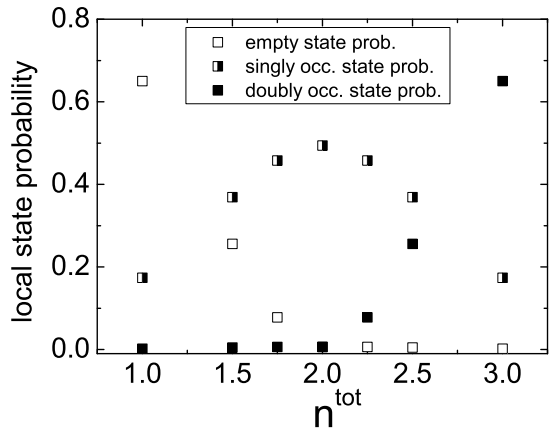

Figure 5.6 The local configuration probabilities with increasing total filling electrons for nondegenerate Anderson lattice at $\varepsilon_f^0 = -\frac{U}{2}$.

when the renormlization factor z reaches its minimum with the variation of filling electrons, as shown in fig. 5.8. It is physically reasonable since the system would have best degrees of freedom to redistribute the local electrons into local configurations. In the limit of empty or full occupation, the local configuration probability is fixed by the occupation with renormalization factor $z = 1$.

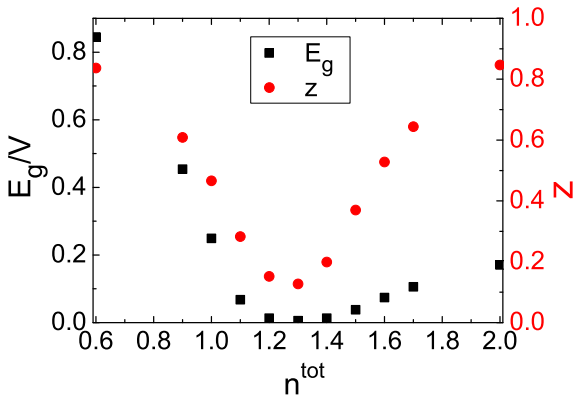

Figure 5.7 Variation of the hybridization energy gap, E_g, and renormalization, z, with increasing total filling electrons for nondegenerate Anderson lattice at $\varepsilon_f^0 = -\frac{U}{2} - 7V$.

5.3.2 FCC Ce

Ce is a rear earth element with 1 f-electron. Fig. 5.9 shows the phase digram for Ce, which is unexpectedly rich and puzzling. The most famous and yet unresolved problem of Ce is the isostructural $\gamma \rightarrow \alpha$ phase transformation with a volume change of 17% [Gschneider et al., (1978)].

While such big volume collapse was observed more than three decades ago, theoretical explanantions are still under debating. There are two promising models which might be able to address the volume collapse transition for Ce: Kondo volume collapse (KVC) model[Allen et al., (1982,1992); Lavagna et al., (1982)] and Mott transition (MT) model[Johansson et al., (1974,1995)]. The KVC model assumes that the $4f$ orbitals hold the local property in both α and γ phase. It is the conduction electron screening effect that drives $\alpha \rightarrow \gamma$

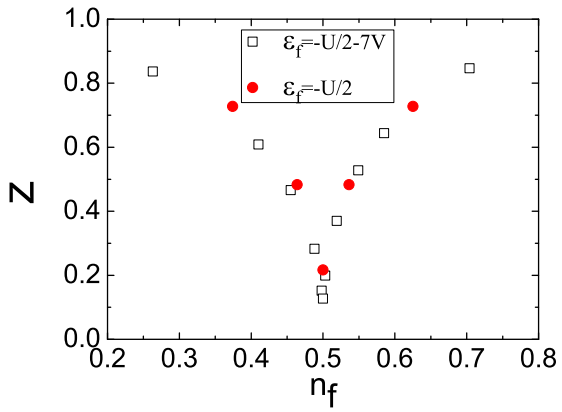

Figure 5.8 The behaviour of the renormalization factor, z, with increasing local orbital occupation, n_f, for nondegenerate Anderson lattice.

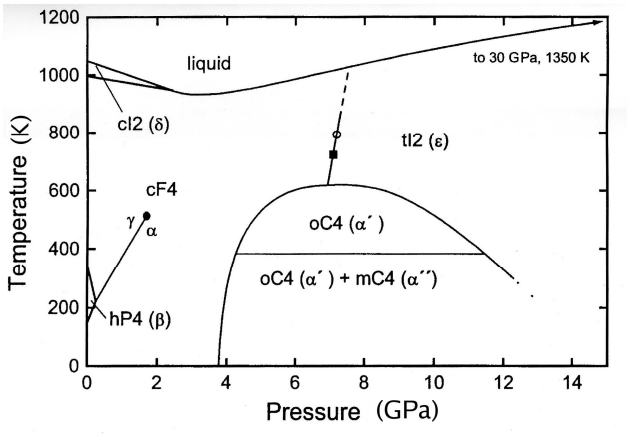

Figure 5.9 P-T phase diagram of pure Ce.

transition. However, in the MT model, the conduction electrons have no contribution at all. It is the $4f-4f$ hybridization effect that drives phase transition. Both models are based on model Hamiltonian approach. The important parameters are obtained by fitting procedure with the experimental data, where some uncertainties are involved. The recently developed LDA+DMFT have been applied to investigate this problem, yet controversial results are reported[Held at al., (2001); Amadon et al., (2006)]. Note that even in LDA+DMFT method, parameters like onsite repulsion U are not self-consistently determined. Thus Ce provides an ideal playground to test our new DFT method where all the interactions are treated self-consistently.

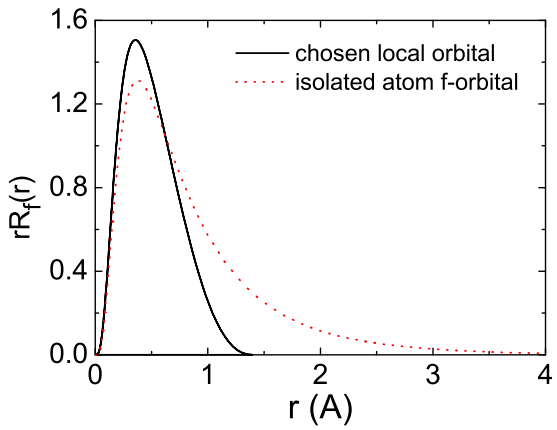

Figure 5.10 Radial function for the chosen local orbital and isolated atomic f-orbital.

We choose our local orbitals to be confined in the augmentation sphere as we discussed in the previous methodology part. Fig.5.10 shows the radial function of our local $f-$orbital. The radial function of the $f-$orbital for an isolated Ce atom is also shown for reference. We understand that the choice of local orbitals for Gutzwiller projector may be critical. Strictly speaking, the set of local orbitals must be expanded until convergence. However, it is still physically interesting to see how the choice of confined local orbitals affect the calculation results.

Fig. 5.11 shows the total energy (E) versus volume (V) curve of Ce with our Gutzwiller-

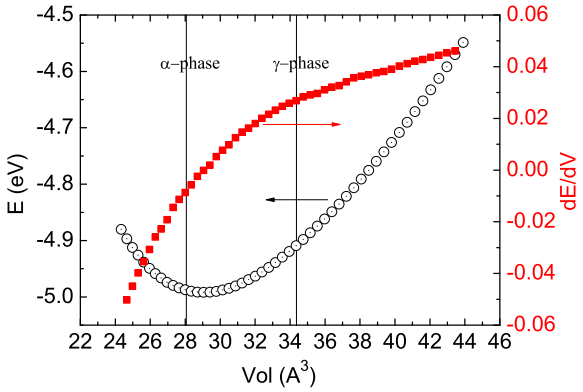

Figure 5.11 Total energy of FCC-Ce versus unit cell volume calculated with Gutzwiller-DFT method.

DFT method. The first derivative of E with respect to V is also plotted. Under the current choice of local orbitals and Gutzwiller projectors, we do not find double minimums in the curve. However, we find that the $E-V$ curve gives a minimum which is closer to the $\alpha-$phase than conventional LDA results. Table 5.1 listes the equilibrium lattice constant (a_0) and the bulk modulus (B) of FCC-Ce obtained from LDA-DFT, Gutzwiller-DFT and experiment. Gutzwiller-DFT gives much closer results to experiment.

Table 5.1 Equilibrium lattice constant and bulk modulus of $\alpha-$Ce obtained from LDA, Gutzwiller-LDA calculations and experiment.

	$a_0(\mathring{A})$	B (GPa)
LDA	4.52	57.4
G-LDA	4.88	34.7
Expt.	4.83	27.0

In the Gutzwiller-DFT calculations, local natural orbital occupation ($n^0_{i\gamma}$), local-nonlocal hopping ($e_{i\gamma}$) and the renormalization factor ($z_{i\gamma}$) are important quantities. Fig. 5.12 shows that local natural orbital occupation as a function of unit cell volume. In cubic symmetry, the seven-fold degenerate $f-$levels split to three different levels: two levels with degeneracy of three ($f_a\,(3)$, $f_b\,(3)$), and one nondegenerate level ($f_c\,(1)$). When the unit cell volume is small, i.e., the crystal field effect is strong, we have very different three sets of local natural

orbital occupations. When the unit cell expands, the crystal field becomes weaker, the local natural orbital occupations tend to merge. The variation of local-nonlocal hopping and the renormalization factor with the unit cell volume is shown in fig. 5.13 and fig.5.14. Generally they are consistent with each other. As the lattice expands, the hybridization effect becomes weaker, the renormalization factors become smaller, and the local-nonlocal hoppings decrease. However, one may spot that the behaviour of the local-nolocal hopping term in fig.5.13 seems somehow weird. The top curve is more or less flat, and all the curves seem to converge to a value which is smaller than $-0.3eV$. We believe it is the evidence that the current confined local orbital choice need to be improved.

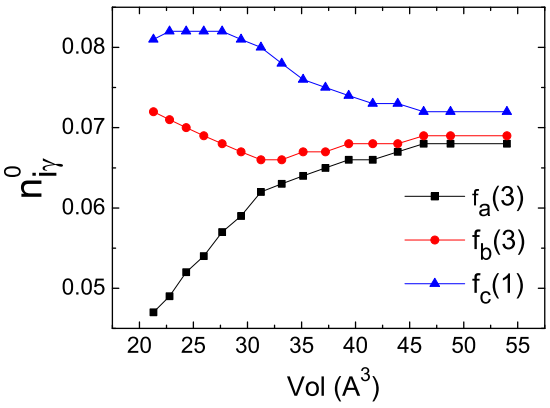

Figure 5.12 Variation of local natural orbital occupation with increasing unit cell volume.

5.4 Conclusion

We have developed an *ab initio* theoretical method which is targeted to solve the many-electron systems with electron correlation effect. We treat all the interactions in a self-consistent manner. Preliminary application to FCC Ce seems encouraging. Several aspects of the method need to be further studied, e.g., choice of Gutzwiller operator, choice of local orbitals, proper way to subtract the part which is treated exactly in the new DFT theory from LDA.

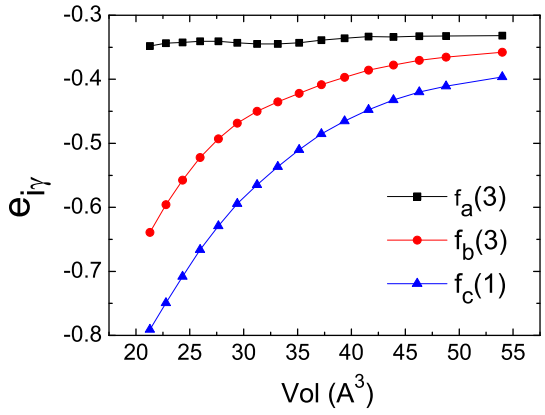

Figure 5.13 Variation of local-nonlocal hoppings with increasing unit cell volume.

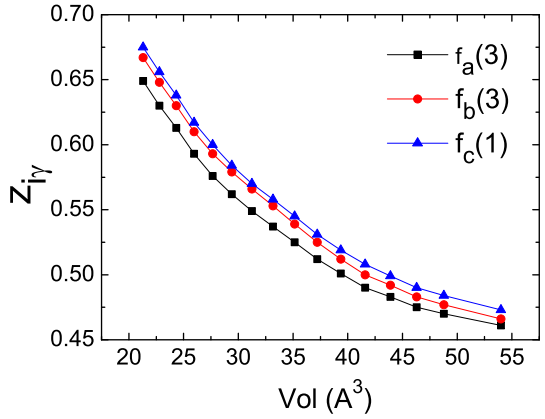

Figure 5.14 Variation of the renormalization factors with increasing unit cell volume.

APPENDIX A. CONSTRAINED MINIMIZATION FOR QUAMBO

We need to minimize

$$L = \sum_{\alpha i} \left(\langle \tilde{A}_\alpha - A_\alpha | \tilde{A}_\alpha - A_\alpha \rangle + \lambda_\alpha \left(\langle \tilde{A}_\alpha | \tilde{A}_\alpha \rangle - 1 \right) \right) \tag{A.1}$$

where

$$\left| \tilde{A}_\alpha \right\rangle = \sum_{\mathbf{k}\mu} C_\alpha^{\mathbf{k}\mu} \left| \phi_{\mathbf{k}\mu} \right\rangle \tag{A.2}$$

w.r.t. the set of coefficients $\{C\}$ and Lagrange multipliers $\{\lambda\}$.

We look at the terms in the Eq.A.1 one by one.

$$\langle \tilde{A}_\alpha | \tilde{A}_\alpha \rangle = \sum_{\mathbf{k}\mu} C_\alpha^{\mathbf{k}\mu} \left(C_\alpha^{\mathbf{k}\mu} \right)^* \tag{A.3}$$

$$\langle \tilde{A}_\alpha | A_\alpha \rangle = \sum_{\mathbf{k}\mu} \left(C_\alpha^{\mathbf{k}\mu} \right)^* \langle \phi_{\mathbf{k}\mu} | A_\alpha \rangle \tag{A.4}$$

$$\langle A_\alpha | A_\alpha \rangle = 1 \tag{A.5}$$

Taking derivatives of L,

$\frac{\partial L}{\partial \left(C_\alpha^{\mathbf{k}\mu} \right)^*}$ gives:

$$\left(1 + \lambda_\alpha\right) C_\alpha^{\mathbf{k}\mu} - \langle \phi_{\mathbf{k}\mu} | A_\alpha \rangle = 0 \tag{A.6}$$

$\frac{\partial L}{\partial \lambda_\alpha}$ gives:

$$\sum_{\mathbf{k}\mu} C_\alpha^{\mathbf{k}\mu} \left(C_\alpha^{\mathbf{k}\mu} \right)^* - 1 = 0 \tag{A.7}$$

Solving the two equations gives

$$C_\alpha^{\mathbf{k}\mu} = \frac{\langle \phi_{\mathbf{k}\mu} | A_\alpha \rangle}{1 + \lambda_\alpha} \tag{A.8}$$

$$\left(1 + \lambda_\alpha\right)^2 = \sum_{\mathbf{k}\mu} \left| \langle \phi_{\mathbf{k}\mu} | A_\alpha \rangle \right|^2 \tag{A.9}$$

i.e.,

$$\left|\tilde{A}_\alpha\right\rangle = D_\alpha^{-1/2} \sum_{\mathbf{k}\mu} |\phi_{\mathbf{k}\mu}\rangle \langle\phi_{\mathbf{k}\mu}|A_\alpha\rangle \tag{A.10}$$

with

$$\begin{aligned} D_\alpha^{-1/2} &= 1 + \lambda_\alpha \\ &= \sum_{\mathbf{k}\mu} |\langle\phi_{\mathbf{k}\mu}|A_\alpha\rangle|^2 \end{aligned} \tag{A.11}$$

APPENDIX B. METHODS FOR GENERATING OPTIMISED VIRTUAL BANDS

Generally we have the optimised virtual band expressed as a linear combination of the virtual bands

$$|\phi_{\mathbf{k}p}\rangle = \sum_{\mu=1}^{N_{VB}} T_p^{\mu\mathbf{k}} |\psi_{\mathbf{k}\mu}\rangle \tag{B.1}$$

we want to maximize

$$L = \sum_{\mathbf{k}} \sum_{p} \sum_{\alpha=1}^{N_q} \langle\phi_{\mathbf{k}p}|A_\alpha\rangle \langle A_\alpha|\phi_{\mathbf{k}p}\rangle + \sum_{\mathbf{k}p} \lambda_{\mathbf{k}p} \left(1 - \langle\phi_{\mathbf{k}p}|\phi_{\mathbf{k}p}\rangle\right)$$

The resulted optimised virtual bands are automatically orthogonal to the preserved bands since we are constructing them in a subspace spanned by all the rest virtual bands, which is orthogonal to the space spanned by the preserved bands. Here N_q is the total number of atomic orbitals. N_{VB} is the total number of virtual bands involved. Usually $N_q \ll N_{VB}$.

$\frac{\partial L}{\partial \langle\phi_{\mathbf{k}p}|}$ gives

$$\left(\sum_{\alpha=1}^{N_q} |A_\alpha\rangle \langle A_\alpha|\right) |\phi_{\mathbf{k}p}\rangle = \lambda_{\mathbf{k}p} |\phi_{\mathbf{k}p}\rangle \tag{B.2}$$

which turns out to be an eigen-value problem.

Mathematically, matrix $\sum_{\alpha=1}^{N_q} |A_\alpha\rangle \langle A_\alpha|$ only has N_q non-zero eigen-values. In the construction of QUAMBO, we may choose $N_q - n_{occ}(\mathbf{k})$ eigen-vectors with biggest eigen-values to get the T-matrix.

In practice, the number of virtual bands, N_{VB}, is determined by the dimension of the basis we used in the electronic structure calculation. It is usually very expensive to solve for all the eigen-vectors of the Hamiltonian matrix. Thus we may truncate the eigen-vectors according to the eigen-energy criteria, i.e., we may choose lowest N_{VB}^* bands at each k-point for the

construction of QUAMBOs. It works very well for simple elements and simple structures, e.g., Si in diamond structure. However, such implementation of the scheme becomes very expensive for complicated elements(like transition metals) and structures, where many more(hundreds or even thousands) bands need to be calculated for the construction of QUAMBO. It is very time-comsuming to calculate so many virtual bands in iterative way in standard DFT codes. Furthermore, it will also take a lot of disk space (several gigabyte or even tens of gigabyte) to store the wavefunctions.

The problem must be solved by a way without using virtual bands. It is true that the basis set(e.g., plane waves) of the DFT calculation already have all the information the virtual bands carry. Thus an improved algorithm of the QUAMBO scheme is that we may proceed directly from the DFT basis set. The solution may be formulated as follows.

Let the DFT basis set be $\{\varkappa_{\nu\mathbf{k}}\}$. The optimise virtual band may be expressed as

$$|\phi_{\mathbf{k}p}\rangle = \sum_{\nu=1}^{N_{BS}} T_p^{\nu\mathbf{k}} |\varkappa_{\nu\mathbf{k}}\rangle \tag{B.3}$$

where N_{BS} is the dimension of the basis set. We want to maximize

$$L = \sum_{\mathbf{k}} \sum_{p} \sum_{\alpha=1}^{N_q} \langle\phi_{\mathbf{k}p}|A_\alpha\rangle \langle A_\alpha|\phi_{\mathbf{k}p}\rangle + \sum_{\mathbf{k}p} \lambda_{\mathbf{k}p} (1 - \langle\phi_{\mathbf{k}p}|\phi_{\mathbf{k}p}\rangle) - \sum_{\mathbf{k}} \sum_{\mu=1}^{n_{occ}(\mathbf{k})} \lambda_{\mathbf{k}\mu} \langle\phi_{\mathbf{k}p}|\psi_{\mathbf{k}\mu}\rangle \tag{B.4}$$

the additional constraints come from the fact that the optimised virtual band $|\phi_{\mathbf{k}p}\rangle$ is not guaranteed to be orthogonal to the preserved bands since it is now constructed in the whole space spanned by the basis set in the DFT calculation.

$\frac{\partial L}{\partial \langle\phi_{\mathbf{k}p}|}$ gives

$$\left(\sum_{\alpha=1}^{N_q} |A_\alpha\rangle \langle A_\alpha| \right) |\phi_{\mathbf{k}p}\rangle - \sum_{\mu=1}^{n_{occ}(\mathbf{k})} \lambda_{\mathbf{k}\mu} |\psi_{\mathbf{k}\mu}\rangle = \lambda_{\mathbf{k}p} |\phi_{\mathbf{k}p}\rangle \tag{B.5}$$

By applying $\langle\psi_{\mathbf{k}\mu}|$ on Eq.B.5 we get

$$\lambda_{\mathbf{k}\mu} = \langle\psi_{\mathbf{k}\mu}| \left(\sum_{\alpha=1}^{N_q} |A_\alpha\rangle \langle A_\alpha| \right) |\phi_{\mathbf{k}p}\rangle$$

Substituting it bacl to Eq.B.5

$$\left(1 - \sum_{\mu=1}^{n_{occ}(\mathbf{k})} |\psi_{\mathbf{k}\mu}\rangle \langle\psi_{\mathbf{k}\mu}| \right) \left(\sum_{\alpha=1}^{N_q} |A_\alpha\rangle \langle A_\alpha| \right) |\phi_{\mathbf{k}p}\rangle = \lambda_{\mathbf{k}p} |\phi_{\mathbf{k}p}\rangle \tag{B.6}$$

This turns out to be an eigen-value problem for a non-hermitian square matrix. Note that we are solving the problem with a large dimension of basis set. The mature iterative solvers are usually for Hermitian matrix. We may simplify the above method by the following way. Mathematically, matrix $\left(1-\sum_{\mu=1}^{n_{occ}(\mathbf{k})}\left|\psi_{\mathbf{k}\mu}\right\rangle\left\langle\psi_{\mathbf{k}\mu}\right|\right)\left(\sum_{\alpha=1}^{N_q}\left|A_\alpha\right\rangle\left\langle A_\alpha\right|\right)$ also only has N_q non-zero eigen-values. And we need to choose $N_q - n_{occ}(\mathbf{k})$ eigen-vectors with biggest eigen-values to get optimised virtual bands. The original way to optimised the virtual band is to maximise the overlap between it and all the atomic orbitals. And we notice that space spanned by the atomic orbitals have "preserved bands-like" part and "virtual bands-like" part. The "preserved bands-like" part should have trivial overlap with the virtual bands. Thus we may choose only the "virtual bands-like" part to be our target to optimise the virtual. This approach in fact is much simpler in algebra and computation. Also it gives unique solution for QUAMBO.

The decomposition of the space spanned by the atomic orbitals into "preserved bands-like" part and "virtual bands-like" part may be proceeded in the following way. First we may construct a matrix $M^{\mathbf{k}}_{\alpha\beta}$

$$M^{k}_{\alpha\beta} = \sum_{\mu=1}^{n_{occ}(\mathbf{k})}\left\langle A_\alpha|\psi_{\mathbf{k}\mu}\right\rangle\left\langle\psi_{\mathbf{k}\mu}|A_\beta\right\rangle \tag{B.7}$$

Note that $n_{occ}(\mathbf{k}) \leq N_q$. The $N_q \times N_q$ matrix $M^{\mathbf{k}}$ only has $n_{occ}(\mathbf{k})$ non-zero eigen values. The $n_{occ}(\mathbf{k})$ eigen-vectors with non-zero eigen values, $|\lambda_{\mathbf{k}\mu}\rangle$, span the "preserved bands-like" subspace, while the rest $N_q - n_{occ}(\mathbf{k})$ eigen-vectors, $\left|\bar{\lambda}_{\mathbf{k}\mu}\right\rangle$, span the "virtual bands-like" subspace. Thus we have $\left\langle\psi_{\mathbf{k}\mu}|\bar{\lambda}_{\mathbf{k}\mu}\right\rangle = 0$ for $\mu = 1, \ldots, n_{occ}(\mathbf{k})$. Replace $\sum_{\alpha=1}^{N_q}\left|A_\alpha\right\rangle\left\langle A_\alpha\right|$ in Eq.B.6 with $\sum_{\mu=1}^{N_q-n_{occ}(\mathbf{k})}\left|\bar{\lambda}_{\mathbf{k}\mu}\right\rangle\left\langle\bar{\lambda}_{\mathbf{k}\mu}\right|$ and we get the simpler eigen-value problem

$$\left(\sum_{\mu=1}^{N_q-n_{occ}(\mathbf{k})}\left|\bar{\lambda}_{\mathbf{k}\mu}\right\rangle\left\langle\bar{\lambda}_{\mathbf{k}\mu}\right|\right)\left|\phi_{\mathbf{k}p}\right\rangle = \lambda_{\mathbf{k}p}\left|\phi_{\mathbf{k}p}\right\rangle \tag{B.8}$$

This method has been successfully applied to BCC Mo and graphene system.

The above algorithm solved the problem of demanding too many virtual bands in the QUAMBO construction by taking the optimised virtual bands directly from space spanned by the basis set of the DFT calculation. However, iteratively solving for $|\phi_{\mathbf{k}p}\rangle$ in a large basis set still takes some time. Qian et al., (2008) realize that atomic orbitals themselves already

contain all the relevant virtual bands information. The optimised virtual may be obtained in a much smaller subspace. The subspace is spanned by the atomic orbitals, subtracting the overlapping part with the preserved bands, i.e., $|A_\alpha\rangle - \sum_{\mu=1}^{n_{occ}(\mathbf{k})} |\psi_{\mathbf{k}\mu}\rangle \langle\psi_{\mathbf{k}\mu}|A_\alpha\rangle$. The dimension of the subspace is N_q. Thus the eigen-value problem is very trivial to be solved.

By comparing the above two methods, we may find that $\left|\bar{\lambda}_{\mathbf{k}\mu}\right\rangle$ in the first method actually also spans a subspace within which the optimised virtual bands may be obtained. We tried these two versions of "QO" and get successful results in both cases.

BIBLIOGRAPHY

Allen, J. W., and Martin, R. M. (1982). Kondo Volume Collapse and the $\gamma \rightarrow \alpha$ Transition in Cerium. *Phys. Rev. Lett.*, *49*, 1106–1110. Allen, J. W., and Liu, L. Z. (1992) $\gamma \rightarrow \alpha$ transition in Cerium. II. A detailed analysis of the Kondo volume-collapse model. *Phys. Rev. B*, *46*, 5047–5054.

Amadon, B., Biermann, S., Georges, A., and Aryasetiawan, F. (2006). The $\alpha - \gamma$ Transition of Cerium Is Entropy Driven. *Phys. Rev. Lett.*, *96*, 066402.

Andersen, O. K., and Jepsen, O. (1984). Explicit, First-Principles Tight-Binding Theory. *Phys. Rev. Lett.*, *53*, 2571–2574; Andersen, O. K., and Saha-Dasgupta, T. (2000). Muffin-tin orbitals of arbitrary order. *Phys. Rev. B*, *62*, R16219–R16222; Andersen, O. K., Saha-Dasgupta, T., Tank, R. W., Arcangeli, C., Jepsen, O., and Krier, G. (2000) Developing the MTO Formalism. emphLecture Notes in Physics, *535*, 3.

Anisimov, V. I., and Gunnarsson, O. (1991). Density-functional calculation of effective Coulomb interactions in metals. *Phys. Rev. B*, *43*, 7570–7574. Anisimov, V. I., Zaanen, J., and Anderson O. K. (1991) Band theory and Mott insulators: Hubbard U instead of Stoner I. *Phys. Rev. B*, *43*, 943–954. Anisimov, V. I., Solovyev, I. V., and Korotin, M. A. (1993) Density-functional theory and NiO photoemission spectra. *Phys. Rev. B*, *48*, 16929–16934.

Ashman, S C., Khanna, N., Liu, F., Jena, P., Kaplan, T., and Mostoller, M. (1997). $(BAl_{12})Cs$: mA cluster-assembled solid. *Phys. Rev. B*, *55*, 15868–15873.

Aziz, M. J., and Boettinger, W. J. (2004). On the transition from short-range diffusion-limited to collision-limited growth in alloy solidification. *Acta metallurgica et materialia*, *42*, 527–537.

Blöchl, P. E. (1994). Projector augmented-wave method. *Phys. Rev. B*, *50*, 17953–17979.

Boettinger, W. J. (1982). Growth kinetic limitation during rapid solidication. *MRS Symp. Proc.*, *8*, 15–31.

Bünemann, J., Weber, W., and Gebhard, F. (1998). Multiband Gutzwiller wave functions for general on-site interactions. *Phys. Rev. B*, *57*, 6896–6916. Bünemann, J., Gebhard, F. (2007). Equivalence of Gutzwiller and slave-boson mean-field theories for multiband Hubbard models. *Phys. Rev. B*, *76*, 193104.

Cacciamani, G., and Ferro, R. (2001). Thermodynamic modeling of some aluminium-rare earth binary systems: Al-La, Al-Ce and Al-Nd. *CALPHAD*, *25*, 583–597.

Cacciamani, G., Negri, S. De., Saccone, A., and Ferro R. (2003). The Al-R-Mg (R=Gd, Dy, Ho) systems. Part II: Thermodynamic modelling of the binary and ternary systems. *Intermetallics*, *11*, 1135–1151.

Chattopadyay, K., Ramachandrarao, R., Lele, S., and Anantharaman, T. R. (1976). in Proceedings of the Second International Conference on Rapidly Quenched Metals, edited by N. J. Grant and B. C. Giessen (MIT, Massachusetts, 1976) Sec. I, p. 157.

Chelikowsky, J. R., and Louie, S. G. (1996). Quantum Theory of RealMaterials. *Kluwer Press, 1996.*

Cohen, M. H., and Turnbull, D. (1959). Molecular Transport in Liquids and Glasses. *The Journal of Chemical Physics*, *31*, 1164–1169.

Davies, H. A., and Hull, J. B. (1972). An amorphous phase in a splat-quenched A1-17.3 at %Cu alloy. *Scripta Metallurgica*, *6*, 241–245.

Davies, H. A., and Lewis, B. G. (1975). A generalised kinetic approach to metallic glass formation. *Scripta Metallurgica*, *9*, 1107–1112.

Dinsdale, A.T. (1991). SGTE data for pure elements. *CALPHAD*, *15*, 317–425.

Donald, I. W., and Davies, H. (1978). Prediction of Glass-Forming Ability for Metallic Systems. *Journal of Non-Crystalline Solids*, *30*, 77–85.

Dorin, V., and Schlottmann, P. (1992). Magnetic instabilities in Kondo insulators. *Phys. Rev. B*, *46*, 10800–10807.

Duplock, E. J., Scheffer, M., and Lindan, P. J. D. (2004). Hallmark of Perfect Graphene. *Phys. Rev. Lett.*, *92*, 225502.

Duwez, P., Willens, R. H., and Crewdson, R. C. (1965). Amporphos phase in palladium-silicon alloys. *Journal of Applied Physics*, *36*, 2267–2269.

Egami, T. (2002). Nano-glass Mechanism of Bulk Metallic Glass Formation. *Materials Transactions, JIM*, *43*, 510–517.

Fecht, H. J., and Johnson, W. L. (2004). Thermodynamic properties and metastability of bulk metallic glasses. *Materials Science and Engineering A*, *375-377*, 2–8.

Galli, G., and Parrinello, M. (1992). Large scale electronic structure calculations. *Phys. Rev. Lett.*, *69*, 3547–3550.

Garzón, I. L., Rovira, C., Michaelian, K., Beltrán, M. R., Ordejón, P., Junquera, J., Sánchez-Portal, D., Artacho, E., and Soler J. M. (2000). Do Thiols Merely Passivate Gold Nanoclusters? *Phys. Rev. Lett.*, *85*, 5250–5251.

Giessen, B. C., and Whang, S. H. (1980). Formation and Characterization of Amorphous Metals. *J. Phys. (Paris) Colloq.*, *41*, C8–95.

Goedecker, S. (1999). Linear scaling electronic structure methods. *Rev. Mod. Phys.*, *71*, 1085–1123.

Gotze W., and Sjogren, L. (1992). Relaxation processes in supercooled liquids. *Reports on Progress in Physics*, *55*, 241–376.

Greer, A. L. (1995). Metallic glasses. *Science*, *267*, 1947.

Gröbner J., Lukas, H.-L., and Aldinger, F. (1995). Thermodynamic calculations in the Y-Al-C system. *Journal of Alloys and Compounds*, *220*, 8–14.

Gschneider, K. A. Jr., and Eyring, L. R. (North-Holland, Amsterdam, 1978).

Gutzwiller M. (1963). Effect of Correlation on the Ferromagnetism of Transition Metals. *Phys. Rev. Lett.*, *10*, 159. Gutzwiller M. (1965). Correlation of Electrons in a Narrow s Band. *Phys. Rev. B*, *137*, A1726.

Han, M. Y., Ozyilmaz, B., Zhang, Y., and Kim, P. (2007). Energy Band-Gap Engineering of Graphene Nanoribbons. *Phys. Rev. Lett.*, *98*, 206805.

Held, K., McMahan, A. K., and Scalettar, R. T. (2001). Cerium Volume Collapse: Results from the Merger of Dynamical Mean-Field Theory and Local Density Approximation. *Phys. Rev. Lett.*, *87*, 276404.

Hernandez, E., and Gillan, M. J. (1995). Self-consistent first-principles technique with linear scaling. *Phys. Rev. B*, *51*, 10157–10160.

Ho, K. M., Elsässer, C., Chan, C. T., and M. Fähnle (1992). First-principles pseudopotential calculations for hydrogen in 4d transition metals. I. Mixed-basis method for total energies and forces. *J. Phys: Condensed Matter*, *4*, 5189–5206.

Ihm, J., Zunger, A., and Cohen, M. L. (1979). Momentum-space formalism for the total energy of solids. *Journal of Physics C-Solid State Physics*, *12*, 4409–4422.

Inoue, A. (1998). Amorphous, nanoquasicrystalline, and nanocrystalline alloys in Al-based systems. *Progress in Materials Science*, *43*, 365–520.

Inoue, A., Zhang, T., and Masumoto, T. (1993). Glass forming ablity of alloys. *Journal of Non-Crystalline Solids*, *156-158*, 473-480.

Inoue, A., Zhang, W., Zhang, T., and Kurosaka, K. (2001). High strength Cu-based bulk glassy alloys in Cu-Zr-Ti and Cu-Hf-Ti ternary systems. *Acta Materialia*, *49*, 2645–2652.

Inoue, A., and Takeuchi, A (2002). Recent Progress in Bulk Glassy Alloys. *Materials Transactions*, *43*, 1892–1906.

Jacle, J. (1986). Models of the glass transition. *Reports on Progress in Physics*, *49*, 171–231.

Johansson, B. (1974). The $\alpha - \gamma$ transition in cerium is a Mott transition. *Philos. Mag.*, *30*, 469–482. Johansson, B., Abrikosov, I. A., Aldén, M., Ruban, A. V., and Skriver, H. L. (1995) Calculated Phase Diagram for the $\gamma \rightleftharpoons \alpha$ Transition in Ce. *Phys. Rev. Lett.*, *74*, 2335–2338.

Kauzmann, W. (1948). The nature of the glassy state and the behavior of liquids at low temperatures. *Chemical Review*, *43*, 219–256.

Kim, J., Mauri, F., and Galli, G. (1995). Total-energy global optimizations using nonorthogonal localized orbitals. *Phys. Rev. B*, *52*, 1640–1648.

Klement, W., Willen, R. H., and Duwez, P. (1960). Non-crystalline structure in solidified gold-silicon alloys. *Nature*, *187*, 869–890.

Koepernik, K., and Eschrig, H. (1999). Full-potential nonorthogonal local-orbital minimum-basis band-structure scheme. *Phys. Rev. B*, *59*, 1743–1757.

Hohenberg. P., and Kohn, W. (1964). Inhomogeneous Electron Gas. *Phys.Rev.*, *136*, B864–B871; Kohn, W., and Sham, L. J. (1965) Self-Consistent Equations Including Exchange and Correlation Effects. *Phys.Rev.*, *140*, A1133–A1138.

Kotliar, G., and Vollhardt, D. (2004). Strongly Correlated Materials: Insights From Dynamical Mean-Field Theory. *Physics Today*, *March 2004*, 53.

Kotliar, G., Savrasov, S. Y., Haule, K., Oudovenko, V. S., Parcollet, O., and Marianetti, C. A. (2006). *Rev. Mod. Phys.*, *78*, 865–951.

Kresse, G., and Hafner, J. (1993). *Ab initio* molecular dynamics for liquid metals. *Phys. Rev. B*, *47*, 558–561. Kresse, G., and Furthmuller, J. (1996). Efficient iterative schemes for *ab initio* total-energy calculations using a plane-wave basis set. *Phys. Rev. B*, *54*, 11169–11181.

Kresse, G., and Joubert, J. (1999). From ultrasoft pseudopotentials to the projector augmented-wave method. *Phys. Rev. B*, *59*, 1758–1775.

Kudin, N. M., Scuseria, G. E., and Martin R. L. (2003). *Phys. Rev. Lett.*, *89*, 266402.

Lang, N. D., and Kohn, W. (1970). Theory of Metal Surfaces: Charge Density and Surface Energy. *Phys. Rev. B*, *1*, 4555–4568.

Lavagna, M., Lacroix, C., and Cyrot, M. (1982). Volume collapse in the Kondo lattice. *Phys. Lett. A*, *90*, 210–212.

Louie, S. G., Ho, K.-M., and Cohen M. L. (1979). Self-consistent mixed-basis approach to the electronic structure of solids. *Phys. Rev. B*, *19*, 1774–1782.

Lu, Z. P., Li, Y., and Ng, S. C. (2000). Reduced glass transition temperature and glass forming ability of bulk glass forming alloys. *Journal of Noncrystalline Solids*, *270*, 103–114.

Lu, Z. P., and Liu, C. T. (2002). A new glass-forming ability criterion for bulk metallic glasses. *Acta Materialia*, *50*, 3501–3512.

Lu, Z. P., and Liu, C. T. (2003). Glass Formation Criterion for Various Glass-Forming Systems. *Physical Review Letters*, *91*, 115505.

Lu, W. C., Wang, C. Z., Schmidt, M. W., Bytautas, L., Ho, K. M., and Ruedenberg, K. (2004). Molecule intrinsic minimal basis sets. I. Exact resolution of ab initio optimized molecular orbitals in terms of deformed atomic minimal-basis orbitals. *J. Chem. Phys.*, *120*, 2629; Molecule intrinsic minimal basis sets. II. Bonding analyses for Si_4H_6 and Si_2 to Si_{10}. *J. Chem. Phys.*, *120*, 2638.

Lu, W. C., Wang, C. Z., Chan, T. L., Ruedenberg, K., and Ho, K. M. (2004). Representation of electronic structures in crystals in terms of highly localized quasiatomic minimal basis orbitals. *Phys. Rev. B*, *70*, 041101; Lu, W. C., Wang, C. Z., Ruedenberg, K., and Ho, K. M. (2004). Transferability of the Slater-Koster tight-binding scheme from an environment-dependent minimal-basis perspective. *Phys. Rev. B*, *72*, 205123; Chan, T. L., Yao, Y. X., Wang, C. Z., Lu, W. C., Li, J., Qian, X. F., Yip, S., and Ho, K. M. (2007) *Phys. Rev. B*, *76*, 205119.

Mao Yuliang, Yuan Jianmei, and Zhong Jianxin (2008). Density functional calculation of transition metal adatom adsorption on graphene. *J. Phys.: Condens. Matter*, *20*, 115209.

Marcus, M., and Turnbull, D. (1976). On the Correlation between Glass-Forming Tendency and Liquidus Temperature in Metallic Alloys. *Materials Science and Engineering*, *23*, 211–214.

Martins, T. B., Miwa, R. H., da Silva, A. J. R., and Fazzio, A. (2007). Electronic and Transport Properties of Boron-Doped Graphene Nanoribbons. *Phys. Rev. Lett.*, *98*, 196803.

Marzari, N., and Vanderbilt, D. (1997). Maximally localized generalized Wannier functions for composite energy bands. *Phys. Rev. B*, *56*, 12847–12865.

Mauri, F., Galli, G., and Car, R. (1993). Orbital formulation for electronic-structure calculations with linear system-size scaling. *Phys. Rev. B*, *47*, 9973–9976.

McMahan K. (2005). *Phys. Rev. B*, *72*, 115125.

Moruzzi, V. L., Janak, J. F., and Williams, A. R. (1978). Calculated Electronic Properties of Metals(Pergamon, New York, 1978).

Murty, B. S., and Hono, K. (2000). Formation of nanocrystalline particles in glassy matrix in melt-spun Mg-Cu-Y based alloys. *Materials Transactions, JIM*, *41*, 1538–1544.

Nakada, K., Fujita, M., Dresselhaus, G., and Dresselhaus, M. S. (1996). Edge state in graphene ribbons: Nanometer size effect and edge shape dependence. *Phys. Rev. B*, *54*, 17954–17961.

Nash, P., and Schwartz, R. B. (1988). Calculation of the glass forming range in binary metallic systems using thermodynamic models. *Acta Metallurgica*, *36*, 3047–3053.

Ordejon, P., Drabold, D. A., Grumbach, M. P., and Martin, R. M. (1993). Unconstrained minimization approach for electronic computations that scales linearly with system size. *Phys. Rev. B*, *48*, 14646–14649.

Payne, M. C., Teter, M. P., Allan, D. C., Arias, T. A., and Joannopoulos, J. D. (1992). Iterative minimization techniques for ab initio total-energy calculations: molecular dynamics and conjugate gradients. *Rev. Mod. Phys.*, *64*, 1045–1097.

Perdew, J. P., Tran, H. Q., and Smith, E. D. (1990). Stabilized jellium: Structureless pseudopotential model for the cohesive and surface properties of metals. *Phys. Rev. B*, *42*, 11627–11636.

Perdew J. P., Burke K., and Ernzerhof M. (1996). Generalized Gradient Approximation Made Simple. *Phys. Rev. Lett.*, *77*, 3865–3868.

Perdew, J. P. (2003). A Primer in Density Functional Theory, Edited by C. Fiolhais, F. Nogueira, M. Marques. *Lecture Notes in Physics*, *620*, 1–55.

Petit, L., Svane, A., Szotek, Z., and Temmerman W. M. (2002). *Science*, *301*, 498. *Eur. Phys. J. B*, *25*, 139–146.

Pickett, W. E. (1989). Pseudopotential methods in condensed matter applications. *Computer Physics Reports*, *9*, 115–197.

Predecki, P., Giessen B. C., and Grant, N. J. (1965). New Metastable Alloy Phases of Gold Silver AND Aluminum. *Trans. Metall. Soc. AIME*, *233*, 1438.

Prodan, I. D., Scuseria, G. E., and Martin R. L. (2005). *Chem. Phys.*, *3*, 225.

Puska, M. J., Nieminen, R. M., and Manninen M. (1981). *Phys. Rev. B*, *24*, 3037–3047.

Puska, M. J., and Nieminen, R. M. (1991). Atoms embedded in an electron gas: Beyond the local-density approximation. *Phys. Rev. B*, *43*, 12221–12233.

Qian, X. F., Li, J., Qi, L., Wang, C. Z., Chan ,T. L., Yao, Y. X., Ho, K. M., and Yip, S. (2008). Quasiatomic orbitals for ab initio tight-binding analysis. *Phys. Rev. B*, *78*, 245112.

Ramachandrarao, P., Laridjani, M., and Cahn, R. W. (1972). *Z. Metallkd*, *63*, 43.

Rose, J. H., and Shore, H. B. (1991). Bonding energetics of metals: Explanation of trends. *Phys. Rev. B*, *43*, 11605–11611.

Sastry, G. V. S., Suryanarayana, C., Srivastava, O. N., and Davies, H. A. (1978). *Trans. Indian Inst. Metals*, *31*, 292.

Saunders, N., and Miodownik, A. P. (1986). Thermodynamic aspects of amorphous phase formation. *Journal of Materials Research*, *1*, 38–46.

Savrasov, S. Y., Kotliar, G., and Abrahams E. (2001). *Nature*, *410*, 793.

Shen, T. S., He, Y., and Schwartz, R. B. (1998). Bulk amorphous Pd-Ni-Fe-P alloys: preparation and characterization. *Jounral of Materials Research*, *14*, 2107–2115.

Shen, T. D., and Schwartz, R. B. (1999). Bulk ferromagnetic glasses prepared by flux melting and water quenching. *Applied Physics Letters*, *75*, 49–51.

Sheng, W., Luo,W. K., Alamgir, F. M., Bai, J. M., and Ma E. (2006). Atomic packing and short-to-medium-range order in metallic glasses. *Nature*, *439*, 419–425.

Shore, H. B., and Rose, J. H. (1991). Theory of ideal metals. *Phys. Rev. Lett.*, *66*, 2519–2522.

Soler, J. M., Artacho, E., Gale, J., Garcia, A., Junquera, J., Ordejon, P., and Sanchez-Portal, D. (2002). The SIESTA method for ab initio order-N materials simulation. *J. Phys.: Condens. Matter*, *14*, 2745–2779.

Son, Y. W., Cohen, M. L., and Louie, S. G. (2006). Energy Gaps in Graphene Nanoribbons. *Phys. Rev. Lett.*, *97*, 216803.

Takeuchi, A., and Inoue, A. (2001). Quantitative evaluation of critical cooling rate for metallic glasses. *Materials Science and Engineering A*, *A304-306*, 446–451.

Tang, Mingsheng, Wang, C. Z., Lu W. C., and Ho K. M. (2006). Structures of $Si_7H_{2m}(m = 1 - 7)$ clusters by global optimization. *Phys. Rev. B*, *74*, 195413.

Taub, A. I., and Spaepen, F. (1980). The kinetics of structural relaxation of a metallic glass. *Acta Metallurgica*, *28*, 1781–1788.

Troullier, N., and Martins, J. L. (1991). Efficient pseudopotentials for plane-wave calculations. *Phys. Rev. B*, *43*, 1993–2006.

Turnbull, D. (1969). Under what conditions can a glass be formed. *Contemp. Phys.*, *10*, 473–488.

Turnbull, D. (1970). On the Free-Volume Model of the Liquid-Glass Transition. *The Journal of Chemical Physics*, *52*, 3038–3041.

Turnbull, D., and Cohen, M. H. (1961). Free-Volume Model of the Amorphous Phase: Glass Transition. *The Journal of Chemical Physics*, *34*, 120–125.

Uhlmann, D. R. (1972). A kinetic treatment of glass formation. *Journal of Non-Crystalline Solids*, *7*, 337–348.

Utreras-Diaz, C. A., and Shore, H. B. (1984). Pseudojellium Model for Surface Properties of Simple Metals. *Phys. Rev. Lett.*, *53*, 2335–2338.

Vanderbilt, D. (1990). Soft self-consistent pseudopotentials in a generalized eigenvalue formalism. *Phys. Rev. B*, *41*, 7892–7895.

Wang Wei Hua (2007). Roles of minor additions in formation and properties of bulk metallic glasses. *Progress in Materials Science*, *52*, 540–596.

Whang, S. H. (1983). New Predictions of Glass-forming Ability in Binary Alloys Using a Temperature-Composition Map. *Materials Science and Engineering*, *57*, 87–95.

Yang, W. (1991). Direct calculation of electron density in density-functional theory. *Phys. Rev. Lett.*, *66*, 1438–1441.

Zhu, A., Poon, S. J., and Shiflet, G. J. (2004). On glass formability of Al-Gd-Ni (Fe). *Scripta Materialia*, *50*, 1451–1455; Zhu, A., Shiflet, G. J., and Miracle, D. B. (2004). Glass forming ranges of Al-rare earth metal alloys: thermodynamic and kinetic analysis. *Scripta Materialia*, *50*, 987–991.